DISSERTATION

Energy and Battery Management for Non-Road Hybrid Electric Vehicles

ausgeführt zum Zwecke der Erlangung des akademischen Grades
eines Doktors der technischen Wissenschaften
unter der Leitung von

Univ.-Prof. Dipl.-Ing. Dr.techn. Stefan Jakubek

am Institut für Mechanik und Mechatronik
Arbeitsgruppe für Regelungstechnik und Prozessautomatisierung

eingereicht an der Technischen Universität Wien,
Fakultät für Maschinenbau

von

Dipl.-Ing. Johannes Unger
Sonnwendgasse 34/32
1100 Wien

Geboren am 13.05.1987
Matr.Nr.: 0526365

Wien, am 27. Mai 2015

Meiner Familie

Kurzfassung

Die Regelung eines elektrischen Hybridantriebs in elektrischen Hybridfahrzeugen (HEV) wird durch das Energiemanagementsystem (EMS) umgesetzt und zielt darauf ab, den Kraftstoffverbrauch und die Abgasemissionen zu minimieren. Legislative Regulierungen verlangen die Einhaltung von Abgasemissionen, wodurch das EMS gezwungen wird, bestimmte Strategien zu verfolgen und die Beschränkungen des Antriebsstrangs zu berücksichtigen. In diesem Zusammenhang sind non-road Fahrzeuge, wie beispielsweise Radlader oder Bagger, besonders schwierig zu steuern, da ihr Lastbedarf sehr dynamisch und vorab nicht bekannt ist.

Auf der Grundlage der verfügbaren Freiheitsgrade des Systems, präsentiert diese Arbeit ein EMS, das die Abgasemissionen sowie den Kraftstoffverbrauch deutlich reduzieren kann. Das EMS ist mit einem kaskadierten Regelungskonzept umgesetzt, welches die langsame Dynamik der Batterie sowie die schnelle Dynamik der Drehzahl und Drehmomente adressiert. Eine optimale Regelung wird durch die nichtlineare Optimierung des Gesamtsystems erreicht, welches die Nichtlinearitäten des elektrischen Systems, eine Prädiktion der zukünftigen kurzfristigen Last und wiederkehrend auftretende zyklische Lasten der Anwendungen berücksichtigt. Zu diesem Zweck sind Korrelationsanalyse und Bayessche Inferenz adaptiert.

Das EMS benötigt darüber hinaus den akkuraten Ladezustand (SoC) der Batterie, der on-line nicht messbar ist und präzise geschätzt werden muss, um die physikalische Leistungsfähigkeit des Antriebsstrangs voll ausschöpfen zu können. Aus diesem Grund wird in dieser Arbeit ein hoch dynamisches Batteriemodell präsentiert, dass auf dem datenbasierten Ansatz des lokalen Modellnetzwerks aufbaut. Die Modellgenauigkeit ist aufgrund des datenbasierten Ansatz maßgebend abhängig von den Trainingsdaten, weshalb optimale modellbasierte Versuchsplanung angewandt wird, um die Genauigkeit der Batteriemodelle zu erhöhen. Basierend auf den erhaltenen Batterie-Zellmodellen, werden dann ein Batterie-Modulmodell und ein SoC-Schätzer für den Einsatz in non-road Fahrzeugen entworfen.

Um die Umsetzbarkeit des Konzepts in Echtzeit zu zeigen, wird das allgemein anwendbare EMS auf einem realen Prüfstand implementiert. Ein Radlader ist als repräsentatives Beispiel für mobile Arbeitsmaschinen gewählt. Reale Lastzyklen werden verwendet, um die Möglichkeit der Prädiktion des zukünftig benötigten Lastbedarf ausschließlich anhand des aktuellen Fahrzeugzustands sowie vergangenen Lastsignals zu demonstrieren. Am Prüfstand, zeigten die Ergebnisse, dass der Kraftstoffverbrauch sowie die Abgasemissionen signifikant reduziert werden konnten, obwohl die Strategien Phlegmatisierung (Beschränkung des Motordrehmomentgradienten) und Downspeeding (reduzierte Drehzahl) die Motordynamik limitierten und ausgeglichen werden mussten. Separat erhaltene Messungen von Batteriezellen und einem Batteriemodul konnten die hohe Genauigkeit der vorgestellten Batteriemodelle und des SoC-Schätzansatzes zeigen. Gleichzeitig wird aufgrund der Messungen von Lithiumeisenphosphat und Lithiumpolymer Batteriezellen, die Zellchemie-Unabhängigkeit des Ansatzes demonstriert.

Abstract

The control of hybrid electric powertrains in hybrid electric vehicles (HEV) is established by the energy management system (EMS) and aims to minimize fuel consumption and exhaust emissions. Legislative regulations require compliance with the limitations of exhaust emissions, which forces the EMS to follow given strategies and to keep constraints of the powertrain. In this context, non-road vehicles, such as wheel loaders or excavators, are especially difficult to control since their load demand is highly dynamic and unknown in advance.

Based on the available degrees of freedom of the system, this work presents an EMS that is able to significantly reduce the exhaust emissions and fuel consumption. The EMS is established by an cascaded control concept that addresses the slow dynamics of the battery as well as the fast dynamics of the rotational speed and torques, respectively. An optimal control is achieved by the nonlinear optimization of the overall system, which considers the nonlinearities of the electrical system, a prediction of the future short term load and recurrent cyclic loads of the applications. To this end, correlation analysis and Bayesian inference are adapted.

The EMS furthermore requires the accurate state of charge (SoC) of the battery, which is not measurable on-line and needs to be precisely estimated in order to fully exploit the physical capabilities of the powertrain. For this reason, a high dynamic battery model is presented in this work that is built on the data based local model network approach. The model accuracy is due to the data based approach decisively dependent on the training data for which reason optimal model based design of experiments is applied to increase the battery model accuracy. Based on the obtained battery cell models, a battery module model and a SoC estimator are designed to be used in non-road vehicles.

In order to demonstrate the feasibility of the concept in real time, the generically applicable EMS is implemented on a real testbed. A wheel loader is chosen as representative example for non-road machinery. Real load cycles are used to demonstrate the possibility of predicting the future load demand exclusively by the actual vehicle states as well as past load signal. At the testbed, the results showed that fuel consumption and exhaust emissions could be reduced significantly, although phlegmatisation (constrained engine torque gradient) and downspeeding (reduced rotational speed) strategies limited the engine dynamics and had to be compensated. Separately obtained measurements of battery cells and an battery module could show the high accuracy of the presented battery models and SoC estimation approach. Simultaneously, due to the measurements of lithium-iron-phosphate and lithium-polymer battery cells, respectively, the cell chemistry independence of the approach is demonstrated.

Acknowledgment

Contents

Chapter 1

Introduction

1.1 Motivation

Non-road mobile machinery (NRMM), such as wheel loaders or excavators, are highly dynamic, mostly cyclically used, applications (see Figure 1.1) that are operated by especially trained drivers to bring out the maximum performance of the vehicles, c.f. [36]. Usually, compared to on-road vehicles, higher power densities and load dynamics occur, which increase the exhaust emissions of non-road vehicles significantly [92]. In the past years, the legislative regulations for exhaust emissions of such vehicles also became more stringent (e.g. *US EPA Tier 4* respectively *EU Stage IV*, [146]) and will be more severe in the future (up to particle counting in e.g. *EU Stage V*, [147]). Exhaust after treatment systems (EATS) are in general used to keep the exhaust emission regulations, but they are cost intensive and may not be enough for future regulations [163]. Lowering the rotational speed of the powertrain (downspeeding) and limiting the dynamics of the engine torque (phlegmatisation) can decrease the fuel consumption and production of emissions in the engine, but these are contrary objectives compared to the required powertrain dynamics [152]. Considering the future load demand as well as cycle information in the control of the powertrain might also have positive effects on exhaust emission reduction, whereby the load demand of non-road machinery is mostly unknown and directly dependent on the driver. Nevertheless, a reduction of the generated exhaust emissions not exclusively achieved by EATS is desirable.

(a) Wheel loader at operation in stone quarry   (b) Excavator at operation in earth moving

Figure 1.1: Typical examples for non-road mobile machinery.

1.2 Characteristic applications of non-road mobile machines

Applications, where non-road mobile machines are established, are manifold. They are used in earth moving, material loading, refilling of bulk storages, ditching, building demolition, flattening and many other applications, which demand different requirements on their powertrain. The requirements are basically defined by the dynamics of the powertrain loads and need to be provided by the powertrain without engine stalling at high dynamic load peaks. In terms of energy, the drivetrain of non-road vehicles is mostly the main energy consumer, which sometimes enables recuperation of regenerative power. The wheel loader is such application that has high drivetrain energy consumption as well as high dynamic load requirements due to the rough environmental influences acting on the machinery during operation (e.g. unsuitable grounds, slopes or task impacts,...). It is therefore chosen as example for which the concepts and proposed methodologies are presented in this work.

Wheel loaders are widely used in the earth moving industry, equipped with buckets to load trucks with bulk material or to transport it to a designated area. The driver controls the vehicle with a joystick and an accelerator, which moves the shovel and requests the driving speed, respectively. Load trajectory and driving patterns are exclusively dependent on the driver and unknown in advance. Typical loading cycles – such as V or Y-cycles – are repeated periodically for a few times and thereafter the operation is changed to another cycle. In Figure 1.2, a Y-cycle is depicted exemplarily, which comprises of several steps repeated periodically.

(1) Filling lowered bucket

(2) Reverse driving while lifting bucket

(3) Stop for reversion

(4) Forward driving towards load receiver

(5) Emptying lifted bucket

(6) Reverse driving while lowering bucket

(7) Stop for reversion

(8) Forward driving towards pile
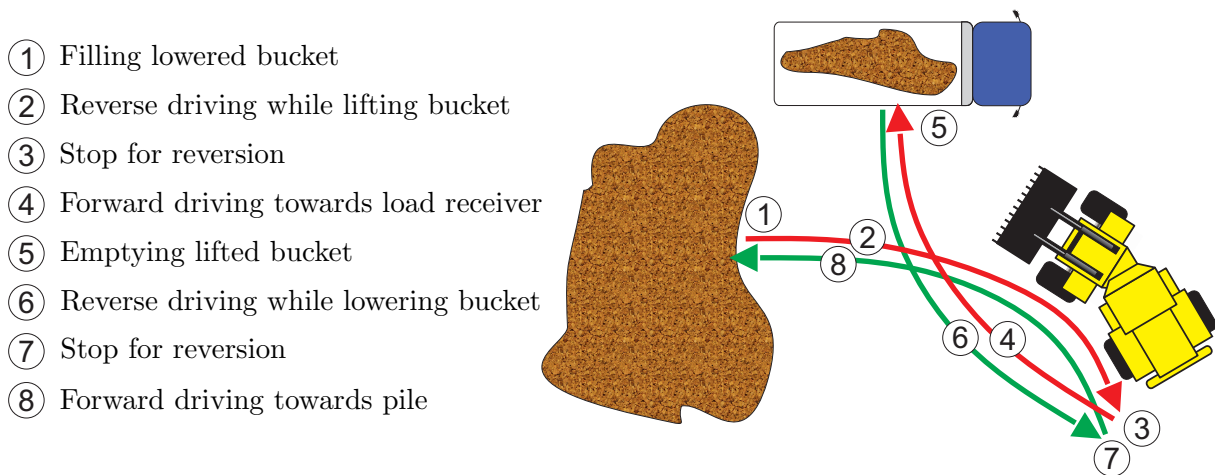
Figure 1.2: Typical duty cycle of a wheel loader.

Filla [35] analyzed different loading cycles to optimize the path trajectory, in order to achieve reductions in fuel consumption and an increase in productivity. However, the periodically operation is observable in the past load signal, which in fact can be considered for the control of the powertrain.

1.3 Configurations of hybrid electric powertrains

Actual developments for conventional powertrains, which usually only consist of an internal combustion engine (ICE), may not be sufficient to reach the low emission and fuel consumption standards requested by the legislative law and customers, respectively. Therefore, a great deal of interest is given to hybridization of non-road vehicles, where the conventional fuel based powertrain is advanced with a secondary energy source to achieve lower fuel consumption and exhaust emissions, respectively. Commonly, an electric energy source such as an electrochemical

battery or double layer capacitor (DLC) is used, though hydraulic concepts are available as well. Meanwhile, distinguished power capabilities are provided by power type batteries, which makes batteries compared to DLCs more attractive to be used within non-road hybrid electric vehicles (HEV) [149]. Hybrid powertrains can be assembled in series or parallel configuration as well as a combination of both, which is depicted schematically in Figure 1.3.
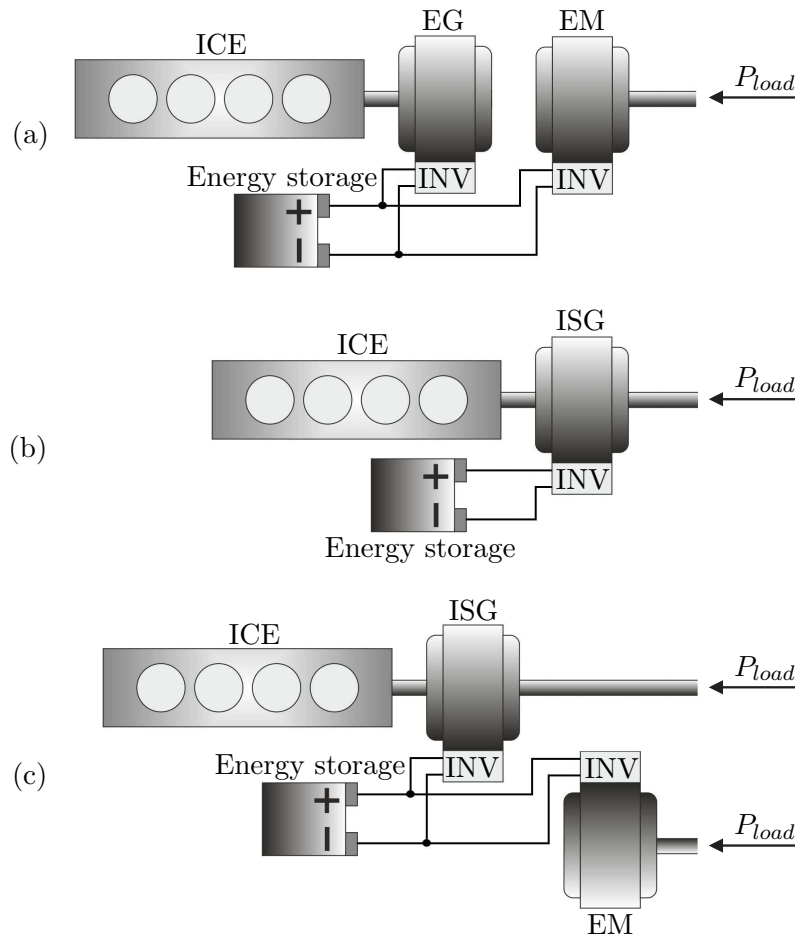
Figure 1.3: Common hybrid configurations used in non-road hybrid electric vehicles. (a) Series, (b) Parallel, (c) Combination of series and parallel.

In Figure 1.3, (a) depicts the series configuration, where no direct form-locking connection between the ICE and the load P_{load} is realized. A secondary energy storage module supplies and receives the power for the electric machines through an inverter unit (INV). Series configuration means to the electric motor (EM) that the full power for the consumer needs to be provided, while the electric generator (EG) may have less power capabilities. In case of high energy conversions, the energy flow must be converted at least two times to reach the consumer, which is disadvantageous. The parallel configuration (b), where ICE and EM are coupled form-locked on one axis, the rotational speed for the ICE and the integrated starter generator (ISG) are the same, while the torques add up. With this configuration, as long as no clutch is used between ICE and ISG, an electric only strategy can not be realized without engine hauling. A combination of series and parallel configuration (c) has the advantage to use electric power for the auxiliary components. Much research interest is spend to analyze the different configurations (see e.g. [165], [7], [76]), while following Kwon et at. [86], the parallel configuration is most favorable for non-road vehicles, though. In Figure 1.4, a parallel hybrid electric powertrain is depicted with the schematic overview of the energy management system (EMS). The depicted powertrain can

be used in different non-road vehicles and applications, while the EMS needs to be especially parametrized for the corresponding vehicles.
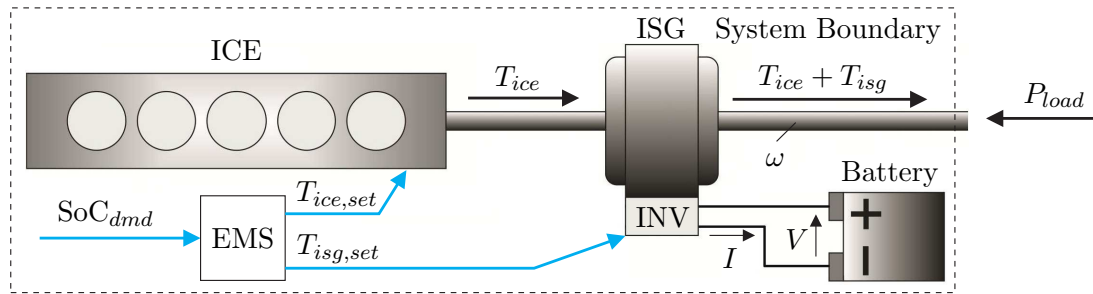
Figure 1.4: Parallel hybrid powertrain to be controlled.

The duty of the EMS is to keep the state of charge (SoC) of the battery at the demand value SoC_{dmd}. This can be achieved by controlling the ICE set-point torque $T_{ice,set}$ and ISG set-point torque $T_{isg,set}$ under consideration of all constraints of the components in such a way that the rotational speed ω is kept at an optimal value while the unknown load P_{load} acts on the powertrain. Underlaid component series controllers apply the set-points to the ICE torque T_{ice} and ISG torque T_{isg}. Battery current I and voltage V attune to T_{isg}, but must be kept below their limits to avoid physical damage. Due to the nonlinearities of the powertrain, achieving an optimal control performance amounts to a nonlinear optimization problem to be solved in the EMS in real time.

1.4 Challenges in control of hybrid electric vehicles

Hybridization can enhance the degrees of freedom of the powertrain to provide the high dynamic load demand of non-road vehicles, but the engine needs to be limited in dynamics according to the downspeeding and phlegmatisation strategies in order to reduce fuel consumption and exhaust emissions. The reduced dynamic tightens to keep all physical constraints of the system, though. Only the information of the entire future load cycle, which is in general unknown for non-road machinery, provides the possibility to reduce the dynamic as far as possible and to exploit the full energy storage capabilities of the battery [101]. An electrochemical battery offers sufficient energy storage capabilities to recuperate regenerative power and consider motor braking phases resulting from an entire load cycle, but the disadvantage of batteries is that the SoC of the battery is not measurable on-line and requires an SoC estimator during operation [118]. In this context, the SoC estimation is only accurate if a precise nonlinear dynamic battery model is used that is capable of the high dynamic loads occurring at non-road vehicles [51]. Such model needs to consider the nonlinear dependency on SoC, temperature and current, as well as many other nonlinear effects such as relaxation and hysteresis [50].

Furthermore, due to the hybridization, system nonlinearities are implicated by the electrical system and the system complexity as well as costs are increased [150]. Minimal costs can only be achieved if the powertrain design is matched with the application [41] and the decrease in fuel consumption and exhaust emissions is significant to reduce the operational costs of the powertrain as well as the acquisition costs for the EATS, respectively. The latter is only achievable if an appropriate framework is available that considers all information in the EMS. Such a framework is provided by a model predictive controller (MPC), which is an advanced method of process control that uses a model of the process to predict the future evolution of the process to optimize the control signal [100]. Due to the nonlinearities of the powertrain, within the MPC a nonlinear optimization problem results, for which an real time implementation in

the hybrid control unit (HCU) is necessary. However, the fast sampling rates intensify the real time requirements and the prediction of the entire future cycle load trajectory is difficult [101].

1.5 Proposed concepts

In this work, methodologies are presented for an efficient control of the described parallel hybrid electric powertrain that is based on the prediction of the future load trajectory as well as for the precise battery SoC estimation during high dynamic operation of a non-road vehicle, respectively. An electrochemical battery is chosen in this work in order to show the applicability of batteries as the secondary energy storage in non-road vehicles.

In the following, first, the functions of a battery management system (BMS) to precisely estimate the SoC are discussed. Thus, a methodology for identification of high accurate battery cell models based on the architecture of local model networks (LMN) is proposed. The global nonlinear model output is obtained by weighted aggregation of the outputs of dynamic local linear models, while the LMN structure is built by an automatic iterative algorithm. Nonlinearities of the battery cell are considered by corresponding inputs that provide sufficient information for the model. Since the LMN approach is only data based, optimal model based design of experiments is proposed to create optimal test sequences, which minimize the variance of the identified parameters of the battery cell model. Based on an optimality criterion, which is determined using the Fisher information matrix, a gradient based algorithm is used for optimization, while constraints of the battery cell are considered to avoid physical damage of the battery cells. Note that due to the data-based approach, the methodology is applicable to different battery cell chemistries and also for DLCs. The obtained LMN battery cell model is then used to built the battery module model for which a SoC estimator based on Kalman filter theory is built. Real measurements are made to verify the battery cell as well as module models and to show their cell chemistry independence. In order to fulfill the dynamic requirements of non-road machinery, a new high dynamic battery cell tester device was developed for the measurements of lithium-iron-phosphate and lithium-polymer battery cells. The real lithium-iron-phosphate battery module has been tested at a battery simulator/tester unit. A special measurement procedure, which is also proposed in this work, was followed exactly to achieve reproducible and comparable measurements.

Second, an real-time capable EMS based on model predictive control is proposed, which primary objective is to minimize the overall energy conversion, fuel consumption as well as exhaust emissions, while constraints are kept to avoid physical damage to the system (safety-related requirements) as well as to enforce that the degrees of freedom are optimally considered (efficiency-related requirements). The EMS consists of a cascaded controller architecture that refers to a linear slave and a nonlinear master MPC, respectively. In the prediction of the future evolution of the process in both MPCs, the unknown future load trajectory is considered by a prediction to increase the control performance as well as to achieve an optimal control during an entire load cycle. Thus, two methodologies for prediction of short term load peaks and the detection of recurrent load cycles are proposed. Bayesian inference is used to statistically predict the short term load based on the available vehicle information such as accelerator position or driving speed, while recurrent load cycles are identified by a cycle detection (CD) that analyzes cyclic correlations within the past load trajectory based on the cross correlation function. Since the electrical system including the ISG and the battery is nonlinear, the optimization problem within the master MPC leads to a nonlinear optimization problem. A relaxation approach is used to solve the problem in real-time, while simplifications are applied. Note that due to the small number of non-road applications, the EMS must be generically applicable to any non-road machinery to minimize the development and implementation costs. In order to guarantee stability of the concept, stability as well as convergence are discussed.

Third, for the example of a wheel loader, as representation of non-road machinery, the EMS is implemented on a real testbed to demonstrate the feasibility of the whole concept including the accurate battery models. The obtained battery module model is implemented at the testbed battery simulator to emulate the battery during the measurements, which are made for different controller adjustments. Three main results are discussed in detail by means of simulation and real testbed measurements:

1. The feasibility of the proposed control concept with respect to the dynamic requirements of the machinery, when downspeeding and phlegmatisation are applied.

2. The optimality of the control approach compared to the conventional powertrain by means of fuel consumption and emissions.

3. The benefit given by the cycle detection to exploit the full energy storage capabilities.

1.6 Main contributions

The following papers of the author form the main contributions of this work:

Paper A

M. QUASTHOFF, J. UNGER, S. JAKUBEK: *Entwicklungsmethodik eines generischen Batterie-Simulationsmodells und dessen Einsatzmöglichkeiten.* 5. Fachtagung Baumaschinentechnik 2012 in Dresden, Baumaschinentechnik 2012 - Energie, Mechatronik, Simulation, Dresden, Schriftreihe der Forschungsvereinigung Bau- und Baustoffmaschinen e.V. (FVB), Heft Nr. 44, pages 263–284, 2012.

In Paper A, the focus lies on the identification of accurate battery models for the application in non-road machinery. The methodology of the local model network applied to battery modeling is given in detail and results without consideration of the temperature in the model are presented.

Paper B

J. UNGER, C. HAMETNER, S. JAKUBEK, M. QUASTHOFF: *Optimal Model Based Design of Experiments Applied to High Current Rate Battery Cells.* IEEE International Conference on Electrical Systems for Aircraft, Railways, Ship Propulsion and Road Vehicles (ESARS 2012 Edition), Bologna, ISBN: 978-1-4673-1371-1, pages 1–6, 2012.

In Paper B, the optimal design of experiments for battery cells without consideration of the temperature is presented in detail. The results show significant increase of model quality due to optimal excitation signals used for the identification of the model parameters.

Paper C

J. UNGER, C. HAMETNER, S. JAKUBEK, M. QUASTHOFF: *A novel methodology for non-linear system identification of battery cells used in non-road hybrid electric vehicles.* Journal of Power Sources, Volume 269, pages 883–897, Elsevier 2014.

In Paper C, the methodology of optimal model based design of experiments and the local model network approach for battery modeling is presented including high current and temperature dependency. Results are shown for lithium-iron-phosphate as well as lithium-polymer battery cells.

Paper D

J. UNGER, M. QUASTHOFF, S. JAKUBEK: *Innovative Energy Management System Using a Model Predictive Controller with Disturbance Prediction for Off-Road Applications.* 16. Antriebstechnisches Kolloquium (ATK 2015), 1. Auflage 2015, pages 427–443, 2015.

In Paper D, the concept of the EMS is presented in the context of non-road machinery and the improvement due to load and cycle prediction is discussed. The focus lies on the non-road machinery and the generically applicability of the methodology.

Paper E

J. UNGER, M. KOZEK, S. JAKUBEK: *Nonlinear model predictive energy management controller with load and cycle prediction for non-road HEV.* Control Engineering Practice, Volume 36, pages 120–132, Elsevier, March 2015.

In Paper E, the energy management system for a parallel hybrid electric powertrain is proposed including the load and cycle prediction. The results measured at the testbed measurements show that a significant reduction in ICE dynamics is feasible and fuel consumption as well as exhaust emissions can be reduced simultaneously by the proposed EMS. The results of Paper C are directly considered within the EMS as well as for the emulation of the battery behavior.

Chapter 2

Battery Management

The battery management in non-road HEV is exposed to higher requirements compared to on-road HEV since higher power densities and load dynamics are usually demanded. For the control of HEV (see Chapter 4), a battery model comprising of the nonlinear effects is required to be used in the controller itself as well as essentially within the battery management system. The state of charge of the battery is not measurable on-line though and needs to be estimated on-line during operation [51]. In this chapter, a generic methodology is proposed comprising of nonlinear system identification and optimal model based design of experiments (DoE) of battery cells, which can be used for battery module modeling and accurate SoC estimation during operation.

2.1 Introduction

2.1.1 Motivation

In many BMS, the open circuit voltage (OCV) of the battery is used to estimate the SoC, which is feasible as long as the battery is not in use. During operation, the nonlinear behavior of the battery voltage comes into effect and big estimation errors occur if only the OCV is used to estimate the SoC [64]. The integration of the battery current is another approach for SoC estimation, which disadvantage is the drift due to the accumulation of current offsets when time increases. Dynamic SoC estimators (e.g. extended Kalman filter) are a powerful way to estimate the SoC, but require a precise dynamic battery model for accurate estimation [118]. Precise battery models describe the nonlinear dynamic behavior of the battery cell terminal voltage accurately by considering nonlinear battery effects such as hysteresis, relaxation and temperature effects. In general, due to the high power densities in non-road HEV, the nonlinear effects of electrochemical batteries are increased [40], which complicates the modeling of the nonlinear battery effects [149]. Note that the used battery model needs to be real time capable in order to be implemented in the BMS, which is in general a trade off between accuracy and complexity.

2.1.2 Cell chemistry dependent system behavior of batteries

The most known cell chemistry is the lead acid cell chemistry, which is used in almost every vehicle to start the engine. Beside of lead acid, there are many other cell chemistries such as e.g. lithium-iron-phosphate ($LiFePO_4$), lithium-polymer (LiPo) or Nickel-Metal Hydride (Ni-MH). However, electrochemical batteries are strongly nonlinear systems, which depend nonlinearly on the SoC, temperature and current, while additional effects such as relaxation and hysteresis are observable. In this context, relaxation refers to the slightly converging battery voltage at

standby or steady state current, while hysteresis refers to a phenomenon in relation to the cell polarization, which causes different shapes of the voltage values during charge/discharge of the battery. Inner chemical reactions may not be observed clearly in the voltage behavior since they occur randomly, but are present and may have an influence to the voltage behavior. Lithium-ion batteries have a higher energy density compared to lead acid batteries and are therefore often used in mobile phones. Ni-MH chemistry has been used for traction batteries of HEV, but more and more traction batteries use the lithium-ion cells. This is not only caused by the higher energy density of lithium-ion cells but also by a smaller referred to as *"memory effect"*, which reduces the capacity if the battery is not fully discharged before being charged again. A comparison of different battery cell chemistries in terms of energy and power capabilities is given in Figure 2.1.
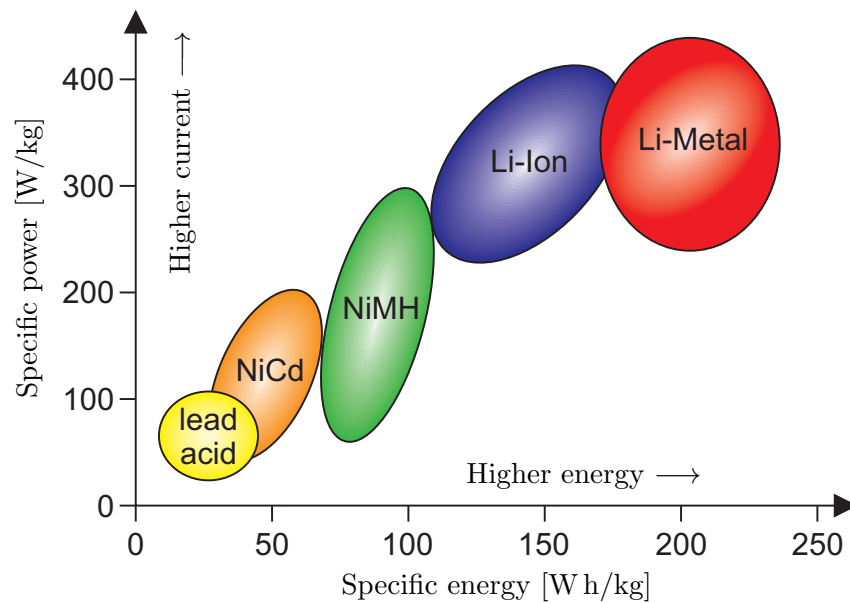
Figure 2.1: Specific energy and specific power of rechargeable batteries.

In general, traction batteries are built by coupling battery cells in serial and parallel connection in order to achieve a desired voltage level (series connection, since voltage add up) or battery capacity (parallel connection, since capacity add up). For the powertrain of non-road vehicles, the power capability of the traction battery is essential, due to which power type battery cells are usually assembled in the battery module. Battery cells can be divided into power and energy cells, while power cells usually have higher power capabilities than the energy density maximized energy cells. The power capabilities of a battery cell can be expressed by the referred to as C-rate, which is a battery capacity independent measure of the current intensity applied to a battery and is obtained by the quotient of current $[A]$ and battery cell capacity $[Ah]$. In non-road vehicles, battery cells must be able to cope with possible C-rates above $20C$, while electric vehicles mostly require larger energy contents. Due to this reason in general power cells are used in non-road HEV.

Furthermore, depending on the cell chemistry, voltage levels and battery behaviors are different, while even the shape of the discharge curve within the same cell chemistry may vary (e.g. lithium-iron-phosphate and lithium-polymer). Also relevant is the voltage level, which is significantly responsible for the overall energy flow and system requirements of the traction battery system. The type of the cell and the geometric structure (e.g. cylindrical, prismatic, ...) mostly define the temperature behavior of the cell. This can be seen at higher C-rates, where the temperature increases significantly and limits the ability of the battery cells to be used in the

high dynamic environment of non-road vehicles. In this context, the energetic efficiency plays a major role for the temperature behavior of the cells and is especially essential in non-road applications. Note here that the energetic efficiency is nonlinearly depending on the history of the battery cell's usage, which is important for the more than 10 years intended product life of a non-road vehicle. For the lithium-ion chemistry, additionally higher safety requirements are relevant, because overcharging with higher voltage may lead to explosion or fire and must be avoided in any case.

2.1.3 Challenges in dynamic battery model identification

In order to use a battery model approach within non-road vehicles, it must be generically applicable to any battery cell chemistry. A general model structure is therefore required that considers nonlinear effects. The nonlinear relations between the voltage and temperature as well as the SoC are unknown in advance and only physical measurable variables are available for parameter identification. In order to identify specific nonlinear effects, long testruns must be performed because the reaction times of batteries are slow. Time consuming and expensive measurements are unacceptable for non-road applications, since the sales volume of non-road machines is low. Data based approaches are methodologies which dependent only on the provided data. The advantage of data based models is that the model is flexible to any cell chemistry, while any model structure can be applied to consider the nonlinearities of the battery cells. On the other hand, the disadvantage is that an appropriate model structure needs to be found and suitable data must be available for parameter identification. Nevertheless, an initial structure can be obtained from expert knowledge and included in the approach. The high dynamic requirement of non-road vehicles challenges especially the test equipment, because high current steps occur during operation. So far, high dynamics are not state-of-the-art in the testing hardware of battery cells. A major role corresponds therefore to the design of experiments, in order to achieve appropriate and reproducible measurements. The reproducibility of battery measurements is depending on the excitation history of the battery and appropriate procedures to clear the cell's short time history must be applied. Though, finding the appropriate procedure is challenging for battery cells, while the case is even more difficult for battery modules due to the cell balancing. In order to gain the maximum information from one testrun, optimal design of experiments can be applied. Optimized test signals are able to achieve sufficient information content in the measurements, but since only the current is applied to the battery cell, in principle a multi-dimensional optimization problem must be solved that consists of only one degree of freedom and multiple effects to be tested.

2.1.4 State-of-the-Art

In the following, the literature known for battery cell modeling, design of experiments, battery module modeling and SoC estimation is reviewed.

Battery cell modeling

Three model approaches have been mainly used in the literature to model the battery behavior:

1. Equivalent circuit models

2. Electrochemical battery models

3. Data-based battery models

In Figure 2.2, the equivalent circuit model (ECM) approach is depicted schematically. Basic electric elements are used to describe the behavior of the terminal voltage, due to which

physically interpretable parameters and real time capability are achieved. Depending on the number of RC-circuits, different time constants are considered in the model. Only one RC-circuit accounting for nonlinear equilibrium potentials, rate- and temperature-dependencies, thermal effects and response to transient power demand is used by Gao et al. [40]. A modified equivalent circuit model is used by Pattipati et al. [113] to estimate SoC, state-of-health (SoH) and remaining useful life in the BMS. Due to the high power density appearing in the automotive industry, solution resistance, charge transfer resistance and Warburg impedance can not be neglected and must be considered within the ECM [44].
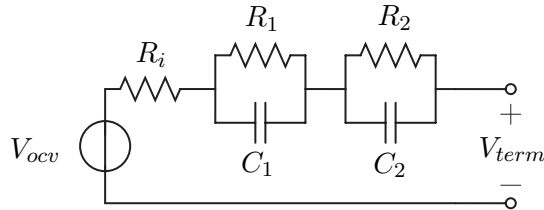
Figure 2.2: Equivalent circuit model with two RC-elements

Electrochemical battery models describe the electrochemical behavior of the battery by chemical reaction equations, which results in a physical model that is computationally intensive. The internal chemical states of the battery are simulated with high accuracy and insight into the system is achieved [82], but in general the model is not real time capable. Concentrated solution theory is used by Doyle et al. [31] to describe lithium-ion battery cells. Klein et al. [82] used partial differential-algebraic equations for state estimation, while a single particle model (SPM) is used by Santhanagopalan et al. [128] to estimate the SoC with an extended Kalman filter. However, the SPM model approach neglects the spatial variation of the states within the battery cell, which questions the validity for the operating region encountered for HEV [20].

Data-based system identification is a powerful approach for modeling and estimation purposes. Model structure and order are easily adaptable, although in general, physical interpretability is not given [82]. In a series of three papers, Plett [116], [117], [118], proposed a SoC estimator based on a data-based nonlinear state space model and an extended Kalman filter. The current direction is considered in the model and hysteresis as well as relaxation are also included by a "hysteresis state" and a low pass filter on the current, respectively. The model is assumed to be cell chemistry independent. Neural networks for battery modeling have been used by [19] and stochastic fuzzy neural networks by [160], [157], [73]. A stochastic fuzzy neural network is also used by Wang et al. [158] for the purpose of modeling the nonlinear dynamics of current, temperature and SoC, while Xu et al. [166] used it for the purpose of SoC estimation.

Hametner et al. [51] obtained a nonlinear battery model due to a local model network, which composes of several local models that are linear in their model parameters and have a certain area of validity defined by validity functions (see e.g. [49], [106], [47]). The nonlinear interpolation of the local linear models (LLM) achieve a nonlinear model output, while the model is constructed by an iterative algorithm. Starting with one global linear model, in each iteration, a LLM is added to the network until a certain threshold is reached (partitioning). Depending on the algorithm's strategy, the validity of the new LLM lies in a specific form in the partition space of the model. In order to identify the model parameters, any model approach requires measurements for parametrization. Battery cells are tested by applying a current excitation signal and recording the voltage response. Depending on the excitation signal, the testing device needs to fulfill certain requirements in terms of dynamics.

Design of experiments

Simple constant discharge and charge cycles are used by Kroeze et al. [85] to identify the parameters of a ECM, while Gao et al. [40], Chen et al. [22] and Hentunen et al. [59] used a discharge pulse excitation signal. Smith et al. [137] used also a discharge pulse excitation signal for the model-based estimation of an electrochemical battery cell model. Charge and discharge mode within a pulse profile have been considered by [66], [63] and [117], in order to identify the parameters for more advanced ECMs (e.g. linear parameter varying models). An asymmetrical current step profile, significantly more dynamic than the other excitation signals, has been used by Hu et al. [65] for the purpose to cover a wide range of SoC as well as a wide range of the current. The dynamic Federal Urban Driving Schedule (FUDS) is mostly used as a validation signal (see e.g. [136], [166], [85], [141]), but in non-road applications the FUDS is rated as an example for low dynamics.

The design of experiments plays an important role, especially for data-based approaches due to the decisive influence of the excitation signal on the parameter estimation [149], [51]. In order to maximize the information content of measurements, model based design of experiments can be used. The idea of model based design of experiments is to use a prior model of the process (reference model), to maximize the information content of measurements in order to identify parameters with minimum variance [122]. A measure for the information content of an excitation signal can be obtained by the Fisher information matrix $\mathcal{I}$ (FIM), which gives the covariance for the parameters estimated from the excitation signal. Based on optimality criteria, the FIM is often used to optimize the excitation signal. Furthermore, depending on the accuracy of the reference model, constraints of the process can be considered in the excitation signal.

Static experiment design based on a local model network generation algorithm is proposed by [56]. Dynamic experiment design for multilayer perceptron networks is proposed in e.g. [24] and [28], where optimal inputs are chosen from a candidate set. Dynamic design of experiments based on multilayer perceptron networks is also centered by Stadlbauer et al. [140], [139]. These papers are used by Hametner et al. [54] to design nonlinear dynamic experiments, which minimize the model variance of dynamic multilayer perceptron networks as well as local model networks. The influence of optimal model based design of experiments on battery modeling, compared to dynamic excitation signals from the literature, is investigated in [149]. Model based design of experiments using a linear dynamic model and predefined current levels is proposed by [51] in order to achieve optimal SoC excitation and minimal measurement duration.

Battery module modeling

The modeling of battery modules is different compared to battery cells since battery balancing needs to be considered [8]. Furthermore, the internal resistance of the battery cell connections as well as the temperature effect on the internal resistance of the battery play major roles in the overall voltage behavior. Lee et al. [87] provided a comprehensive review of joining technologies and processes for automotive lithium-ion battery manufacturing and discussed advantages and disadvantages of the different joining technologies, while corresponding manufacturing issues are mentioned. Since the battery forms a critical part of the HEV powertrain, Sen et al. [131] presents a battery pack model that analyzes the variation of internal resistance as a function of temperature in order to provide the possibilities to design a cost effective and efficient battery management system. Watrin et al. [162] proposed a multiphysical battery pack model along with a test procedure that must be followed to obtain the different model parameters. Based on a screening process that provides a selection of battery cells with similar electrochemical characteristics, in [81], the accuracy of the SoC estimator is increased. Due to the screening process and a parameter comparison, the battery module model can be simplified into a unit cell model that is multiplied with the number of series connected cells. A similar capacity and

resistance screening process is used in [80] to improve the voltage/SoC balancing of a lithium-ion series battery module. Dubarry et al. [32] uses an equivalent circuit technique commonly applied for electrochemical impedance characterizations to describe the behavior of battery cells. These battery cell models are furthermore used to express the behavior of a battery module, while the imbalance of the battery cells are addressed along other effects to improve the battery module model. Battery module model accuracy can be increased significantly if intrinsic cell-to-cell variations in capacity and internal resistance are considered [33]. An estimation of the remaining available power of a battery module, is presented in [119].

State of charge estimation

Many state of charge estimation algorithms are based on the open circuit voltage [88]. Since the relationship between the OCV and SoC is not identical for all batteries, Lee et al. [88] proposed a modified OCV-SoC relationship to increase the SoC estimation accuracy. Commonly an equivalent circuit model is used in combination with an extended Kalman filter (EKF) for the purpose of SoC estimation of batteries (see e.g. [30], [154], [153], [55], [11]), while Santhanagopalan et al. [128] uses an electro-chemical model. A sliding mode observer is applied by [79] to compensate the modeling errors of the used simple resistor-capacitor battery model. Neural networks (NNs) and EKF are used for modeling and SoC estimation in [19]. Chen et al. [23] used the same combination, but also developed a method to consider battery hysteresis effects. An adaptive unscented Kalman filtering method is proposed in [142], which is further compared with an extended and a unscented Kalman filter. He et al. [57] improved the dependence of the traditional filter algorithm on the battery model by an adaptive Kalman filter algorithm. An adaptive Luenberger observer for the SoC that uses an optimized model is built by Hu et al. [62]. For the same purpose, a stochastic fuzzy neural network in combination with an extended Kalman filter for SoC estimation is proposed by [166]. Plett et al. [117] based the SoC estimation also on an EKF, but used a state space structure that considers the dynamic contributions due to open circuit voltage, ohmic loss and polarization time constants.

An alternative to the Kalman filter is the Interacting Multiple Model (IMM) estimator, which has the ability to estimate the state of a dynamic system with several behavior models and switching between them by corresponding rules [103]. The IMM is one of the most cost-effective hybrid state estimation schemes that can act as a self-adjusting variable-bandwidth filter which is widely used for tracking maneuvering targets. Helm et al. [58] used the IMM for a misfire detection that is based on two dedicated parametric Kalman filters. A fusion prediction-based interacting multiple model algorithm is used in [138]. Another application of IMM is hypotheses merging [13]. In the field of vehicle maneuvering, a fuzzy interacting multiple model unscented Kalman filter approach is presented in [75]. Although the IMM approach could be applied for SoC estimation, so far, no papers are known in the literature discussing this topic.

Two different sliding mode observers for dynamic Takagi-Sugeno fuzzy systems are proposed by [9]. A nonlinear filter approach based on local linear models is proposed by [51]. Lendek et al. [90] focused on the stability of cascaded fuzzy systems and observers.

2.1.5 Solution approach

In this chapter, the methodologies are presented to achieve a precise battery cell terminal voltage model for non-road application, which can be applied to estimate the SoC of a battery module with high accuracy during operation.

The model is based on the data-based LMN approach, which advantages are that expert knowledge can be considered, the computational effort is low, a random initialization of the parameters is avoided and the LLMs can be interpreted as local linearization of the process [50], [107]. Nelles et al. [108] proposed the local linear model tree (LOLIMOT) construction

algorithm, which is used to construct the LMN, while corresponding inputs are used to define the LMN structure. In order to consider the battery nonlinearities SoC, relaxation and hysteresis as well as temperature and current in the model, the inputs are adapted. In this context, a physically appropriate network is obtained by adapting the LOLIMOT algorithm to make use of a prepartitioned network and to prohibit splitting within specified dimensions of the network. The resulting battery cell model is applicable to different cell chemistries and real time capable due to the low computational complexity.

Furthermore, optimal model based design of experiments is utilized to achieve high dynamic excitation signals, which cover the entire SoC range during the measurements. Based on the Fisher information matrix $\mathcal{I}$, a scalar cost function $J(\mathcal{I})$ is used to optimize the excitation signal, while the battery cell is sufficiently excited and relaxation, hysteresis as well as current and temperature effects are considered additionally. For this reason, the optimization is furthermore focused on real load ranges that are frequently used in operation. A gradient based algorithm is used to solve the optimization problem, while battery constraints on current, voltage and SoC are considered simultaneously. The obtained excitation signal reduces the identified model parameter variance and maximizes the information content of measurements.

Based on the optimal model based DoE and the LMN approach, the battery module model can be built. A simple approach that multiplies the cell voltage with the number of cells in series connection is compared with the approach proposed in [81], which considers the internal resistance of the battery cell connections as well as an voltage offset. The cell balancing is neglected, because in non-road vehicles mostly a passive cell balancing strategy is used due to the appearing high energy conversions.

An accurate SoC estimation is then achieved for the battery module using the fuzzy observer approach as proposed in [51]. For a straight forward implementation, the battery module model must be transferred into a state space representation with an augmented state vector that includes the SoC. At the end, different choices of process and measurement noise within the filter tuning show the trade off between convergence and accuracy of the filter.

This chapter is organized as follows: First, the battery cell model is developed and an appropriate optimal model based DoE is introduced for the developed battery cell model structure. Second, the temperature model approach is described. Third, different battery module model approaches that are based on the developed battery cell model are discussed. At the end, the SoC estimation for battery modules as well as for battery cells are discussed.

2.2 Data-based identification of nonlinear battery cell models

In this section, the generic methodology for nonlinear identification of high dynamic, current-voltage battery cell models is discussed. Nonlinear battery effects such as SoC, relaxation, hysteresis and temperature as well as current effects are considered by the model. First, the general architecture and structure of LMN is given, followed by the construction of the LMN using the LOLIMOT algorithm. Based on this, the final battery model is developed.

2.2.1 General architecture and structure of local model networks

In principle, the local model network structure is built by local linear models that are only valid in a certain operation regime and interpolated to obtain the global nonlinear model output. An autoregressive with exogenous input (ARX) model structure is chosen for the LLM, by what the regression vector φ follows with the global nonlinear model output $\hat{y}$, the global parameter

vector $\boldsymbol{\theta}$ and the input variables u_l to

$$
\begin{aligned}
\boldsymbol{\varphi}(k, \boldsymbol{\theta}) &= [\bar{\boldsymbol{y}} \ \bar{\boldsymbol{u}}_1 \ldots \bar{\boldsymbol{u}}_q \ 1]^T, \\
\bar{\boldsymbol{y}} &= [\hat{y}(k-1, \boldsymbol{\theta}) \ldots \hat{y}(k-n, \boldsymbol{\theta})], \\
\bar{\boldsymbol{u}}_l &= [u_l(k-d) \ldots u_l(k-d-m_l)], \ l = 1, ..., q,
\end{aligned}
\tag{2.1}
$$

where k is the actual time instant, n is the output order, m_l is the input order of the l-th of q input variables and d is the dead time. Following Nelles et al. [108], the input variables u_l span the so-called input space $\mathcal{Q}$ of the model. The bias is considered by the one in equation (2.1). Note that (2.1) is denoted for MISO systems, but MIMO systems can be modeled as well [107].

One challenge in data-based modeling is the optimal choice of the model order of the inputs and outputs. In [25], different methodologies such as goodness-of-fit (GOF) techniques are recommended to find the optimal model order. GOF from the statistical point of view is discussed in [27]. Akaike's information criterion trades off goodness-of-fit and model complexity and is used in e.g. [168] for the optimal order of an ARX structured battery model. As presented in [69], another methodology is to analyze different selections of the model order and choose the best compromise between complexity and accuracy. To this end, the mean squared error (MSE) provides a basis to make a decision.

The chosen model order is applied to the M LLMs, where the i-th model output $\hat{y}_i$ is obtained by

$$
\hat{y}_i(k, \boldsymbol{\theta}) = \boldsymbol{\varphi}^T(k, \boldsymbol{\theta})\boldsymbol{\vartheta}_i,
\tag{2.2}
$$

where $\boldsymbol{\theta} = [\boldsymbol{\vartheta}_1 \ldots \boldsymbol{\vartheta}_M]^T$ denotes the global parameter vector, which consists of the local parameter vectors $\boldsymbol{\vartheta}_i$ of all M LLM. Weighted aggregation of $\hat{y}_i$ leads to the global nonlinear LMN output

$$
\hat{y}(k, \boldsymbol{\theta}) = \sum_{i=1}^{M} \hat{y}_i(k, \boldsymbol{\theta})\Phi_i(k),
\tag{2.3}
$$

where $\Phi_i(k)$ is the validity function of the i-th LLM. Using a Kernel function $\mu_i(k, \boldsymbol{z})$, which can be any common function (e.g. uniform, triangle,...) [107], the validity function follows by

$$
\Phi_i(k) = \frac{\mu_i(k, \boldsymbol{z})}{\sum\limits_{j=1}^{M} \mu_j(k, \boldsymbol{z})},
\tag{2.4}
$$

where $\boldsymbol{z} = [z_1 \ldots z_\phi]$ span the so-called partition space $\mathcal{Z}$ of the model using the ϕ partition variables [47]. Note that the normalization results from the sum of all validity functions, which is required to be 1. Though input and partition variables may be used in the partition space $\mathcal{Z}$ and input space $\mathcal{Q}$ simultaneously, they are not mandatory the same [60].

2.2.2 Construction of LMN using LOLIMOT

A LMN is usually constructed by algorithms, which iteratively add new LLM to the network. One such algorithm is the local linear model tree algorithm presented in [107]. LOLIMOT searches for the worst LLM by the quadratic error criterion and identifies the dimension in which a split of the model could achieve the best improvement for the global model output. The worst LLM is then axis-orthogonal split into two new models in the dimension with the best improvement [108]. Iteratively, the LMN grows until a certain threshold is reached, which in this work is the maximal number of LLM M.

The parameters for the two new models are determined by weighted least squares (WLS). In case of numerical effects due to significant differences in the input, partition and output variables, all signals used within the algorithm are normalized from 0 to 1 [107]. Schematically,

the LOLIMOT procedure for a two-dimensional partition space is depicted in Figure 2.3. In every iteration, the quadratic evaluation criterion is used to find the worst LLM. The worst model is split into all possible dimensions, while the best alternative, identified likewise with the quadratic evaluation criterion, is chosen.
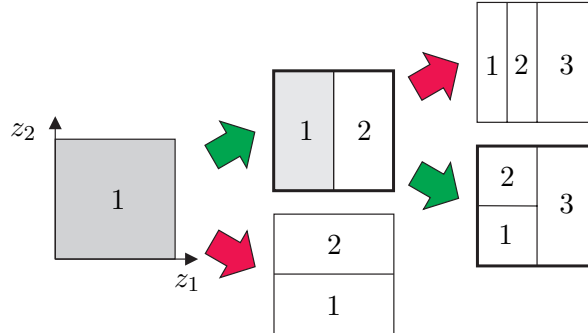

Figure 2.3: LOLIMOT Scheme for two-dimensional partition space

A characteristic of the LOLIMOT algorithm is the Kernel function $\mu_i(k, \boldsymbol{z})$, which is chosen to be Gaussian [107]

$$\mu_i(k, \boldsymbol{z}) = \exp\left(-\frac{1}{2}\left(\frac{(z_1(k) - c_{i1})^2}{\sigma_{i1}^2} + \cdots + \frac{(z_\phi(k) - c_{i\phi})^2}{\sigma_{i\phi}^2}\right)\right). \tag{2.5}$$

Since the partition space $\mathcal{Z}$ is split axis-orthogonal, c_{ij} denotes the center point of the LLM and σ_{ij} is the corresponding individual standard deviation, which is approximated by

$$\sigma_{ij} = k_{\sigma,j}\Delta_{ij}. \tag{2.6}$$

The term Δ_{ij} corresponds to the spread of the LLM, while $k_{\sigma,j}$ is a user-defined sharpness factor that can be interpreted as an overlapping factor of the LLM and influences the smoothness of the nonlinear model output. Note that depending on the specific application as well as the partitioning dimensions, the optimal sharpness factor varies.

Alternative construction algorithms have the same aim, but are different to LOLIMOT. Jakubek et al. [71] used a statistical criteria along with regularization to allow an arbitrary orientation and extent in the partition space of the constructed LMN. In [70], a proper partitioning of the LMN is achieved by an expectation-maximization algorithm that makes use of a residual obtained from generalized total least squares parameter estimation. The advantage of LOLIMOT compared to mentioned alternatives is the low implementation complexity due to the axis orthogonal orientation, for which reason LOLIMOT is used in this work.

2.2.3 Battery cell modeling using LMN

So far, the methodology for battery modeling has been discussed. In the following, the procedure to apply the LMN to battery modeling is presented. Corresponding inputs and the structure for the LMN are presented in order to consider nonlinear battery effects and enhancements for the LOLIMOT algorithm to increase the physical meaning of the battery model. Figure 2.4 depicts an overview of the battery model construction process using a flowchart.

Corresponding LMN inputs of nonlinear battery cell effects

Electrochemical batteries comprise of physical and chemical nonlinear effects. In Figure 2.5, the nonlinear effects can be observed and should be explained in detail in the following.
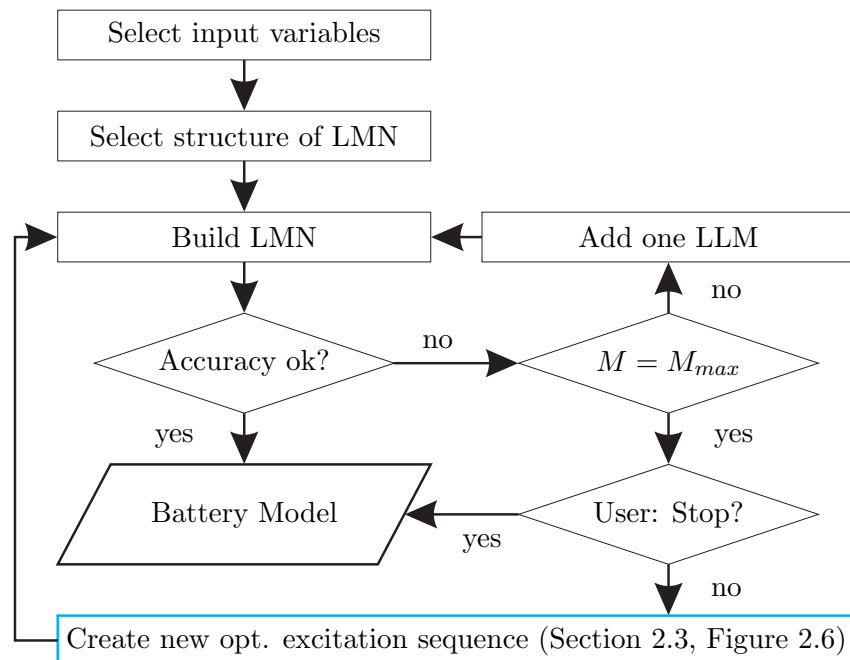
Figure 2.4: Flowchart of battery model construction process.
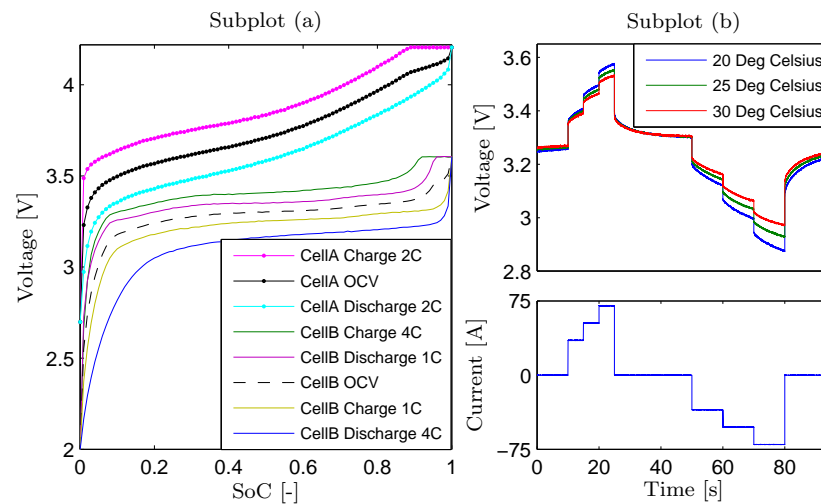

Figure 2.5: **Subplot (a):** Discharge and charge curves for a lithium-polymer (Cell A) and lithium-iron-phosphate (Cell B) chemistry at different currents. The open circuit voltage is estimated by interpolation between the charge and discharge curve.
Subplot (b): Voltage response of a current step sequence, similar to [65], at different temperatures for Cell B.

Constant charge and discharge curves for different C-rates are depicted over the SoC in Subplot (a) of Figure 2.5. Cell $\boldsymbol{A}$ refers to a lithium-polymer chemistry, while Cell $\boldsymbol{B}$ represents a lithium-iron-phosphate chemistry. In order to be able to plot the voltage curves over the SoC, the cell current is integrated [141], while interpolation between the charge and discharge curve provided an estimate for the open circuit voltage [1]. A current step sequence at different temperatures measured for Cell $\boldsymbol{B}$ is shown in Subplot (b).

Distinction must be made between physical and chemical effects. Physical effects are caused by any physical interaction such as an applied current and the resulting temperature increase, while chemical effects arise also without physical interaction such as hysteresis and relaxation. Subplot (b) in Figure 2.5 shows the nonlinear physical influence of current and temperature. Dynamic change in the battery voltage is caused by the applied battery cell current, while the voltage drop is directly influenced by the temperature. Due to the lower/higher temperature, increased/decreased internal resistance of the battery cell is obtained and a bigger/smaller voltage drop is caused. Current as well as temperature are physically measurable on-line and can directly be considered in the model. Hence, the corresponding inputs u_{Current} and z_{Temp} are selected. The time constant of the temperature is significantly higher than the time constant of the current. Due to this reason, the current is included in the input space $\mathcal{Q}$, while the temperature is assumed to be static and is therefore included in the partition space $\mathcal{Z}$. Note that the small temperature gradients compared to gradients of the current underline the assumption.

The nonlinear influence of the SoC on the battery cell voltage is clearly shown in Subplot (a) of Figure 2.5. Since the SoC can not change dynamically or independent to the current, the SoC is considered as corresponding static input z_{SoC}, which is the actual value of the SoC. The value of the SoC is not measurable on-line and needs to be estimated in real batteries (see e.g. [51], [118]). For simulation purposes, the current can be integrated to determine a value for the SoC. Note that in Section 2.6, the SoC estimation is discussed in detail.

Chemical effects are not directly measurable and need to be provided indirectly by corresponding inputs. The slightly to a steady state value converging voltage at standby current in Subplot (b) of Figure 2.5 is referred to as relaxation [117], although, relaxation also acts during current phases [10]. In [117], a low pass filter on the current, which follows certain requirements, is used to model the relaxation, which time constant is significantly different to the one of the current. Following [117],

- after a long rest period and

- during constant-current discharge/charge,

the relaxation state needs to converge to zero, which can be realized by the dynamic corresponding input

$$u_{\text{Relax}} = filt(\Delta u_{\text{Current}}). \tag{2.7}$$

Note that in order to force the filter $filt(\cdot)$ to have zero DC-gain, the change rate of the current $\Delta u_{\text{Current}}$ is used. For lithium-iron-phosphate as well as lithium-polymer chemistry, a third order low pass filter showed to be appropriate, which relaxation time constant is approximated properly on the basis of the voltage converging speed at standby current after a current pulse have been applied to the battery cell.

Different shapes of the charge and discharge curve in Subplot (a) of Figure 2.5 indicate the nonlinear chemical effect referred to as hysteresis [145]. At standby current in Subplot (b) of Figure 2.5, the effect is observable as well. In principle, the hysteresis effect separates the model into a charge and discharge model, which can be achieved by using $sign(\cdot)$ of the current as a corresponding first order hysteresis input z_{Hyst} that is kept at the last value, if the current is zero. As hysteresis is acting statically on the battery behavior, z_{Hyst} is included in $\mathcal{Z}$. Intercalation effects, conductivity of anode/electrolyte/cathode, concentration gradients or

other known chemical effects play a tangential role compared to the mentioned effects and are therefore neglected.

LMN structure of battery cell models

Distinction must further be made between dynamic and static influence on the cell voltage. Dynamic influence of the inputs needs to be considered in the dynamic LLM and must therefore be included in the input space $\mathcal{Q}$, while static influence is important for the partitioning and must therefore be included in the partition space $\mathcal{Z}$. This defines the structure of the LMN and leads to

$$\begin{aligned} \mathcal{Z} &= [z_1\ z_2\ z_3] &\widehat{=}& \quad [z_{\text{SoC}}\ z_{\text{Hyst}}\ z_{\text{Temp}}], \\ \mathcal{Q} &= [u_1\ u_2\ u_3] &\widehat{=}& \quad [z_{\text{SoC}}\ u_{\text{Current}}\ u_{\text{Relax}}]. \end{aligned} \tag{2.8}$$

To this end, the inclusion of the SoC z_{SoC} in the input space $\mathcal{Q}$ implies two advantages. On the one hand side, the continuous change of the voltage depending on the SoC is considered and on the other hand, the observability of the SoC within the model is given, which is required by the SoC estimation with a fuzzy observer (c.f. [51]).

User defined prepartitioning of the LMN structure

In the iterative construction of the LMN, only the quadratic evaluation criterion decides whether to split a model or not. This may lead to physically inappropriate partitions that make a physical interpretation impossible. Due to this reason, LOLIMOT is enhanced to use initial partitions of $\mathcal{Z}$ instead of one global partition. The predefined physically appropriate partitions reduce the computational efforts, while all partitions can be kept physically appropriate if selected dimensions of the partition space are prohibited to be split. This influences the partitioning significantly and needs to be discussed in detail in the following.

Prohibiting a dimension to be split is only appropriate, if a physical reason is given to limit the number of LLM within this dimension. At this point, expert knowledge can be included to improve the model accuracy. The hysteresis input z_{Hyst} refers to the corresponding cell polarization, which can only reach two different states. In this case, an initial split into charge as well as discharge mode and prohibiting to split within this dimension, is advantageous. From Subplot (b) in Figure 2.5, the temperature influence seams to be evenly distributed and therefore three initial partitions are defined for the temperature input. Note that due to the split in the hysteresis dimension, a simultaneous split of charge and discharge mode can not be achieved by definition, because of which partitioning is prohibited within the temperature dimension. The number of initial partitions follows to 6 and the partitioning degree of freedom is limited to the SoC dimension.

2.3   Optimal model based design of experiments

In this section, the optimal model based design of experiments for battery model identification is discussed. The goal of optimal model based DoE is to obtain an excitation signal that minimizes the variance of the identified model parameters. To this end, the system dynamics of a battery cell must be sufficiently excited, while the entire SoC range is covered and relaxation as well as hysteresis effects are considered. The battery system behavior is obtained by applying a load current excitation signal $\boldsymbol{U}$ to the battery cell and recording the cell terminal voltage. In on-road applications, intermediate current steps show sufficient dynamics [65], but in non-road applications higher dynamic excitation signals are required [149].

For that purpose, a methodology to obtain optimal excitation signals for non-road application is proposed. In the following, first, an a-priori available battery model and the Fisher information

matrix $\mathcal{I}$ are used to formulate optimality criteria. Second, a constrained optimization problem is formulated to optimize an excitation signal under consideration of constraints and the nonlinear effects of a battery cell. Note that the information content is further improved by focusing the optimization especially on load ranges frequently used in operation. Third, the optimization by means of a gradient based algorithm is described in detail. At the end, some extensions are made to the obtained optimal excitation sequence to take into account the entire SoC operating range, relaxation, hysteresis and constant current behavior.

2.3.1 Optimization criteria based on the Fisher information matrix

The Fisher information matrix $\mathcal{I}$ is a tool to measure the information content of measurements in terms of the covariance of the estimated model parameters. In order to increase the information content, the system inputs by means of the excitation signal $\boldsymbol{U}$ needs to be modified [54]. The calculation of $\mathcal{I}$ is based on the parameter sensitivity vector $\boldsymbol{\psi}(k)$, which is the partial derivative of the model output with respect to the model parameters. For the LMN approach as described in Section 2.2, $\boldsymbol{\psi}(k)$ follows by

$$\boldsymbol{\psi}(k) = \frac{\partial \hat{y}(k, \boldsymbol{\theta})}{\partial \boldsymbol{\theta}} = \begin{bmatrix} \Phi_1(k)\boldsymbol{\varphi}(k, \boldsymbol{\theta}) \\ \vdots \\ \Phi_M(k)\boldsymbol{\varphi}(k, \boldsymbol{\theta}) \end{bmatrix}, \quad k = 1, ..., N, \tag{2.9}$$

where M denotes the number of LLM and $\Phi_i(k)$, $\boldsymbol{\varphi}(k, \boldsymbol{\theta})$, $\boldsymbol{\theta}$ as defined in (2.4) and (2.1). A reference model is required for the optimization and can be obtained by two possibilities:

- A LMN model is available.

- A different model (no LMN model) or measurements are available.

A LMN with only one LLM describes a linear model of the battery and can be identified easily based on a priori available measurements. In this work, the easy approach of only a linear model is followed to show the significant influence of the methodology to the model quality. Note that a reference LMN can be identified by simulation data created by an available complex electrochemical model, alternatively.

The Fisher information matrix is defined by

$$\mathcal{I} = \frac{1}{\sigma^2} \sum_{k=1}^{N} \underbrace{\frac{\partial \hat{y}(k, \boldsymbol{\theta})}{\partial \boldsymbol{\theta}}}_{\boldsymbol{\psi}(k)} \frac{\partial \hat{y}(k, \boldsymbol{\theta})}{\partial \boldsymbol{\theta}}^T, \quad k = 1, ..., N, \tag{2.10}$$

where σ is the variance of the measurement noise [46]. Denoting $\boldsymbol{\Psi}$ as

$$\boldsymbol{\Psi} = \begin{bmatrix} \boldsymbol{\psi}^T(1) \ldots \boldsymbol{\psi}^T(N) \end{bmatrix}^T, \tag{2.11}$$

the FIM can be expressed by

$$\mathcal{I} = \frac{1}{\sigma^2} \boldsymbol{\Psi}^T \boldsymbol{\Psi}. \tag{2.12}$$

Based on the obtained FIM, in the literature three common scalar criteria are known for the optimization of the excitation sequence. They are formulated as follows [46]:

$$\text{A-optimality: } J_A = \text{Tr}\left(\mathcal{I}^{-1}\right) \to \min_{\boldsymbol{U}} \tag{2.13}$$

$$\text{D-optimality: } J_D = \det\left(\mathcal{I}\right) \to \max_{\boldsymbol{U}} \tag{2.14}$$

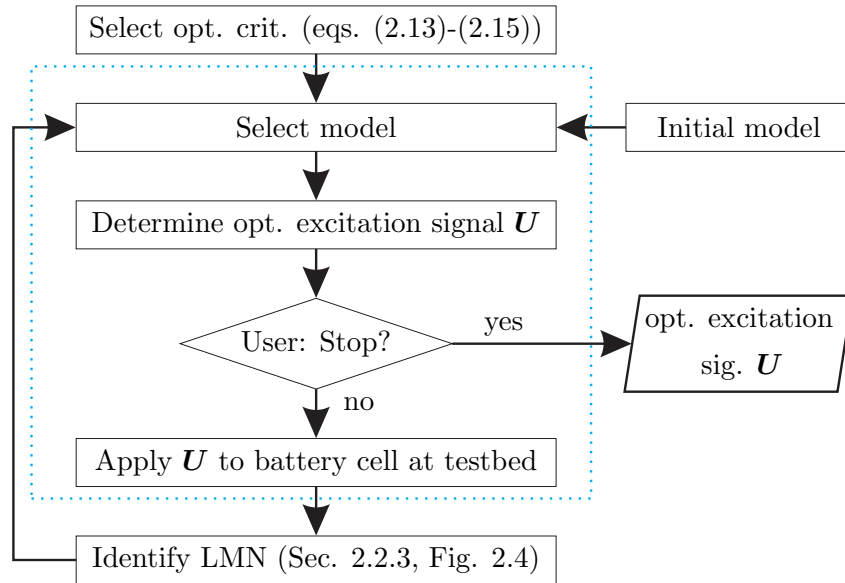$$\text{E-optimality: } J_E = \lambda_{min}\left(\mathcal{I}\right) \to \max_{\boldsymbol{U}} \tag{2.15}$$

Figure 2.6: Process flowchart of the DoE to obtain the optimal excitation signal U. Compare blue block with battery model identification flowchart in Figure 2.4.

A-optimality minimizes the trace of the inverse of the Fisher information matrix, D-optimality corresponds to the maximization of the determinant of the FIM and E-optimality is targeted to maximize the smallest eigenvalue of the FIM. The advantage of D-optimality is the higher sensitivity to single parameter covariances compared to the A-optimality [140].

Following the three common criteria (2.13)-(2.15), Figure 2.6 shows the process to obtain the optimal excitation signal U.

2.3.2 Formulation of the constrained optimization problem

The optimization aims primarily to achieve sufficient high dynamic currents within the excitation sequence, while constraints on current and battery cell voltage are considered. Note that the SoC is limited due to the physical capacity of the battery, which is automatically considered by voltage and current constraints. Constraints must be kept to avoid, among other things, physical damage, accelerated life time reduction, electrolyte oxidation, fire or explosion. Especially the lithium-ion chemistry is sensitive to over charge and over voltage, respectively, which attracts the attention due to safety issues.

The current is furthermore constraint to ranges frequently used in operation to increase the information content especially in ranges used in real applications. Consequential, two possibilities can be used for current constraints:

1. High dynamic excitation between physical minimum and maximum current.

2. High dynamic excitation between load (current) ranges, frequently used in operation.

The first approach simply defines the current constraints at the physical minimum and maximum values, while the second approach defines the constraints using a real load cycle analysis that is realized as follows:

1. Determine the distribution density of the load by a histogram with a defined number of intervals.

2. Set the lower and the upper current constraints corresponding to the interval limits of the histogram.

3. Define the durations within the corresponding constraint ranges by the corresponding distribution densities.

Figure 2.7 shows the load cycle analysis in more detail: Subplot (a) depicts the real load cycle signal for which the analysis is done. The corresponding histogram is shown in Subplot (b) and the resulting current constraints can be seen in Subplot (d). In order to consider output constraints within the experiment design, the reference model must have sufficient accuracy. The used linear reference model is not able to provide such a precision though, which implicate that voltage constraints must be included indirectly through the current. To this end, a limitation ratio for the current depending on the SoC is introduced. Subplot (c) in Figure 2.7 depicts the limitation ratio. Note that the reliability of the output constraints in general depends on the model accuracy and increases with each model update [53]. Nevertheless, due to the maximal current constraints, the maximal deviation of the SoC from the starting SoC value is limited. The SoC limits follow therefore by an adequately chosen starting SoC value.
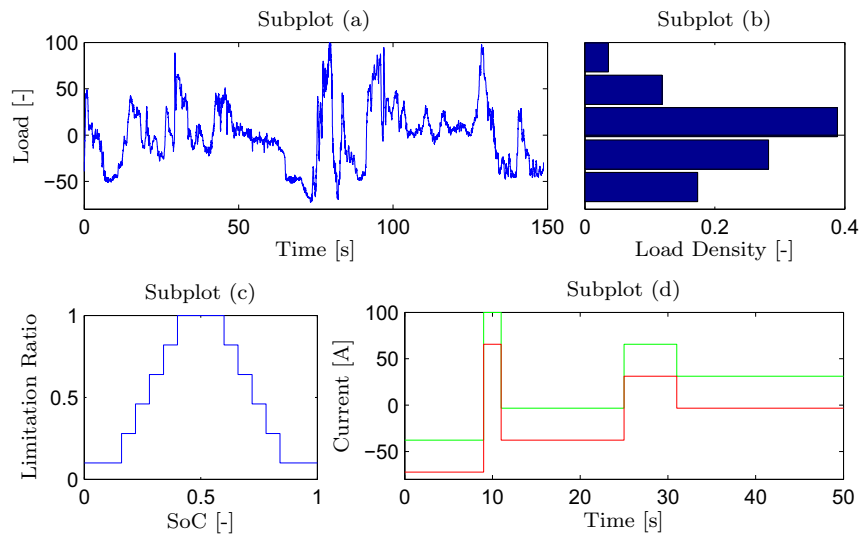
Figure 2.7: Construction of the constraints for the optimization.
Subplot (a): Scaled real load cycle.
Subplot (b): Histogram of the load density distribution of the real load cycle.
Subplot (c): Limitation Ratio of the applied minimal/maximal physical current depending on the SoC.
Subplot (d): Current constraints according to the histogram in Subplot (b). Green: Upper current constraints. Red: Lower current constraints.

On the basis of these constraints, a formulation of the optimization problem can be obtained. Following [122], the D-optimality criterion has higher sensitivity to single parameter covariances and is more invariable to re-parametrization of the model than the A-optimality. Due to this reason, the D-optimality criterion is used to formulate the optimization problem:

$$\text{D-optimality:} \quad \max_{\boldsymbol{U}} \det(\boldsymbol{\mathcal{I}}) \tag{2.16}$$

$$\text{s.t.} \quad \begin{cases} U_{min}(k) \leq U(k) \leq U_{max}(k), \quad k = 1, ..., N \\ \boldsymbol{U} \in \mathbb{R}^{N \times 1} \end{cases},$$

where $U = u_{\text{Current}}$ corresponds to the current input. Note that relaxation input and SoC are directly dependent on the current, which is therefore the only degree of freedom within the optimization.

2.3.3   Constrained optimization

The constraints require to solve the stated optimization problem iteratively. One approach with low computational efforts and sufficient performance is the gradient descent method. The derivative of the design criterion with respect to the input $U(r)$ for all observations N composes the gradient $\boldsymbol{g} = [g(1) \dots g(N)]^T$. In order to obtain the single gradients, the trace of the product of the derivative of the determinant of the FIM with respect to the parameter sensitivity matrix $\boldsymbol{\Psi}$ and the derivative of $\boldsymbol{\Psi}$ with respect to $U(r)$ need to be built, which is computationally intensive [140]. Nevertheless, the r-th observation follows by

$$\frac{dJ_D(\boldsymbol{\Psi})}{dU(r)} = \text{Tr}\left(\frac{dJ_D(\boldsymbol{\Psi})}{d\boldsymbol{\Psi}^T} \frac{d\boldsymbol{\Psi}}{dU(r)} \right), \tag{2.17}$$

where for the D-optimality, the first term is obtained by (cf. [98])

$$\frac{dJ_D(\boldsymbol{\Psi})}{d\boldsymbol{\Psi}^T} = 2J_D(\boldsymbol{\Psi})\boldsymbol{\Psi}[\boldsymbol{\Psi}^T\boldsymbol{\Psi}]^{-1}. \tag{2.18}$$

Note that the inversion of the FIM appears in eq. (2.18), due to which the FIM is required to be a regular matrix with full rank.

The second term in eq. (2.17) is obtained by the single derivatives of the parameter sensitivity vectors with respect to the model input, which are based on the derivative of the regressor $\boldsymbol{\varphi}(k, \boldsymbol{\theta})$ as defined in eq. (2.1) with respect to the input $U(r)$. Denoting the derivative of $\boldsymbol{\varphi}(k, \boldsymbol{\theta})$ by

$$\frac{d\boldsymbol{\varphi}^T(k, \boldsymbol{\theta})}{dU(r)} = \left[\frac{d\hat{y}(k\text{-}1, \boldsymbol{\theta})}{dU(r)} \dots \frac{d\hat{y}(k\text{-}n, \boldsymbol{\theta})}{dU(r)} \quad \delta_{1l}\delta_{(k-1)r} \dots \delta_{pl}\delta_{(k-m_l)r} \ 0 \right], \quad k > r, \tag{2.19}$$

where δ_{ij} is the Kronecker delta function and l corresponds to the current input of the LMN battery model. The former model output with respect to the input $U(r)$ is recursively calculated and follows to

$$\frac{d\hat{y}(k, \boldsymbol{\theta})}{dU(r)} = \frac{\partial \hat{y}(k, \boldsymbol{\theta})}{\partial \hat{y}(k\text{-}1, \boldsymbol{\theta})} \cdot \underbrace{\frac{d\hat{y}(k\text{-}1, \boldsymbol{\theta})}{dU(r)}}_{\text{recursive calculation}} + \frac{\partial \hat{y}(k, \boldsymbol{\theta})}{\partial \hat{y}(k\text{-}n, \boldsymbol{\theta})}\frac{d\hat{y}(k\text{-}n, \boldsymbol{\theta})}{dU(r)} + \frac{\partial \hat{y}(k, \boldsymbol{\theta})}{\partial U(r)}, \quad k > r. \tag{2.20}$$

Based on equations (2.19), (2.20), the derivative of the parameter sensitivity vector with respect to the model input is obtained by

$$\frac{d\boldsymbol{\psi}(k)}{dU(r)} = \begin{bmatrix} \Phi_1(k)\dfrac{d\boldsymbol{\varphi}(k, \boldsymbol{\theta})}{dU(r)} \\ \vdots \\ \Phi_M(k)\dfrac{d\boldsymbol{\varphi}(k, \boldsymbol{\theta})}{dU(r)} \end{bmatrix} + \begin{bmatrix} \boldsymbol{\varphi}(k, \boldsymbol{\theta})\dfrac{d\Phi_1(k)}{dU(r)} \\ \vdots \\ \boldsymbol{\varphi}(k, \boldsymbol{\theta})\dfrac{d\Phi_M(k)}{dU(r)} \end{bmatrix}, \quad k > r, \tag{2.21}$$

while the compact notation of eq. (2.21) yields the second term of eq. (2.17)

$$\frac{d\boldsymbol{\Psi}}{dU(r)} = \left[\frac{d\boldsymbol{\psi}^T(1)}{dU(r)} \dots \frac{d\boldsymbol{\psi}^T(N)}{dU(r)} \right]^T. \tag{2.22}$$

Using equations (2.18), (2.22), the gradient $\boldsymbol{g}$ can be used in the gradient descent method to update the excitation sequence. Considering the current constraints along with an adaptively adjusted step size η, the update follows by

$$\boldsymbol{U}^{(\nu+1)} = \boldsymbol{U}^{(\nu)} + \eta \cdot \boldsymbol{g}^{(\nu)}, \quad \nu = 0, 1, 2, \dots \tag{2.23}$$

$$\text{s.t.} \begin{cases} \boldsymbol{U}_{min} \leq \boldsymbol{U}^{(\nu+1)} \leq \boldsymbol{U}_{max} \\ \boldsymbol{U} \in \mathbb{R}^{N \times 1} \end{cases},$$

which process is repeated until no further improvement is achieved.

Note that the voltage constraints are included indirectly and therefore a nonlinear constrained optimization problem is avoided. Nevertheless, several alternative approaches are known, which include the output constraints directly in the formulation of the optimization problem: The (quadratic) difference between the gradient of the design criterion and the excitation signal increment is minimized by Stadlbauer et al. [140], while the feasible area is approached simultaneously. In order to realize the constrained optimization, Hametner et al. [54] applied Lagrangian multipliers. Sequential quadratic programming (see [96]) and numerical multi-objective optimization (see [133]) are further approaches.

2.3.4 Extensions on the excitation sequence

The previous sections discussed the optimization of the excitation sequence while constraints are considered. For the purpose of especially including the battery specific nonlinear effects, the optimized excitation sequence is extended in the following.

Constant discharge/charge currents with following standby currents are able to reveal the voltage behavior caused by relaxation and to discharge/charge the battery to a desired SoC value. Constant discharge/charge current pulses with subsequent standby current are therefore added in front of/after the optimized sequence. Following the limitation ratio (see Subplot (c) in Figure 2.7), the values of the constant currents are obtained, while the duration of the pulses are related to the longest time constant of the system. Sufficient information about relaxation requires the duration of the standby current to be at least a multiple of the duration of the constant current. An analysis of Subplot (b) in Figure 2.5 leads to a duration ratio of at least 6 for an abated voltage degradation at standby current. Due to this reason, a duration ratio of 8 is suggested and used in this work.

The final excitation signal is obtained by merging the extended high dynamic sequences, while the sequences are created for evenly distributed SoC values across the entire SoC range of interest. Any SoC deviations from the desired SoC are carefully compensated by varying the durations of the constant currents, in order to achieve information across the entire SoC range. Note that the SoC range of interest for different non-road applications differs from each other and therefore may vary.

2.4 Temperature model of battery cells

In order to provide a simulation model, the battery temperature needs to be modeled as well. At high charge and discharge currents the cell temperature increases significantly and may raise above allowable limits [112]. Hu et al, [61] proposed an accurate battery thermal model using a Foster network, which extracts capacitance and resistance from computational fluid dynamics (CFD) results. A simplified mathematical model is presented in [72] that considers heat generations due to joule heating and entropy change, respectively. Sun et al. [143] developed a three-dimensional thermal model to gain a better understanding of the thermal battery cell behavior in a battery module. The more advanced approach considers the battery non-uniform heat generation rate, the battery temperature distribution as well as battery temperature variation across the module in order to predict the temperature behavior during simulated driving cycles. A lumped-parameter thermal model based on a differential equation is developed in [37], which approach is used in this work. Based on the cell thermal capacity c_p and the heat transfer coefficient h_{out}, the temperature behavior of a battery cell can be expressed by

$$c_p \frac{d\vartheta_{cell}}{dt} = h_{out} \left(\vartheta_{amb} - \vartheta_{cell} \right) + I_{cell}^2 R_{int}, \tag{2.24}$$

where ϑ_{amb} is the ambient temperature, ϑ_{cell} is the cell temperature, R_{int} is the internal resistance of the cell model and I_{cell} is the cell current. The battery type (energy or power cell) influences the temperature behavior essentially, since the losses produce heat, which is dissipated through the battery cell. In general, energy cells have a different design, due to which the heat transfer resistance is higher. Nevertheless, as can be seen in equation (2.24), the internal resistance R_{int} is required and needs to be exported from the LMN battery cell. Due to the nonlinear behavior of the battery cell, R_{int} depends on the actual state of the battery cell though.

In this context, the interpretability of the LMN battery model should be discussed in more detail. Due to the physical appropriate partitioning of the LMN, the steady state gain of the LLM can be interpreted as the local internal resistance of the particular LLM. Note that the calculated steady state gain is normalized and needs to be transformed first before it can be interpreted as physical value. In Figure 2.8 in the upper two subplots, the identified internal resistances for Cell $\boldsymbol{A}$ and Cell $\boldsymbol{B}$, respectively, are shown for different temperatures. Since the partition space is three-dimensional, the current is hold at $I_{cell} = -40\ A$ to be able to depict a two-dimensional representation of the parameters. The lower two subplots show the identified open circuit voltages in comparison with an OCV that is obtained from an interpolation of the charge and discharge curve at $2C$. As can be seen, the OCV is precisely identified, though the excitation signal has been highly dynamic and included only few standby phases during the measurements. Based on this interpretation, look-up tables for the internal resistance R_{int} and the OCV V_0 can be exported from the LMN and used in equation (2.24).

2.5 Battery module model design

Battery module models are required for the simulation of powertrain concepts in hybrid electric vehicles as well as for the implementation in battery simulators, which emulate the real battery behavior at the test bed. Real time capability is especially necessary for the implementation in battery simulators. Nevertheless, battery modules consists of multiple battery cells connected in series and parallel connections, which results in a required monitoring system that observes the voltage and SoC balance between the battery cells to avoid physical damage. The balancing strategy needs to be included in a battery model, as long as there is an effect during operation. Due to this reason, in the following cell balancing in battery modules is reviewed before the design of the LMN based battery module model is discussed.

2.5.1 Battery cell balancing in battery modules

Battery balancing refers to the equalization of the state of charge of the battery cells within a battery module to avoid overcharge, which might cause physical damage and safety issues due to explosion and fire. Cao et al. [18] presents the theory behind balancing methods for battery systems within the past twenty years and groups their nature of balancing. In general, two different balancing techniques are known [3]:

1. Active balancing

2. Passive balancing

Active balancing draws the energy from the most charged cell and transfers the energy through DC-DC converters to the least charged cells. Lee et al. [89] e.g. proposed an active balancing algorithm for lithium battery modules. Passive systems waste energy from the most charged cell as heat, until the cell charges are equalized. To this end, the balancing strategy needs to be considered in the battery module model, if cell balancing is carried out during operation and has an influence on the voltage behavior.
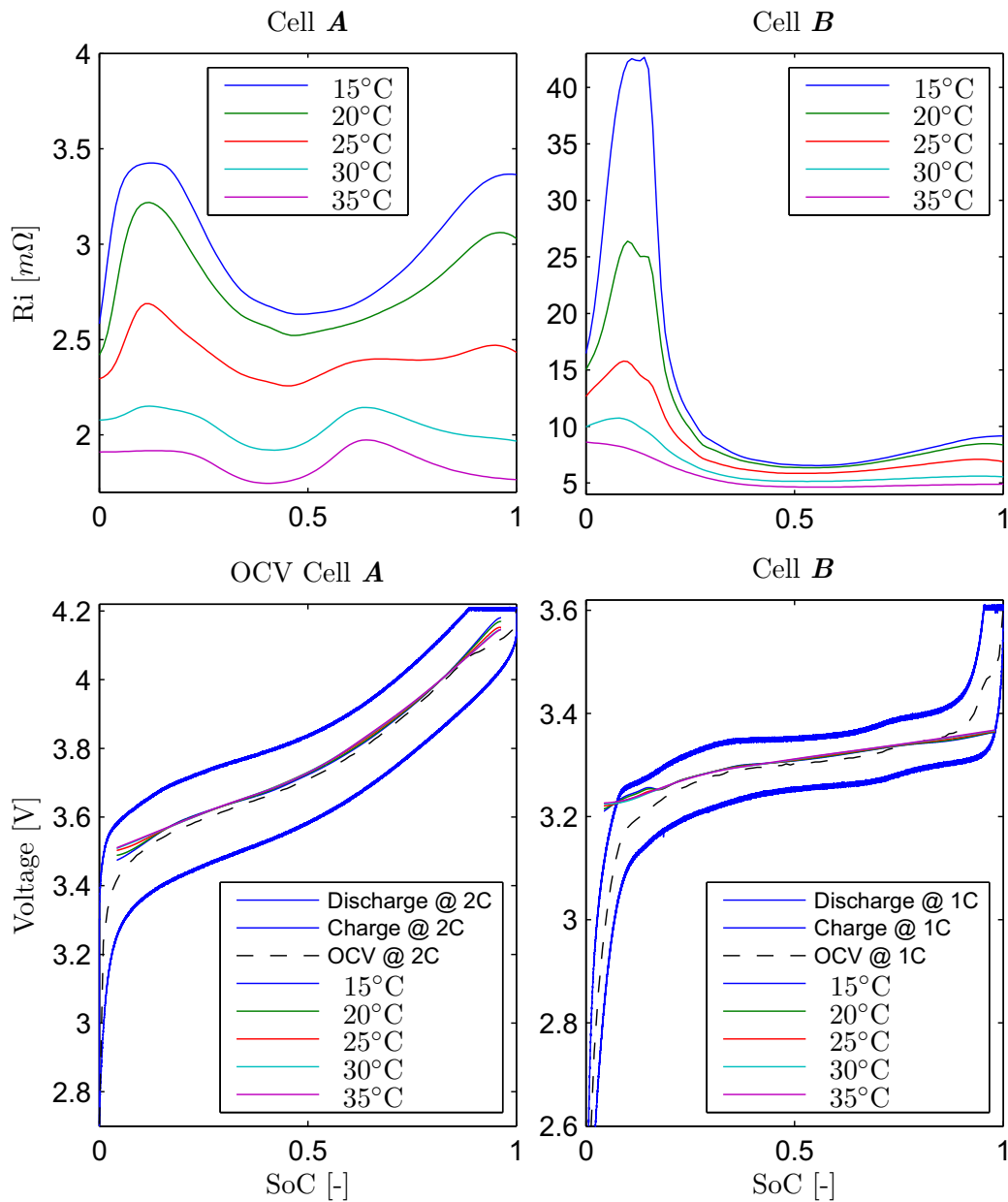
Figure 2.8: Interpretability of LMN battery model parameters shown at Cell **A** and Cell **B**. The current dimension is hold at $I_{cell} = -40\ A$.

In this work, a battery module with implemented passive balancing system is used. Thus, balancing is neglected in the proposed model approach. Nevertheless, different balancing strategies and their implementation in battery models are discussed in e.g. [8], [26], [164].

2.5.2 LMN based battery module design

In non-road vehicles, the voltage level of battery modules is usually high, because the current capabilities of electrochemical batteries for high power demands are in general limited. Thus often super capacitors are used due to their significantly larger power capabilities. Nevertheless, the higher energy densities of batteries make them an equal alternative. During the design process of hybrid electric powertrains, the planned battery module may not physically available. This complicates the design of battery module models, since a sufficient parametrization is difficult. To this end, four different approaches of battery module model approaches Σ_i are discussed in the following, in order to show the influence of different considered effects.

Battery cell measurements are easier to realize and therefore a battery module model that is based on battery cell models is desired and advantageous. The proposed methodology in the previous sections provides LMN battery cell models that can easily be obtained by cell measurements, but does not consider the additional internal resistance of battery modules resulting from the cell connections. Nevertheless, the internal resistance is unknown in advance and therefore a first obvious model approach is

$$V_{module,\Sigma_1} = n_{cells} \cdot V_{cell}, \tag{2.25}$$

where n_{cells} is the number of series connected cells and V_{cell} refers to the battery cell voltage. The battery cell voltage V_{cell} can be obtained by the LMN battery cell model using the battery cell current

$$I_{cell} = \frac{I_{module}}{p_{cells}}, \tag{2.26}$$

where p_{cells} is the number of parallel connected cells and I_{module} is the battery module current. Note that the internal resistances of the battery cell connections are not considered in this simple approach and may limit the accuracy, but therefore, no information about the internal resistance of a battery module is required.

Considering the internal resistance of the battery module in V_{module,Σ_1} leads to model Σ_2

$$V_{module,\Sigma_2} = n_{cells} \cdot V_{cell} - R_{int,\Sigma_2} \cdot I_{module}, \tag{2.27}$$

where R_{int,Σ_2} refers to the internal module resistance. Battery cells usually vary in nominal cell voltage, which can be considered by an offset voltage. Module model approach Σ_3 follows therefore to

$$V_{module,\Sigma_3} = n_{cells} \cdot V_{cell} - R_{int,\Sigma_3} \cdot I_{module} + V_{offset,\Sigma_3}, \tag{2.28}$$

where the offset voltage V_{offset,Σ_3} also considers measurement sensor offsets and any other additional influences on the module voltage. Electrical resistances are usually linear elements, but a current dependent adaptation of the internal resistance and offset, respectively, have been shown as advantageous. This can be caused by e.g. inaccuracies in the battery cells, different ages of the installed battery cells or the battery cell used to identify the battery cell model. Nevertheless, the resulting model can be denoted by

$$V_{module,\Sigma_4} = n_{cells} \cdot V_{cell} - R_{int,\Sigma_4}^{\pm} \cdot I_{module} + V_{offset,\Sigma_4}^{\pm} \tag{2.29}$$

with

$$R_{int,\Sigma_4}^{\pm} = \begin{cases} R_{int,\Sigma_4}^{+} & \text{if} \quad I_{module} > 0 \\ R_{int,\Sigma_4}^{-} & \text{if} \quad I_{module} \leq 0 \end{cases}, V_{offset,\Sigma_4}^{\pm} = \begin{cases} V_{offset,\Sigma_4}^{+} & \text{if} \quad I_{module} > 0 \\ V_{offset,\Sigma_4}^{-} & \text{if} \quad I_{module} \leq 0 \end{cases}. \tag{2.30}$$

Battery module measurements can then be used to identify the module parameters R_{int,Σ_i} and V_{offset,Σ_i}, respectively.

2.6 State of charge estimation

State estimation is required, if system states are not measurable. An observer is used to estimate the unmeasurable states based on the measurable states and a dynamic model of the process. In this context, the observability of the system must be given, which is the case if the observability matrix $\mathcal{O}$

$$\mathcal{O} = \begin{bmatrix} \boldsymbol{C} \\ \boldsymbol{CA} \\ \boldsymbol{CA}^2 \\ \vdots \\ \boldsymbol{CA}^{n_{states}-1} \end{bmatrix}, \tag{2.31}$$

where n_{states} denotes the number of states in the state space system with state matrix $\boldsymbol{A}$ and output matrix $\boldsymbol{C}$, has full rank.

The linear Kalman filter is an efficient recursive filter that is able to observe the internal states of a linear dynamic system by measurements corrupted with noise. Advantageous is that the filter is based on time-invariant models, which reduces the computational complexity significantly. Nonlinear processes are in general more challenging, since nonlinear estimation approaches need to be applied. A well known nonlinear estimator is the extended Kalman filter, which is based on the local Jacobian of a nonlinear model and is therefore more complex than a linear Kalman filter. Note that the filter gain as well as the data dependent local linearization of the EKF cannot be precalculated, which is disadvantageous for real time application [117], [154]. The interacting multiple models approach achieves a nonlinear estimation by running separate linear Kalman filters and switching between the filters based on a detection scheme using the validity probability of the underlying models [103], [58]. Another similar nonlinear estimator, which is ideal in combination with LMN models, is the fuzzy observer [21], [132]. Since each LLM of the LMN corresponds to an linear time-invariant dynamic system, the linear Kalman filter theory can be applied and the global filter output can be obtained by weighted aggregation of the local filters [134]. Furthermore, stability of the fuzzy observer can be shown based on Lyapunov stability theory and is discussed in e.g. [102], [144]. The fuzzy observer approach is therefore used in this work.

In the following, the general architecture of the SoC estimation scheme is presented, before the fuzzy SoC observer is developed. Note that the SoC estimation approach is applicable for cell and module SoC estimation, respectively, and is therefore developed for the general case.

2.6.1 General architecture of the SoC observer scheme

The estimation of the SoC of a battery can be obtained by two practical principles. First, measuring the open circuit voltage leads to an accurate estimate of the SoC if the battery has been in standby mode for a sufficiently long period of time, but can not be used during operation. The second possibility is to integrate the current, which can be denoted by

$$\text{SoC}(t) = \text{SoC}_{init} + \frac{1}{Q_{c,batt}} \int_0^t \eta_{batt,cou}(I_{batt}(\nu)) \, I_{batt}(\nu) d\nu, \tag{2.32}$$

where SoC_{init} is the initial SoC, $Q_{c,batt}$ is the battery capacity and $\eta_{batt,cou}$ is the charge efficiency. Note that $\eta_{batt,cou}$ is usually 0.99 and can be neglected for the purpose of observer based SoC estimation. Nevertheless the integration of the current leads to an acceptable initial SoC value that can be used in an advanced SoC observer scheme.

Following [51], the estimation of the SoC can be done by automated nonlinear observer design using a fuzzy observer. In this context, the relative SoC estimation given by eq. (2.32) should be included in the observer scheme. For that purpose, eq. (2.32) is represented in the discrete formulation

$$\text{SoC}(k) = \text{SoC}(k-1) + \frac{t_{s,bms}}{Q_{c,batt}} I_{batt}(k), \tag{2.33}$$

where $t_{s,bms}$ corresponds to the sampling time. An overview of the observer scheme is depicted in Figure 2.9 exemparlily. As can be seen in the figure, the SoC is corrected by the observer, which obtains the simulated battery voltage by the LMN battery model discussed in Section 2.2. Any drift of the SoC due to extended operational time is compensated since the SoC estimator is able to act during operation. Note that the estimation accuracy is mainly dependent on the battery model accuracy. In the next subsection, the SoC fuzzy observer is developed in detail.
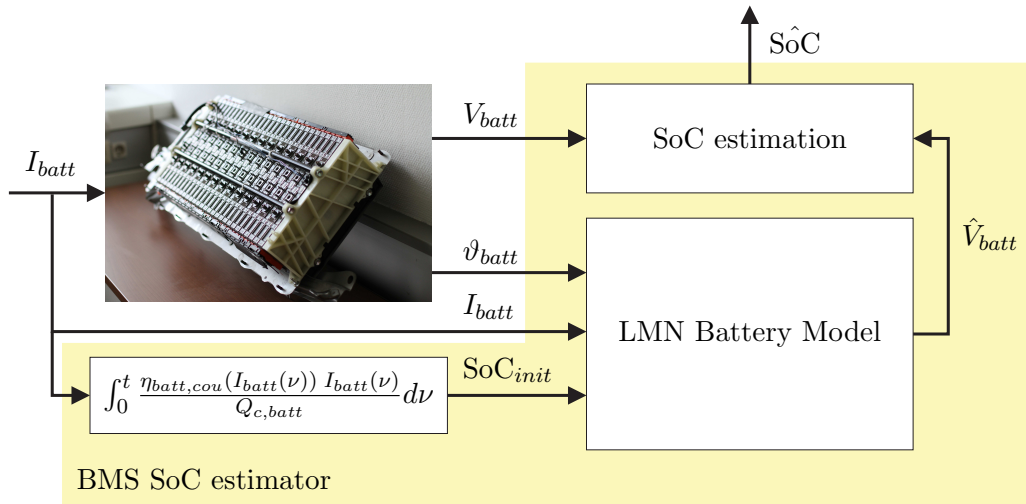

Figure 2.9: SoC fuzzy observer scheme

2.6.2 SoC fuzzy observer design

The automated nonlinear observer design requires the nonlinear LMN in state space (SS) representation [132], which state vector needs to be augmented in order to consider the initial SoC from the current integration in the fuzzy observer. A correct transformation of the LLM (c.f. eq. (2.2)) into the SS-representation can be achieved by including the past outputs y and the previous state of charge $\text{SoC}(k-1)$ in the augmented state vector $\boldsymbol{x}_{aug}$, which follows to

$$\boldsymbol{x}_{aug}(k) = \begin{bmatrix} y(k-1) \\ y(k-2) \\ \vdots \\ y(k-n) \\ \text{SoC}(k-1) \end{bmatrix}. \tag{2.34}$$

The parameter vector of the i-th LLM can be be denoted by

$$\boldsymbol{\vartheta}_i = \begin{bmatrix} a_{1,i} & \cdots & a_{n,i} & b_{11,i} & \cdots & b_{lm_l,i} & \cdots & b_{qm_q,i} & b_{0,i} \end{bmatrix}, \tag{2.35}$$

where $a_{.,i}$ and $b_{.,i}$ denote the output and input parameters, respectively, while $b_{11,i} = b_{\text{SoC},i}$ corresponds to the order-one SoC input parameter used in the LMN design (cf. eq. (2.8)). Note that the LMN design described in Section 2.2.3 already includes the SoC as input variable, in

order to be able to use the identified parameter for the augmented state variable in the design of the linear Kalman filters. Using these parameters, the state matrix $\boldsymbol{A}_i$ can be established by

$$\boldsymbol{A}_i = \begin{bmatrix} a_{1,i} & a_{2,i} & \dots & a_{n,i} & b_{\text{SoC},i} \\ 1 & 0 & \dots & 0 & 0 \\ 0 & 1 & \dots & 0 & 0 \\ \vdots & \vdots & \ddots & \vdots & \vdots \\ 0 & 0 & \dots & 0 & 1 \end{bmatrix} \tag{2.36}$$

and the input matrix $\boldsymbol{B}_i$ follows by

$$\boldsymbol{B}_i = \begin{bmatrix} b_{21,i} & \cdots & b_{lm_l,i} & \cdots & b_{qm_q,i} & b_{0,i} \\ 0 & 0 & 0 & 0 & 0 & 0 \\ \vdots & \ddots & \vdots & \ddots & \vdots & \vdots \\ \frac{t_{s,bms}}{Q_{c,batt}} & 0 & 0 & 0 & 0 & 0 \end{bmatrix}, \tag{2.37}$$

where $b_{0,i}$ corresponds to the local affine term (bias term). Note that the corresponding parameter of the SoC input $b_{11,i} = b_{\text{SoC},i}$, is excluded from $\boldsymbol{B}_i$ since it is already considered in $\boldsymbol{A}_i$. The augmented input vector for the augmented observer SS model follows then to

$$\boldsymbol{u}_{aug}(k) = \begin{bmatrix} u_1(k) \\ u_1(k-1) \\ \vdots \\ u_q(k-m_q) \\ 1 \end{bmatrix}, \tag{2.38}$$

where u_i corresponds to the actual and past elements of the model inputs. At this point it is important to mention that the integrator needs to be adapted if the a normalization of the LMN is used. In case of scaled parameters, the integrator increment can be transformed by a corresponding additional term in the last row and column of the matrix $\boldsymbol{B}_i$.

Using equations (2.34)-(2.38), the augmented state equation

$$\boldsymbol{x}_{aug}(k) = \sum_{i=1}^{M} \Phi_i(k-1) \left\{ \boldsymbol{A}_i \boldsymbol{x}_{aug}(k-1) + \boldsymbol{B}_i \boldsymbol{u}_{aug}(k) \right\} \tag{2.39}$$

leads to the global model output

$$y(k) = \boldsymbol{C} \boldsymbol{x}_{aug}(k) \tag{2.40}$$

with

$$\boldsymbol{C} = \boldsymbol{C}_i = \begin{bmatrix} 1 & 0 & \dots & 0 & 0 \end{bmatrix}. \tag{2.41}$$

Based on these equations, the local steady-state Kalman filters can be designed for each local linear model, while the global filter is obtained by weighted aggregation of the individual local estimates. The state estimate $\hat{\boldsymbol{x}}_{aug}$ of the global filter can be determined based on the gain matrix $\boldsymbol{K}_i$ by

$$\hat{\boldsymbol{x}}_{aug}(k) = \sum_{i=1}^{M} \Phi_i(k-1) \left\{ \boldsymbol{x}_{aug,i}^*(k) + \boldsymbol{K}_i \left[y(k) - \hat{y}(k) \right] \right\}, \tag{2.42}$$

with

$$\boldsymbol{x}_{aug,i}^*(k) = \boldsymbol{A}_i \hat{\boldsymbol{x}}_{aug}(k-1) + \boldsymbol{B}_i \boldsymbol{u}_{aug}(k), \tag{2.43}$$

where

$$\hat{y}(k) = \sum_{i=1}^{M} \Phi_i(k-1)\boldsymbol{C}\boldsymbol{x}_{aug,i}^*(k). \tag{2.44}$$

The gain matrix $\boldsymbol{K}_i$ is calculated by

$$\boldsymbol{K}_i = \boldsymbol{A}_i\boldsymbol{P}_i^T\boldsymbol{C}^T\left(\boldsymbol{C}\boldsymbol{P}_i^T\boldsymbol{C}^T + \boldsymbol{R}^T\right)^{-1}, \tag{2.45}$$

where $\boldsymbol{P}_i$ refers to the solution of the discrete-time algebraic Riccati equation (DARE)

$$\boldsymbol{A}_i\boldsymbol{P}_i\boldsymbol{A}_i^T - \boldsymbol{P}_i - \boldsymbol{A}_i\boldsymbol{P}_i\boldsymbol{C}^T\left(\boldsymbol{C}\boldsymbol{P}_i\boldsymbol{C}^T + \boldsymbol{R}\right)^{-1}\boldsymbol{C}\boldsymbol{P}_i\boldsymbol{A}_i^T + \boldsymbol{Q} = 0. \tag{2.46}$$

In eq. (2.46), the matrices $\boldsymbol{R}$ and $\boldsymbol{Q}$ reflect the covariance matrices of the measurement and process noise, respectively. The Kalman filter theory assumes $\boldsymbol{R}$, $\boldsymbol{Q}$ to be known, but often the covariance matrices are unknown and $\boldsymbol{R}$, $\boldsymbol{Q}$ are used as tuning parameters [51]. For the application of SoC estimation in batteries, the terminal voltage measurement noise $\boldsymbol{R}$ can be found by experiments. The process noise $\boldsymbol{Q}$, similar to [154], is used to tune the filter and no correlation between the different elements in $\boldsymbol{Q}$ is assumed.

Chapter 3

Results for BMS in Non-Road Vehicles

The battery management system of batteries used in non-road vehicles needs to be able to provide an accurate value of the SoC, even during operation if high dynamic currents act on the battery. This can be achieved based on the generically applicable methodologies proposed in Section 2. In this chapter, the proposed concepts and methodologies are validated using measurements from real battery cells with different cell chemistries as well as a battery module. The battery module is established with battery cells, which are separately available to be investigated with cell measurements.

In the following, first, the measurement procedures and hardware are specified. Second, the results for the nonlinear battery cell model identification are discussed. Third, the results for the temperature and battery module model are validated and at the end, the estimation accuracy achieved with the SoC estimator introduced in Section 2.6, is demonstrated.

3.1 Generation of reproducible high dynamic data sets

The reliability of precise battery models depend on the data set used to identify the model parameters. Due to this reason, the reproducibility of measurements is essential for the whole methodology, since only reproducible measurements can verify the model accuracy. In the following, the measurement procedure is discussed and the measurement hardware is described. At the time, when battery cell measurements were required, an affordable and sufficiently high dynamic battery cell tester was not available and therefore a cell tester hardware has been developed. Measurements on a real battery module could be achieved using an adapted battery simulator available at the test bed also used to measure the hybrid powertrain (cf. Section 5). In the following, the measurement procedures are introduced before the developed battery cell tester as well as module tester are described in detail.

3.1.1 Measurement procedures

Electrochemical batteries show that the previous excitation has influence on the voltage behavior of the cells. Reproducibility can only be guaranteed, if the initial battery conditions are uniquely defined in advance to the measurements. Unexpected and undefined appearing effects are avoided and all short term history of the battery cells (cell conditioning) is erased. It has been shown that the following procedure enables to compare measurements as well as different battery cells and chemistries, respectively, with each other:

1. Initial capacity check at 25 °C

2. Set temperature of climate chamber

3. Fully charge the battery cell

4. Discharge until initial SoC is reached

5. Apply excitation signal

6. Repeat 3 to 5 until all excitation signals are recorded

7. Repeat 2 to 6 until all temperatures are recorded

Since the exact capacity of a battery cell is in advance unknown, the initial capacity check (see enumeration 1) is applied only once before any dynamic measurements are taken. Eight charge/discharge cycles with different C-rates from $4C$ to $1C$ are applied to the battery cell, due to which the short term history is reduced and the true capacity can be calculated. Due to the high C-rates, the full capacity of a battery cell can not be exploited, because of which only the last cycle is used to calculate the capacity. The difference between the quotient of discharge capacity divided by charge capacity can additionally be used to obtain a charge efficiency for each cycle. Any battery cell measurements obtained in this work are based on this procedure.

In case of battery modules, the capacity check is due to the cell balancing more difficult. Nevertheless, in order to achieve the best reproducibility possible, the battery module is fully charged and balanced before the battery module is discharged to the demanded initial SoC. Prior to the measurements, a conditioning cooling circuit established the demand temperature of the battery module.

3.1.2   Test hardware for battery cells

High dynamic current excitation signals such as real load profiles are so far not state-of-the-art, which implicates that high dynamic battery cell testers with reasonable price are unavailable. Due to this reason, a battery cell tester is developed based on a Hoecherl&Hackl source/drain module for closed-loop current control and a National Instruments USB data acquisition board for the measurements. A LabView control software executed the measurement procedure, kept any physical constraints and monitored battery states and safety issues. The voltage range is $-1\,\text{V}$ to $10\,\text{V}$ and the current range is $\pm240\,\text{A}$. A Vötsch climate chamber, also triggered by the LabView control software, provided an ambient temperature between $-20\,°\text{C}$ and $60\,°\text{C}$ (relevant temperature range for non-road application is between $12.5\,°\text{C}$ and $35\,°\text{C}$). Note that the system is designed for up to $10\,\text{kHz}$ with step response time constants of the source/drain module for less than $200\,\mu\text{s}$. Due to the slow system behavior of battery cells, the measurement duration is very long and an enormous amount of data is generated, if the sampling time is chosen too high. Any voltage response from the applied excitation signals as well as the cell temperature are therefore recorded with a sampling rate of $100\,\text{Hz}$. In Figure 3.1, the battery cell tester (left) and the climate chamber (right) are depicted.

3.1.3   Test hardware for battery modules

A battery simulator (KS BattSim) from Kristl, Seibt & Co GmbH, usually designated to emulate battery models in real time, is adapted to test the available real battery module. The battery simulator has a voltage range from $500\,\text{V}$ to $750\,\text{V}$ and a current range of $\pm250\,\text{A}$. These specifications are sufficient for the battery module measurements and the emulation of the battery module during the hybrid powertrain test bed measurements. The current excitation signal is directly programmed into the control unit of the battery simulator and an implementation of high dynamic excitation signals is possible. Depending on the purpose of the battery simulator,
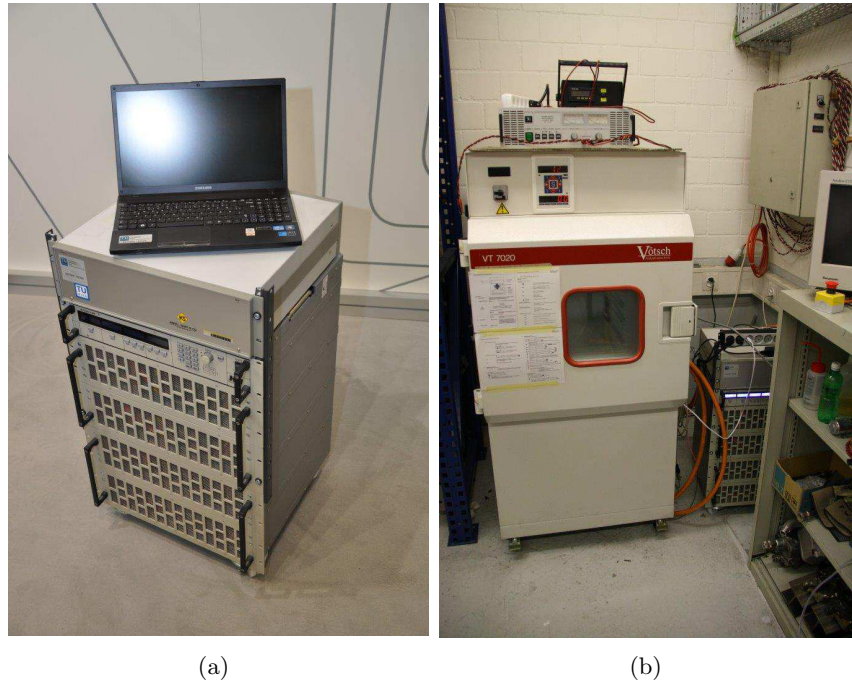
<center>(a)   (b)</center>

Figure 3.1: Battery cell tester (left) and climate chamber (right) used to test different cell chemistries and temperatures.

the control interface is changed. In Figure 3.2, the battery simulator and the real battery module are depicted.

3.2   Battery cells and battery module specifications

The presented methodologies are data-based approaches that are generically applicable to any battery chemistry. In order to show this benefit, battery cells with different cell chemistry are investigated in this work. The three battery cells and one battery module under investigation are introduced in the following:

Cell A is a prismatic type, energy cell based on the lithium-polymer chemistry, which has a nominal voltage of 3.7 V. Cell B and C are cylindrical type, power cells based on the lithium-iron-phosphate cell chemistry and have a nominal voltage of 3.3 V. The capacity of Cell A is 40 A h, while Cell B and Cell C have a capacity of 4.4 A h and 1.1 A h, respectively. In Figure 3.3, similar battery cells commonly used in HEV are depicted exemplary and compared with a standard AA sized primary battery cell. The battery module is built by 192 series and 2 parallel connected cells (192S2P-configuration) of type Cell B, has a nominal voltage of 630 V and a maximal current of ± 200 A (c.f. Figure 3.2 (b)). Passive cell balancing is established between the battery cells, but balancing does not start until a 15 minute standby time of the battery. All battery cells and the battery module allow a temperature range for charge and discharge, respectively, between 0 °C and 40 °C, although the investigated and relevant temperature range in non-road application lies between 12.5 °C and 35 °C.

3.3   Training data for battery cell models

The methodology of optimal model based DoE, described in Section 2.3, provides excitation signals, which minimize the parameter variances of the identified battery models. In this work,

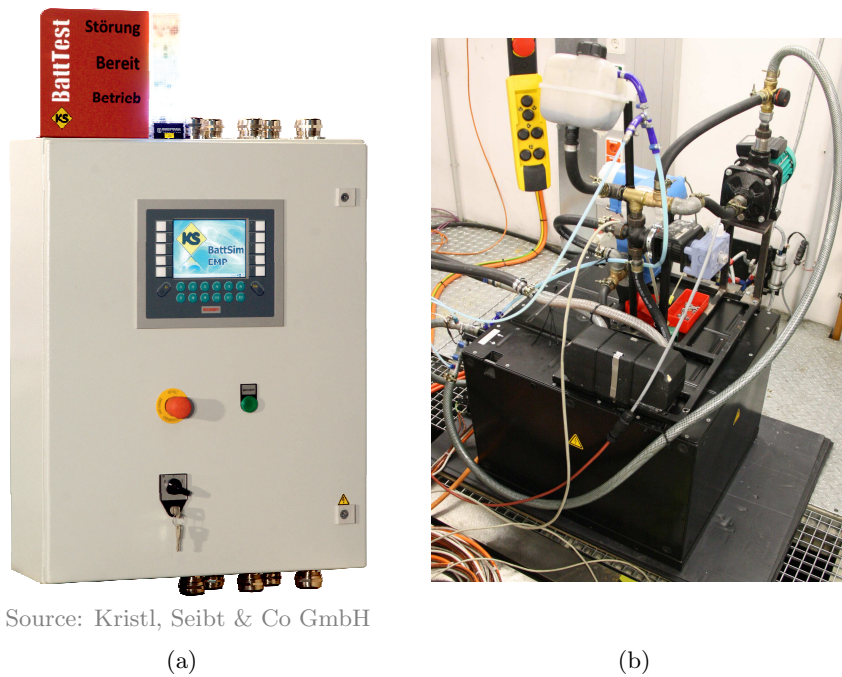Source: Kristl, Seibt & Co GmbH

(a) (b)

Figure 3.2: Battery simulator (KS BattSim) adapted for battery module testing (left) and real battery module (right).

Figure 3.3: Exemplary battery cells commonly used in HEV compared to a commercial AA-type battery cell.

these signals are used as training data and should be presented exemplary for battery cell $\boldsymbol{B}$ in the following. Figure 3.4 shows the result for the obtained optimal excitation signal with recorded voltage response of battery cell $\boldsymbol{B}$. The current signal and current constraints are depicted in Subplot two, where currents with more than $100\,\mathrm{A}$ can be observed. Cell $\boldsymbol{B}$ has a capacity of $4.4\,\mathrm{A\,h}$, which results in a C-rate of more than $22.5C$. Nevertheless, the corresponding voltage responses for the two depicted temperatures (see Subplot one) and the SoC (see Subplot three), keep the constraints. Note that even though the constraints of voltage and SoC are indirectly considered, any constraints are met and the entire relevant range of the SoC is covered.
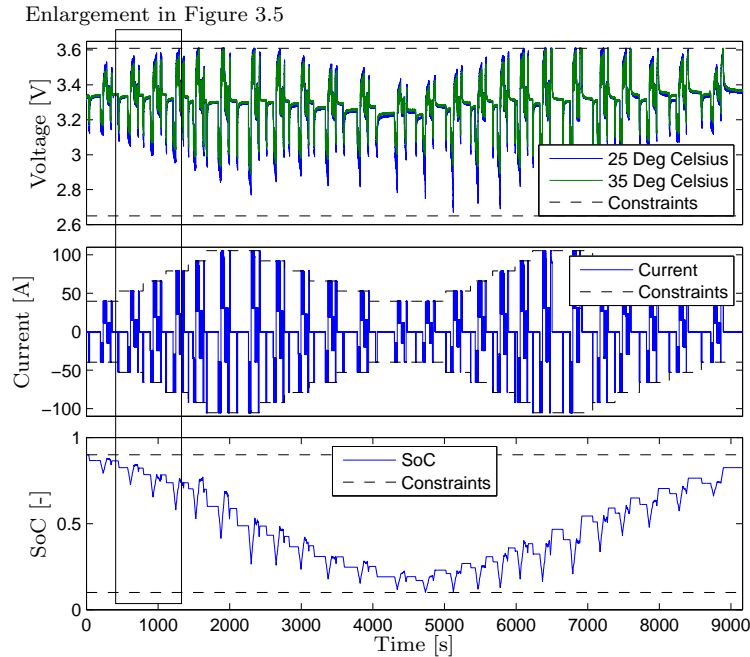

Figure 3.4: Optimal excitation signal obtained from optimal model based DoE for Cell $\boldsymbol{B}$ depicted for two temperatures.

In Figure 3.5, one extended excitation sequence is shown in more detail. Subplot two shows that the optimization considered the current constraints and the maximal current depending on the SoC, respectively. Furthermore can be seen that high dynamic current is obtained between the lower and upper current constraints (green and red lines), which is the optimized part of the optimal model based DoE methodology. Though, the voltage response depicted in Subplot one shows that the degree of freedom due to the linear reference model has not been fully exploited. Note that the spread of the current over the dynamic range may also include more intermediate steps, if a nonlinear reference model is used [149].

3.4   Validation of battery cell model accuracy

The results obtained with LMN battery models are presented in this section. First, the improvements due to optimal excitation signals are discussed based on two different LMN battery models. Second, the generic applicability to different cell chemistries and the influence of the mentioned nonlinearities are demonstrated. Last, the best LMN battery model is further discussed in terms of the dynamic accuracy.
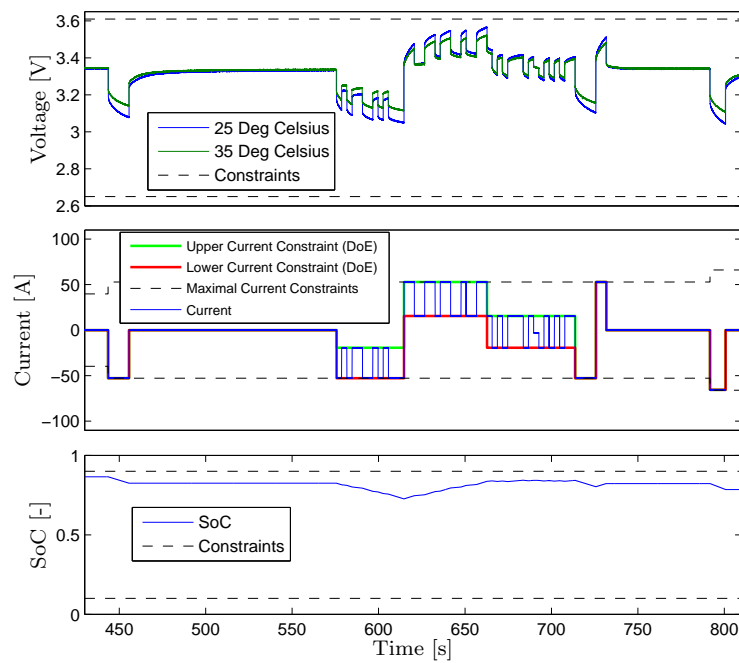
Figure 3.5: Enlarged view of the optimal excitation signal in Figure 3.4 for Cell **B** at two temperatures. In the second subplot, the current constraints for the optimization (green and red lines) as well as the maximal current constraint depending on the SoC (black dashed lines) are included.

3.4.1 Battery model quality improvement with optimal DoE

The accuracy of data-based LMN is significantly dependent on the used training data. For this reason, two local model networks (models Γ_1 and Γ_2) with the same configuration are identified by conventional DoE and optimal model based DoE, respectively, to show this dependency. The benefit can better be seen on a simplified LMN structure, which is chosen to $\mathcal{Z}_{12} = [z_{\text{SoC}} \ z_{\text{Hyst}}]$ as partition space and $\mathcal{Q}_{12} = [u_{\text{Current}}]$ as input space of the models. Since the ambient temperature is kept constant at $22.5\,^{\circ}\text{C}$, z_{Temp} is excluded in $\mathcal{Z}_{12}$ and z_{SoC}, u_{Relax} are neglected in $\mathcal{Q}_{12}$ in order to exclusively show the effect of the training data. Following the methodology in [69], a good compromise for the model order is found by analyzing the mean squared error of a linear model for different selections of the order and choosing a suitable model order between complexity and accuracy. The model orders of current and voltage are finally set by $m_{\text{Current}} = n_{\text{Voltage}} = 5$.

A LMN model with 10 local linear models is used to find a suitable choice for the kernel function sharpness of the SoC $k_{\sigma,\text{SoC}}$. The given configuration of the partition space leads to a good compromise by $k_{\sigma,\text{SoC},12} = 0.75$, which is obtained by comparing different selections of $k_{\sigma,\text{SoC}}$ with each other. Note that smoothness and strict partitioning is controlled by $k_{\sigma,\text{SoC}}$, since the overlapping of the validity functions is increased with a larger $k_{\sigma,\text{SoC}}$ value. A smooth separation between discharge and charge behavior of z_{Hyst} is not physically reasonable, due to which a desired sharp separation is obtained by $k_{\sigma,\text{Hyst}} = 0.05$. The threshold for the number of LLM is predefined by the critical real time limit of the battery emulator control unit (Beckhoff Industrial PC C6515), which is capable of $M = 30$ as is obtained by testruns[1]. Table 3.1 shows the summary of the LMN configuration parameters for models Γ_1 and Γ_2.

LMN Structure	Configuration Parameters
$\mathcal{Z}_{12} = [z_{\text{SoC}} \ z_{\text{Hyst}}]$ $\mathcal{Q}_{12} = [u_{\text{Current}}]$	$m_{\text{Current}} = n_{\text{Voltage}} = 5$ $k_{\sigma,\text{SoC},12} = 0.75$ $k_{\sigma,\text{Hyst}} = 0.05$ $M = 30$

Table 3.1: Summary of the LMN configuration parameters of models Γ_1 and Γ_2, which are used to compare the benefits of optimal model based DoE to conventional DoE. The model parameters are identified by different training data at $22.5\,^{\circ}\text{C}$ temperature (c.f. Figure 3.6 and 3.7).

In Figure 3.6, the raw training data for model Γ_1 is depicted, where conventional DoE for Cell $\boldsymbol{C}$ is used to obtain the excitation signal. Hu et al. [65] proposed a step profile training data, which is similar to the one used. Note that the conventional DoE is more dynamic than other excitation signals in the literature [149] and is therefore used for comparison with the proposed experiment design. However, the step profile is established by alternating intermediate current steps in charge and discharge direction and the variation of the step durations realizes to cover the entire SoC range. Disadvantageous is that the DoE is very strict in terms of voltage, since the voltage behavior is not considered. Expert knowledge needs to be used to limit the current in order to avoid voltage violations. Nevertheless, in the second subplot the applied current constraints can be seen, which ensure that current, voltage and SoC constraints are met, although full current capabilities of the battery cell are not exploited by the step profile. Subplot one includes the training result obtained for the battery model Γ_1.

Model Γ_2 is identified using an optimal excitation signal obtained with the methodology proposed in Section 2.3 and adapted for Cell $\boldsymbol{C}$. The optimal model based DoE is depicted in Figure 3.7, where in the first subplot the training result of battery model Γ_2 is included. Subplot

---

[1] CPU usage of the LMN with $M = 30$ lies between 8 and $12\,\%$, which exhausts the real time limits in the used battery emulator.
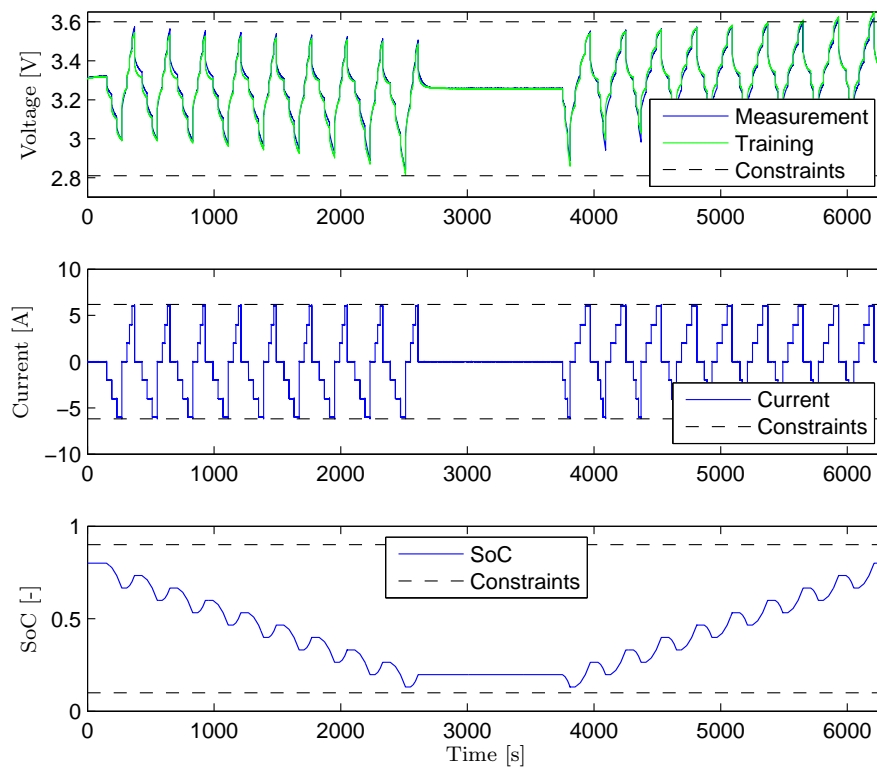
Figure 3.6: Step profile training data adapted for Cell C to be used for the parameter identification of model Γ_1. The temperature is hold at 22.5 °C. The training result of model Γ_1 is included in the first subplot.

two depicts the optimal excitation signal including the applied constraints, which indirectly consider the voltage and SoC limits, respectively. In comparison to the conventional DoE in Figure 3.6, the optimal excitation signal has superior dynamics and higher currents, while all constraints are met.
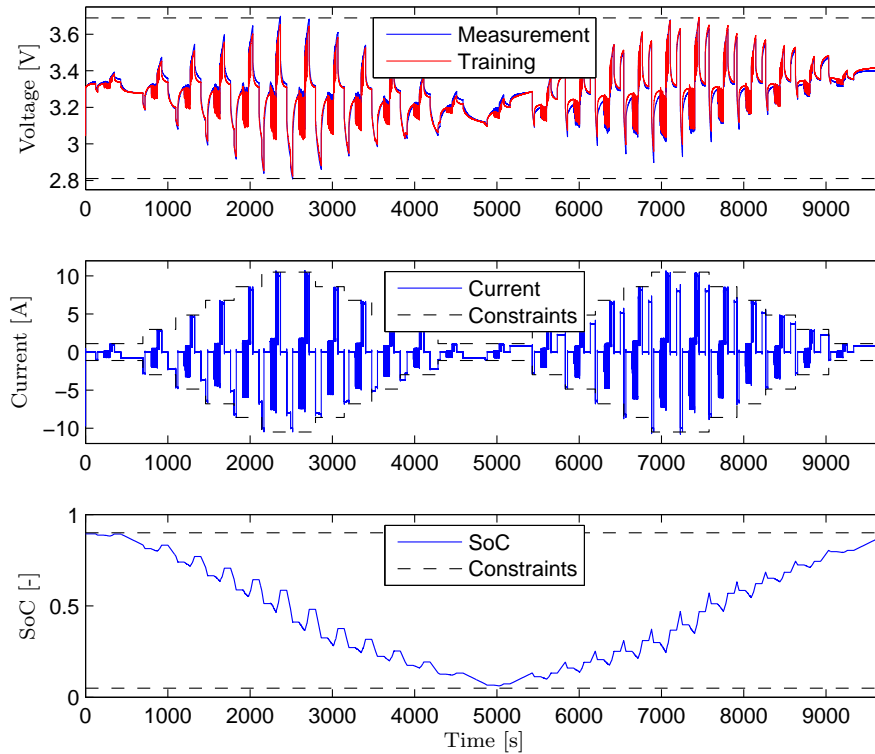

Figure 3.7: Optimal excitation signal training data for Cell C at 22.5 °C to be used for the parameter identification of model Γ_2. The training result of the model is included in subplot one.

In order to validate the obtained battery models Γ_1 and Γ_2 in terms of dynamics and high currents occurring in non-road applications, a repeated real (current-) load cycle is used, which does not change the SoC on average. Alternatingly raising/lowering the mean current value of the cycle, forces the SoC to pass the entire SoC range, due to which the signal is referred to as *SoC validation signal*. Note that in the following the maximal current capabilities of the battery cells under investigation are exhausted by scaling the cycle to the maximal current allowed for the specific cells. Figure 3.8 depicts the obtained simulation results for the models Γ_1 and Γ_2. In Subplot one, the voltage response of the battery and the simulated voltages of the models are shown. Subplot two and three show the current and the SoC trajectory, respectively. The ambient temperature during the experiment is kept constant at 22.5 °C.

Both models consider the nonlinear relationship between SoC and battery cell voltage, which is observable by comparing the envelope curves of the maximal voltage values in Subplot one of Figure 3.8. Nevertheless, a significant average error of model Γ_1 (56.25 mV) can be seen compared to the error of model Γ_2 (5.44 mV). The marked region in Figure 3.8 is depicted in detail in Figure 3.9.

In Figure 3.9, one cycle is enlarged to show the dynamic behavior of the models Γ_1 and Γ_2. In general, the behaviors are similar, but model Γ_1 shows a large offset compared to Γ_2, which
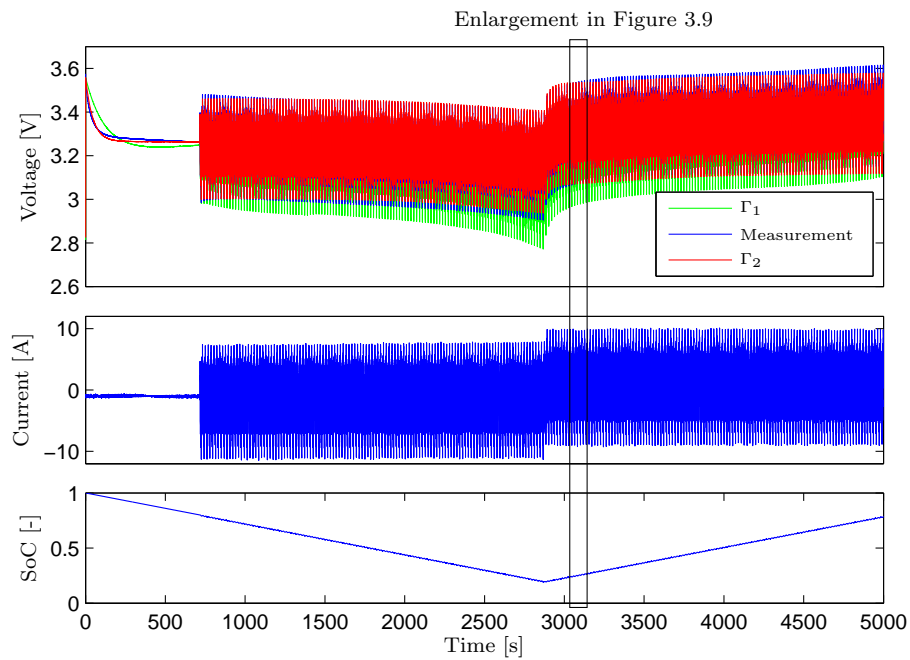
Figure 3.8: Simulation result comparison of models Γ_1 and Γ_2, shown on a SoC validation signal measured on Cell C at $22.5\,°C$. The signal is based on a real load cycle, which represents the high dynamic requirements of non-road applications. The envelope curves of the maximal voltage values show a significant higher error of model Γ_1.
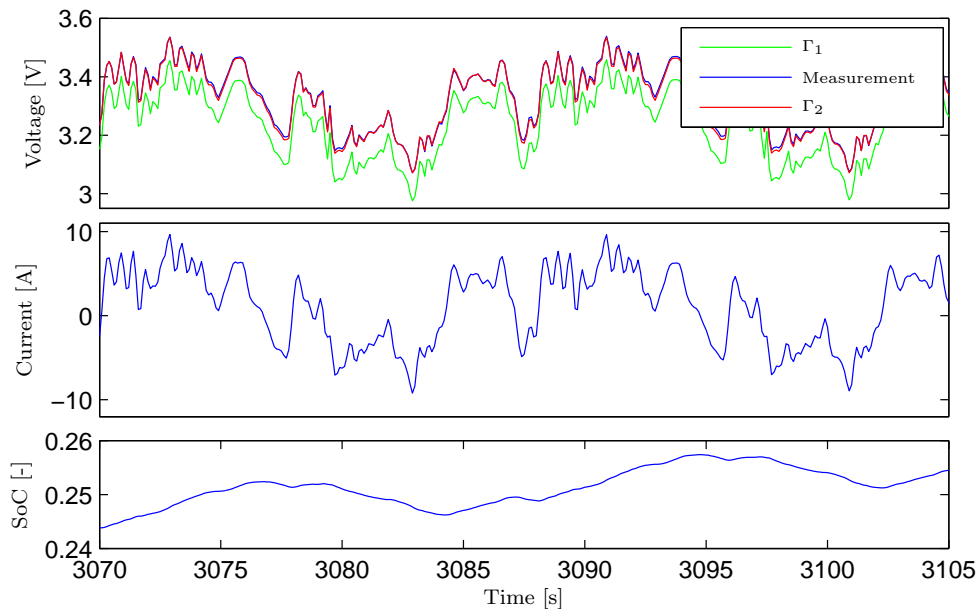

Figure 3.9: Enlarged view of Figure 3.8: The comparison of models Γ_1 and Γ_2 at one real load cycle measured on Cell C at $22.5\,°C$. Significantly accuracy increase due to high dynamic training data observable for model Γ_2.

is observable in the first subplot. One reason is the lack of high dynamic excitation in the step excitation signal used to train model Γ_1. Due to the optimal model based DoE, an optimal excitation signal is obtained, which is able to significantly increase the model accuracy at high dynamic excitation of the battery cells. Even though, C-rates above $9C$ occur in the validation signal, satisfactory model accuracy is obtained. For this reason, exclusively optimal excitation signals are used in the following to train the battery models.

3.4.2   Comparison of battery cell models with different LMN structures and cell chemistries

The influence of the optimal excitation signals on the LMN battery model quality is presented in the previous section. In the following, the influence of hysteresis, relaxation and temperature input on the LMN structure as well as the applicability of the LMN approach to different battery cell chemistries are discussed in detail. To this end, three different LMN battery model structures (Γ_3, Γ_4, Γ_5) are validated using two different validation signals (*temperature validation signal* and *SoC validation signal*) and two different cell chemistries (Cell $\boldsymbol{A}$ with lithium-polymer and Cell $\boldsymbol{B}$ with lithium-iron-phosphate chemistry). The achieved results are then compared with each other and interpreted.

Training data for the three models is obtained by creating optimal excitation signals for each cell chemistry separately and measuring the voltage response at 10 different temperatures between $12.5\,°\text{C}$ and $35\,°\text{C}$ in $2.5\,°\text{C}$ steps. Figure 3.4 shows the optimal excitation signal of Cell $\boldsymbol{B}$ at two different temperatures exemplarily for all cell chemistries, which are then merged to one training data set (raw data for identification) for Cell $\boldsymbol{A}$ and $\boldsymbol{B}$, similarly.

LMN Structure for Γ_3, Γ_4 and Γ_5	
Γ_3:	$\mathcal{Z}_3 = [z_\text{SoC}\ z_\text{Current}\ z_\text{Temp}]$, $\mathcal{Q}_3 = [z_\text{SoC}\ u_\text{Current}]$
Γ_4:	$\mathcal{Z}_4 = [z_\text{SoC}\ z_\text{Hyst}\ z_\text{Temp}]$, $\mathcal{Q}_4 = [z_\text{SoC}\ u_\text{Current}]$
Γ_5:	$\mathcal{Z}_5 = [z_\text{SoC}\ z_\text{Hyst}\ z_\text{Temp}]$, $\mathcal{Q}_5 = [z_\text{SoC}\ u_\text{Current}\ u_\text{Relax}]$
Configuration Parameters for Γ_3, Γ_4 and Γ_5	
$m_\text{SoC} = 1$ $k_{\sigma,\text{SoC},345} = k_{\sigma,\text{Temp}} = 0.6$	
$m_\text{Relax} = 3$ $k_{\sigma,\text{Hyst}} = k_{\sigma,\text{Current}} = 0.05$	
$m_\text{Current} = n_\text{Voltage} = 5$ $M = 30$	

Table 3.2: Summary of the LMN configuration parameters of models Γ_3, Γ_4 and Γ_5. The influence of the hysteresis as well as relaxation input on the model accuracy is illustrated by different $\mathcal{Z}$ and $\mathcal{Q}$. The model parameters are identified by the same training data (c.f. Figure 3.4).

In Table 3.2, the LMN structures and configuration parameters of the models explained in the following are summarized. The purpose of the simplest model (Γ_3) is to provide a reference to show the influence of hysteresis and relaxation input to the model structure, which are not considered in Γ_3. However, the temperature is considered in the partition space, which follows by $\mathcal{Z}_3 = [z_\text{SoC}\ z_\text{Current}\ z_\text{Temp}]$ and the input space, including the SoC as mentioned in Section 2.2.3, is defined by $\mathcal{Q}_3 = [z_\text{SoC}\ u_\text{Current}]$. Note that due to the excluded hysteresis input, the corresponding polarization of the battery cell is not indicated through the current z_Current at standby, since z_Current is only interpolated between charge/discharge behavior. The current is therefore initially partitioned between positive/negative current instead of charge/discharge mode, but nevertheless the current effects are considered in model Γ_3.

Model Γ_4 is improved compared to model Γ_3 by replacing the current input with the hysteresis input, which leads to a partition space $\mathcal{Z}_4 = [z_\text{SoC}\ z_\text{Hyst}\ z_\text{Temp}]$ and an input space $\mathcal{Q}_4 = \mathcal{Q}_3$.

At this point it is important to mention that the complexity of the model is unchanged in this case. An increase in model complexity is obtained in model Γ_5, which includes the relaxation input in the input space. Hence the input space can be denoted by $\mathcal{Q}_5 = [z_{\mathrm{SoC}} \ u_{\mathrm{Current}} \ u_{\mathrm{Relax}}]$ and the partition space remain the same ($\mathcal{Z}_4 = \mathcal{Z}_5$). Note here, that any in this work mentioned nonlinear and/or electrochemical effects are considered in model Γ_5.

In terms of the configuration parameters, the objectives remain the same as for the models Γ_1 and Γ_2 and can therefore directly taken from Table 3.1. Therefore, the parameters for models Γ_3, Γ_4 and Γ_5 follow to $m_{\mathrm{Current}} = n_{\mathrm{Voltage}} = 5$, $k_{\sigma,\mathrm{Hyst}} = 0.05$ and $M = 30$, while $k_{\sigma,\mathrm{Current}} = k_{\sigma,\mathrm{Hyst}} = 0.05$ is set for the sharpness factor of the current input to achieve a sharp separation between charge and discharge behavior. In case of the optimal kernel function sharpness of the SoC and temperature, $k_{\sigma,\mathrm{SoC},345} = k_{\sigma,\mathrm{Temp}} = 0.6$ slightly increases the smoothness of the validity function and is therefore chosen for the temperature input. The SoC input has no dynamic influence on the system behavior, for which reason the order of the input is set straight forward to $m_{\mathrm{SoC}} = 1$. Because $filt(\cdot)$ of the relaxation input is established using a third order low pass filter, the order within the LMN model is also set straight forward to $m_{\mathrm{Relax}} = 3$.

The validation of the battery models is achieved using the two mentioned validation signals for temperature and SoC, while the *SoC validation signal* is already introduced beforehand and slightly improved. Aim of the temperature validation is to show the model accuracy in case of temperature changes and different SoC values. Due to this reason, the ambient temperature is heated up to the upper level of $32\,^\circ\mathrm{C}$ and cooled back to the lower level of $18\,^\circ\mathrm{C}$, while the aforementioned real load cycle is continuously applied to the battery cell. This procedure is repeated for different SoC levels and is referred to as *temperature validation signal*.

The *SoC validation signal*, as introduced earlier in this section, is furthermore improved to strengthen the significance of the validation by alternatingly raising/lowering the current mean value in between the repetitions of the cycle. Due to the more often changed average charge direction, the dynamic behavior is more excited and proves the battery model therefore with more significance. Though, the entire SoC range is covered. In the next subsection, the *temperature validation signal* and *SoC validation signal* are described in terms of the dynamic behavior and depicted in Figures 3.10 and 3.12, respectively.

Based on the mean squared error and a normalized root mean squared error (NRMSE) as given in eq. (3.1), the model accuracy can be evaluated. The NRMSE can be denoted by

$$e_{NRMSE,\%} = \sqrt{\frac{1}{N_s} \sum_{i=1}^{N_s} \left(\frac{y_i - \hat{y}_i}{\max(y) - \min(y)} \right)^2} \cdot 100\%, \tag{3.1}$$

where N_s is the number of samples, y is the measured output and $\hat{y}$ is the simulated output. Note that the different cell chemistries have different nominal voltages, due to which a normalization of the measured output values in eq. (3.1) is required in order to allow a direct comparison between the different battery model accuracies. Table 3.3 presents the MSE and NRMS values for the different LMN architectures and cell chemistries.

In Table 3.3, a continuous decrease in the error values is observable from model Γ_3 to model Γ_5. Reasons are the included hysteresis input (Γ_4) and the increased complexity (Γ_5) similar for both cell chemistries. The interpolation between the charge/discharge behavior at standby current in model Γ_3 is not physically appropriate, while in contrast, the corresponding polarization is indicated through the hysteresis input in model Γ_4 and Γ_5. In terms of the electrochemical behavior of battery cells, models Γ_4 and Γ_5 are more physically appropriate and therefore the model accuracies are improved.

The time constants of electrochemical batteries are usually very different, due to which a high sampling rate is required for the measurements since otherwise the fast dynamic behavior is not considered in the recorded data. A fast sampling rate causes a highly correlated data set

Battery Cell:		Cell A		Cell B	
Criterion:		MSE	NRMSE	MSE	NRMSE
Temp. Val. Sig.	Γ_3	$2.935\mathrm{e}^{-4}$	$2.059\,\%$	$7.592\mathrm{e}^{-4}$	$2.671\,\%$
	Γ_4	$2.668\mathrm{e}^{-4}$	$1.963\,\%$	$6.585\mathrm{e}^{-4}$	$2.487\,\%$
	Γ_5	$2.447\mathrm{e}^{-4}$	$1.752\,\%$	$5.236\mathrm{e}^{-4}$	$2.218\,\%$
SoC Val. Sig. 20 °C	Γ_3	$3.711\mathrm{e}^{-4}$	$2.537\,\%$	$5.652\mathrm{e}^{-4}$	$2.933\,\%$
	Γ_4	$3.559\mathrm{e}^{-4}$	$2.485\,\%$	$4.811\mathrm{e}^{-4}$	$2.706\,\%$
	Γ_5	$1.431\mathrm{e}^{-4}$	$1.438\,\%$	$3.386\mathrm{e}^{-4}$	$2.270\,\%$
SoC Val. Sig. 25 °C	Γ_3	-	-	$4.622\mathrm{e}^{-4}$	$2.928\,\%$
	Γ_4	-	-	$4.094\mathrm{e}^{-4}$	$2.756\,\%$
	Γ_5	-	-	$3.109\mathrm{e}^{-4}$	$2.402\,\%$
SoC Val. Sig. 30 °C	Γ_3	-	-	$3.633\mathrm{e}^{-4}$	$2.847\,\%$
	Γ_4	-	-	$3.393\mathrm{e}^{-4}$	$2.752\,\%$
	Γ_5	-	-	$2.496\mathrm{e}^{-4}$	$2.360\,\%$

Table 3.3: Validation error values for the LMN battery models Γ_3, Γ_4 and Γ_5 as defined in Table 3.2. The error values are shown for Cell A and B, respectively. Comparing the models with each other, independent from the cell chemistry, model Γ_5 has the best model accuracy, model Γ_3 the worst and model Γ_4 denotes intermediate accuracy.

though and leads to numerical problems due to ill-conditioning at the parameter estimation [12], [94]. This phenomenon is referred to as redundance [12]. The used sample time of 100 Hz makes a precisely identification of the corresponding relaxation time constant within the dynamic behavior very difficult. Therefore, the relaxation input of model Γ_5 is used to provide the required information of the slow relaxation time constant. As is observable in the results, this improves the accuracy significantly.

Based on Table 3.3 and the corresponding MSE/NRMSE values, the best model accuracy of the three discussed models (Γ_3, Γ_4, Γ_5) is achieved by model Γ_5, which is discussed in detail in the following.

3.4.3   Dynamic accuracy of the LMN battery models

Previously only the error values are used to evaluate the battery model accuracy. In the following, the dynamic accuracy achieved with the introduced battery model Γ_5, which considers all relevant electrochemical effects, is discussed in detail in terms of relaxation, hysteresis and temperature influence. The dynamic behavior of the measured cell chemistries are all similar, due to which the resulting plots are depicted for Cell B only. Figure 3.10 shows the temperature validation signal, where SoC and temperature trajectory are depicted in Subplot three and four, respectively.

The measured voltage response and the simulated cell voltage using model Γ_5 can be seen in Subplot one in Figure 3.10. Clearly observable is the dependence of the model output on the ambient temperature. A changing time constant of the relaxation effect, which is not considered in the constant time constant of the filter input, causes a model mismatch at the beginning of the dynamic excitation at the different SoC levels. Nevertheless, following Table 3.3, the model accuracy is increased significantly due to the relaxation input. Since high battery currents (more than $20C$) occur in non-road applications, the training data is focused to high dynamically excite the battery behavior, which leads to a lack of sufficient information at low constant current (below $2C$). This is observable at the small model mismatch during transition to the different SoC levels using low constant currents. Note that the continuous change between charge and discharge prevents to observe the hysteresis effect directly in Figure 3.10. Influence and benefit due to the hysteresis input are verified explicitly by the error values in Table 3.3 though. Figure 3.11 shows an enlarged view of the marked region (Enlargement (a)) in Figure 3.10.

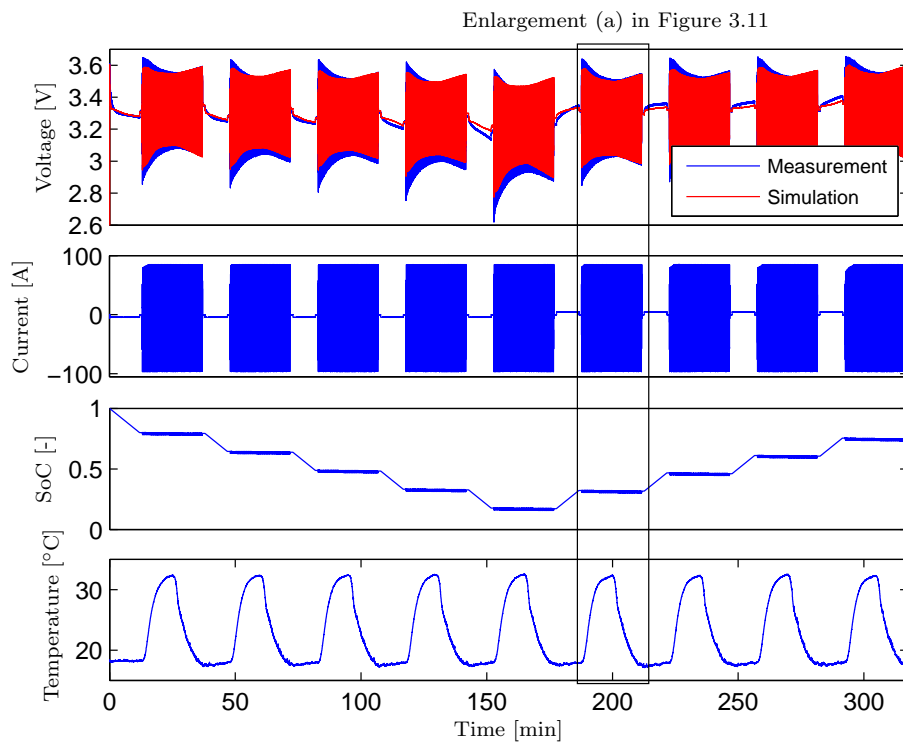In Figure 3.11 one load cycle is shown in an enlarged view. Enlargement (a) depicts the volt-

Figure 3.10: Resulting plot of the temperature validation signal applied to Cell **B** and the simulated cell voltage using model Γ_5. The real load cycle is repeated at different SoC levels while the ambient temperature is heated up to the upper level of $32\,°C$ and cooled back to the lower level of $18\,°C$.
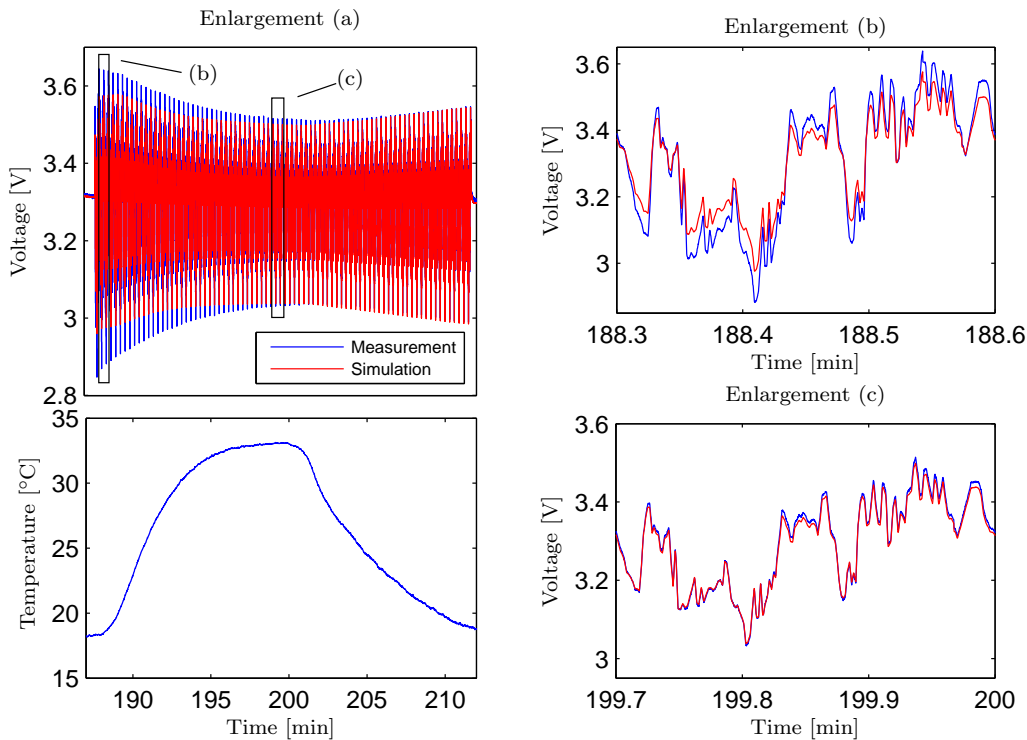
Figure 3.11: Resulting enlargement plots of the temperature validation signal (see Figure 3.10) applied to Cell **B**. Enlargements (b) and (c) as defined in (a).

age and temperature signal, while enlargement (b) and (c) show the corresponding enlargement of the marked regions in enlargement (a). The model dynamics, as can be seen, are sufficient for non-road applications. A comparison between enlargement (b) and (c) shows the slightly bigger voltage error in enlargement (b) due to the mentioned changing time constant of the relaxation effect.

Figure 3.12 presents the resulting SoC validation signal at $20\,°C$, $25\,°C$ and $30\,°C$ constant ambient temperature, where the temperature influence on the voltage behavior is clearly observable.

Subplot four in Figure 3.12 shows the invariant model error for the different temperatures, which never exceed a maximum error of $90\,mV$ and stay within a small tolerance tube. Hence, it can be concluded that the SoC and temperature are considered in the battery model since the error does not depend on the changing SoC or temperature. In Figure 3.13 the marked region in Figure 3.12 is depicted in detail, where one real load cycle with current rates above $20C$ at $30\,°C$ ambient temperature can be seen.

The nonlinear behavior at low SoC is especially distinctive. In Figure 3.13 it can be seen that although the SoC is low and high current values (above $20C$) occur, the LMN battery model represents the underlying strong nonlinear behavior of the battery cell accurately.

3.5   Battery cell temperature model accuracy

In order to simulate the battery model without measured signals, the temperature is required as model input. The simple temperature model proposed in Section 2.4 is able to provide sufficient accuracy for the simulation of the cell temperature. Based on the same training data used for the battery cell identification, the cell thermal capacity and heat transfer coefficient can
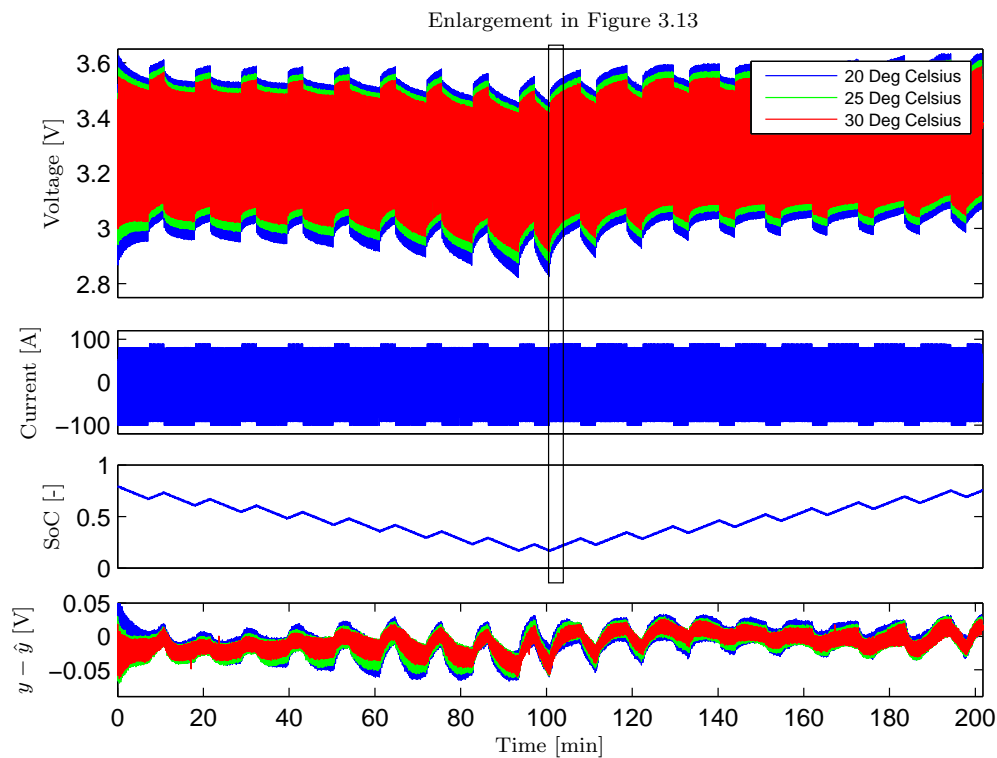
Figure 3.12: Resulting plot of the SoC validation signal applied to Cell $\boldsymbol{B}$ at three different ambient temperatures (20 °C, 25 °C and 30 °C). An enlarged view of the marked region is depicted in Figure 3.13.

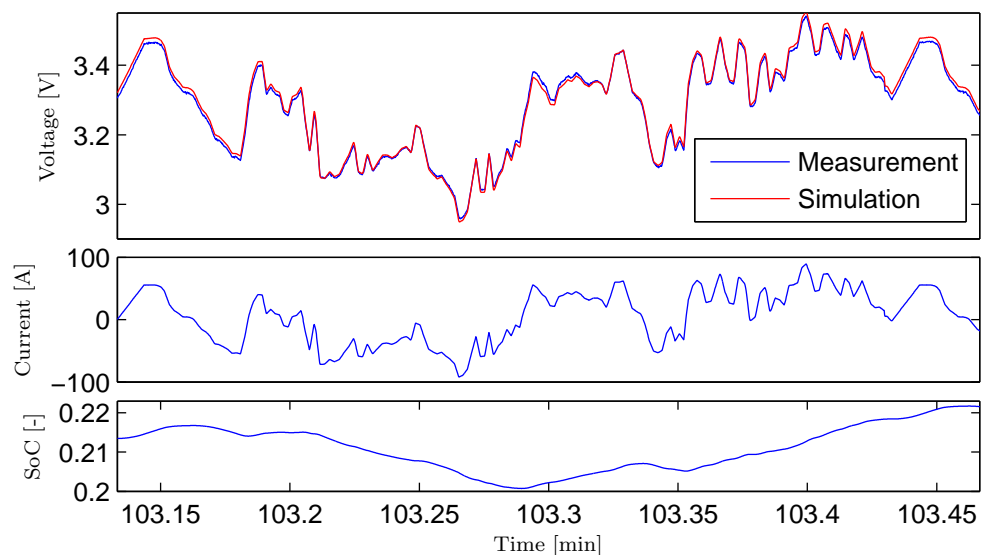Figure 3.13: Enlarged view of marked region in Figure 3.12. One real load cycle applied to Cell $\boldsymbol{B}$ at 30 °C ambient temperature. Simulation result of battery model Γ_5 at applied current rates above 20C.

be identified. For Cell $\boldsymbol{B}$, the temperature model parameters are obtained to $c_p = 833.34\frac{Ws}{K}$ and $h_{out} = 3.686\frac{W}{K}$, respectively, which leads to the temperature model accuracy shown in Figure 3.14. The first row of subplots shows the measured and simulated cell temperature, respectively, for the optimal excitation signal, the SoC validation signal and the temperature validation signal. In the second row of subplots, the corresponding errors are depicted, while in the third row, the ambient temperature is shown. As can be seen is that the model quality is accurate, while only the transient temperature changes of the temperature validation signal shows higher errors. This is caused by the external mounted temperature sensor, which is in case of the temperature validation signal more influenced by the strong gradient of the ambient temperature. Nevertheless, these ambient temperature gradients usually do not appear in real non-road vehicles, due to which the temperature model is legitimized. Note that the two error peaks in the SoC validation signal result from the merging of the validation signals and is observable at the non realistic steps in the ambient temperature signal.
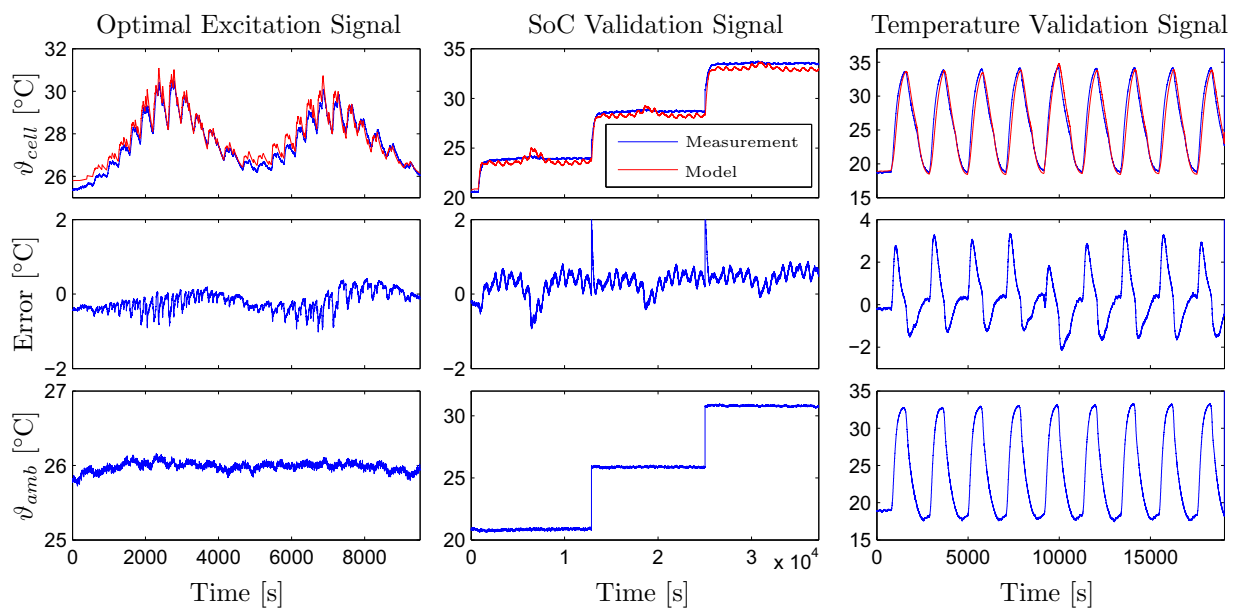

Figure 3.14: Result obtained for the temperature model of Cell $\boldsymbol{B}$.

3.6   Battery module model accuracy

The used battery module is built with $n_{cells} = 192$ series and $p_{cells} = 2$ parallel connected cells of type Cell $\boldsymbol{B}$. Hence the obtained LMN battery cell model Γ_5 (cf. Table 3.2) can be used for the simulation of the battery module behavior, which is discussed in the following. Note that the balancing is activated after 15 minutes in standby mode and thus has no influence in the following.

Due to the limited time capacities at the test bed, only step profiles at three different current levels are measured to create a set of training data for the battery module parameter identification. Nevertheless, the training results showed that the step profile with the full current coverage is sufficient. In Figure 3.15 the used step profile is depicted.

In the first subplot of Figure 3.15, the voltage behavior as well as the training results for the four proposed module models are depicted. The corresponding current and SoC signals are shown in the second and third subplot, respectively. In the last subplot, the absolute value of the voltage difference between measurement and model (error) is shown. It can be observed
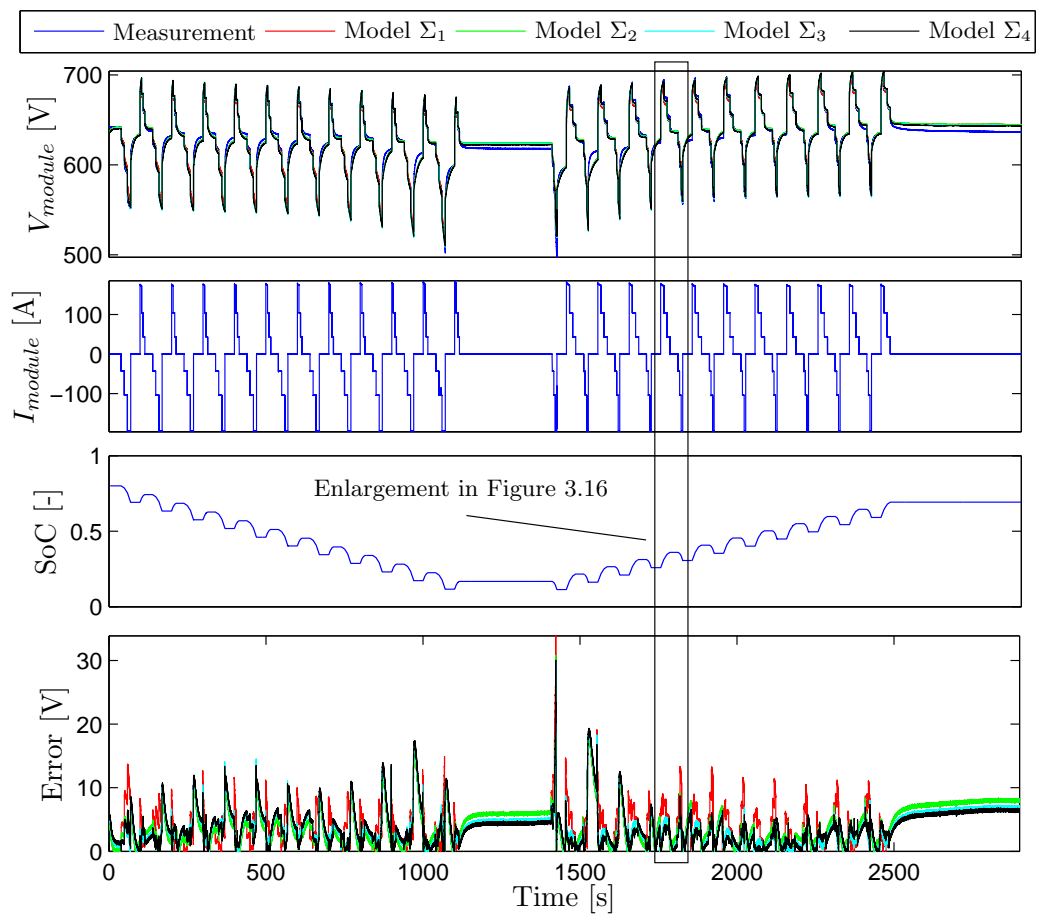
Figure 3.15: Training data for battery module models

that the error values are very small for all model approaches. An enlarged view of the training data is depicted in Figure 3.16.
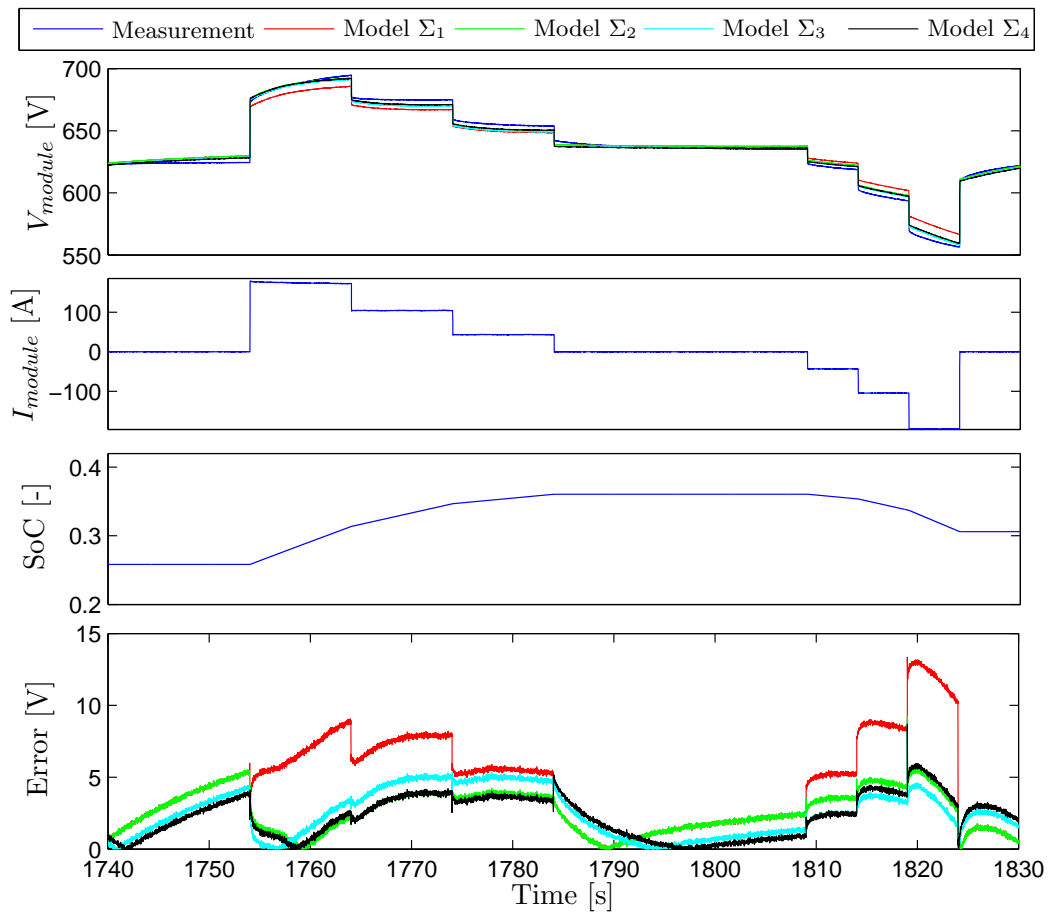

Figure 3.16: Enlarged view of the marked region in Figure 3.15.

The error of the battery models is again depicted in the last subplot of Figure 3.16. Clearly observable is the significantly higher error of the simple model Σ_1, which does not consider the internal resistance of the battery model. The other models are similar to each other, which indicates that the internal resistance is the major influencing effect beside the electrochemical effects considered by the LMN battery cell model. In order to validate the battery module models, a SoC validation signal is generated that is based on the scaled real load cycle as introduced for the battery cell validation. The repeated real load cycles are superposed with zero, negative and positive constant currents, respectively, to obtain the system behavior across the entire SoC range. Figure 3.17 depicts the SoC validation signal used for the battery module.

Subplot one of Figure 3.17 shows the measured as well as simulated voltages. The second subplot shows the current signal, where can be seen that the full current range is exploited. In subplot three, the SoC profile is shown, which passes the entire range of SoC used in non-road vehicles. The last subplot shows the model errors, where the difference between model Σ_1 and the other models Σ_2, Σ_3 and Σ_4 is clearly observable. Note that the reason for the peak errors at the transitions, results from data set merging, since a continuous measurement of the entire SoC validation signal is not supported by the battery tester. Nevertheless, Figure 3.18 shows an enlarged view of the validation signal.
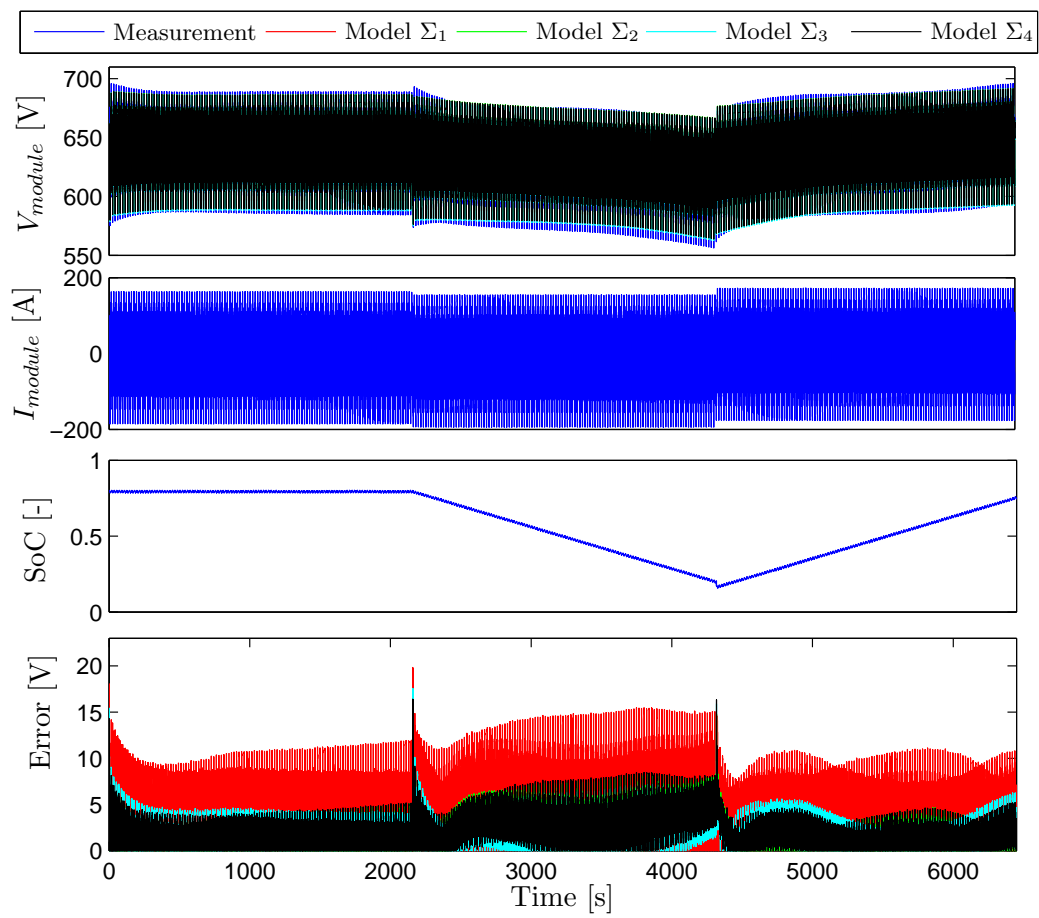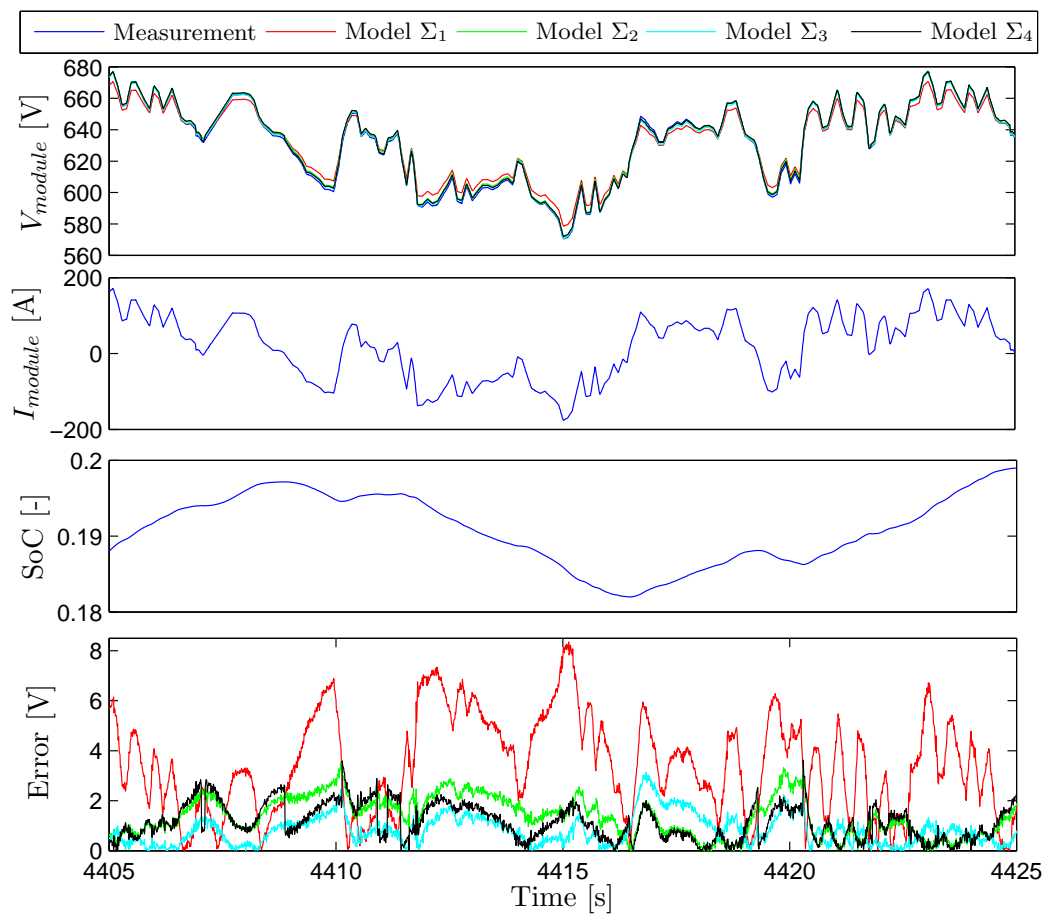
Figure 3.17: Validation data for battery module models.

Figure 3.18: Enlargement of Figure 3.17: Validation data for battery module models.

As can be seen in Figure 3.18, all models are able to depict the high dynamic behavior of the battery module, while only model Σ_1 has a slightly larger mismatch. Although a current of almost $\pm 200\,\text{A}$ is applied to the battery module, the accuracy is superior. Nevertheless, model Σ_4 has a slightly better overall accuracy compared to the other models. This is also observable in the MSE and NRMSE (cf. eq. (3.1)) values obtained for the SoC validation signal as shown in Table 3.4.

Criterion:	MSE	NRMSE
Model Σ_1	27.8851	2.5962 %
Model Σ_2	7.5727	1.3529 %
Model Σ_3	6.9949	1.3003 %
Model Σ_4	6.5871	1.2618 %

Table 3.4: Battery module SoC validation signal error values for the LMN battery module models Σ_1, Σ_2, Σ_3 and Σ_4.

Table 3.4 shows the slightly increase in accuracy due to the considered voltage offset and current dependent parameters, respectively. Nevertheless, a NRMSE clearly below $2\,\%$ is worth mentioning.

3.7 SoC estimation accuracy

The SoC estimation is essential in non-road vehicles, since the occurring high power densities cause measurement inaccuracies of the on-board sensors. Thus large SoC mismatches during operation are observable in case of a current accumulated SoC. Several initializations during operation are required to increase the accuracy, but mostly non-road vehicles are operated without breaks due to which a SoC reset based on standby conditions is not possible. For the SoC validation signal of the available real battery module, in Figure 3.19, the comparison between the current accumulated SoC and the implemented BMS SoC is depicted. At this point it is important to mention that a high accurate current sensor implemented in the battery tester is used to measure the current signal, which admits the comparison.

The first, second and third subplot in Figure 3.19, show the voltage, current and SoC signal, respectively. In the last subplot, the difference between the current accumulated SoC and the BMS provided SoC is depicted, where a significant mismatch is observable clearly. Note that the SoC validation signal is not measured in one test run, due to which the observable SoC drift of the real BMS is cleared after the cycles without superimposed constant current. Based on this information, the assumption of inaccurate SoC estimation of the BMS is shown to be true.

In the following, the results achieved with the LMN based SoC estimation for the battery module are presented. Since cell monitoring is important in terms of safety issues of battery modules, the SoC estimation methodology is also applicable to battery cells. To this end, SoC estimation results obtained for the battery cells are presented additionally. Nevertheless, an overall SoC estimation is desired, for which the module SoC estimation is of main interest.

3.7.1 Battery module SoC estimation results

The battery module model Σ_4 is used in the fuzzy observer to estimate the SoC of the battery module. As discussed in Section 2.6.2, estimation accuracy of the Kalman filters can be tuned by choosing the corresponding process $\boldsymbol{Q} = \boldsymbol{1} \cdot Q$ and measurement $\boldsymbol{R} = \boldsymbol{1} \cdot R$ noise variance matrices, where $\boldsymbol{1} \in \mathbb{R}^{n \times n}$ indicates a one matrix with corresponding dimension n. For the given battery module, a measurement noise variance is chosen to $R = 25000$, while the process
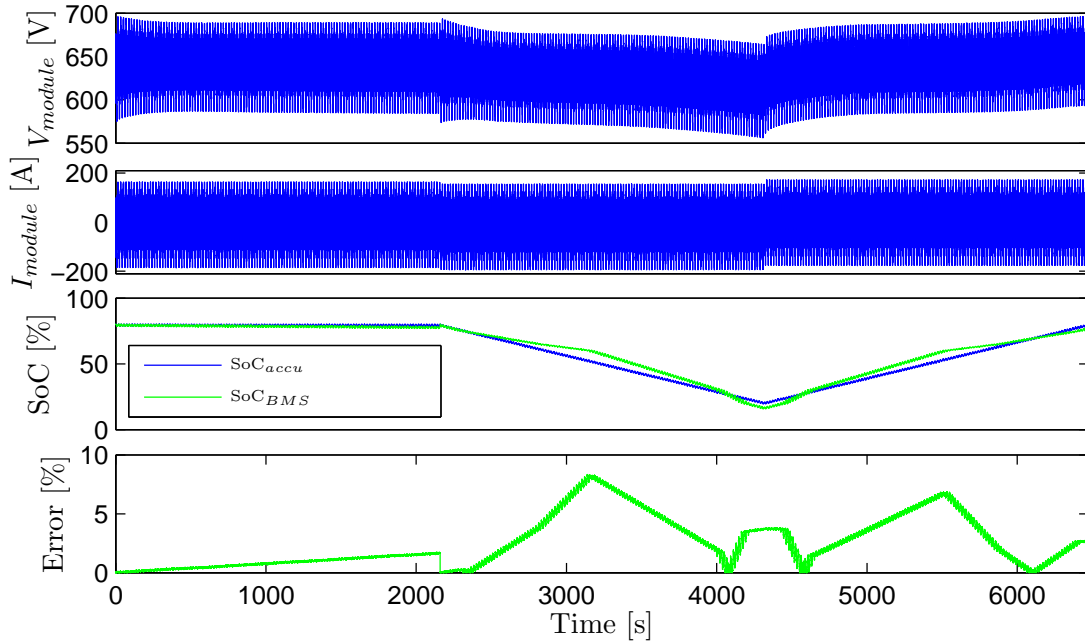
Figure 3.19: SoC estimation accuracy shown on a SoC validation signal measured at a real battery module.

noise variance is chosen between $Q = 0.01$ and $Q = 1$ to show the influence. In Figure 3.20 the results are depicted.

The upper subplot in Figure 3.20 shows the estimated SoC, while in the lower subplot, the difference to the current accumulated SoC is depicted. It can be seen that the accuracy increase with smaller process noise, which in other terms can be interpreted as larger weighting of the current accumulation within the augmented observer model. The disadvantage of a small Q is though that the convergence in case of a wrong initial SoC is significantly slower. Since usually a correctly approximated initial SoC value is obtained after standby, the OCV based SoC estimation is accurate enough to initialize the fuzzy observer and the process noise can be chosen small. Nevertheless, the convergence speed of the filter is also important and the performance of the observer in terms of convergence should be discussed in the following. To this end, unrealistic initial SoC values are used to test the convergence speed of the filter with different process noise variances. In Figure 3.21, the results for initial SoC at $SoC_{init} = 0\,\%$ and $SoC_{init} = 200\,\%$ are depicted. Note that $SoC_{init} = 200\,\%$ is not feasible in general, but shows that the filter converges from any initial SoC.

As can be seen in the second subplot, the larger choice of the process noise variance has a positive influence on the convergence speed, but the accuracy at converged state is poor. Therefore, a trade off between a fast convergence and SoC estimation accuracy needs to be made and the best application specific alternative must be chosen. In comparison to the SoC value obtained through the BMS of the module, the differences are low due to the precise LMN based battery model. Nevertheless, small process noise leads to unsufficient performance, since the actual SoC of the module can not be reached, if the initial SoC is to far from the actual value.

3.7.2 Battery cell SoC estimation results

Since monitoring purposes of the BMS are also important, in the following, the SoC estimation applied to battery cells is reviewed shortly. The BMS requires to monitor the single cell voltages
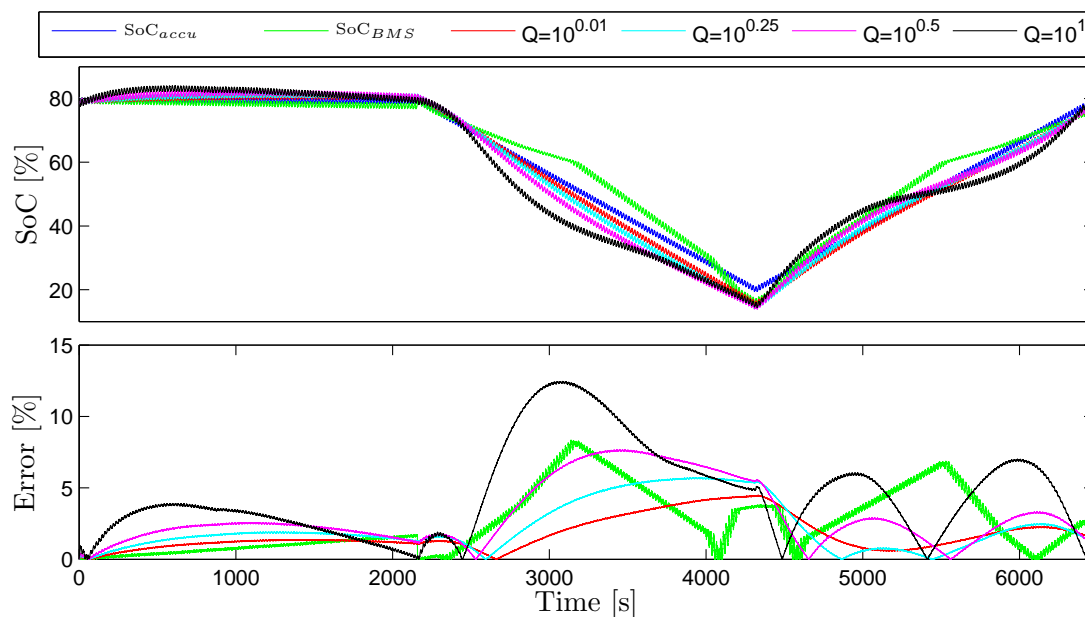
Figure 3.20: Accuracy of LMN based SoC estimation on real battery module.
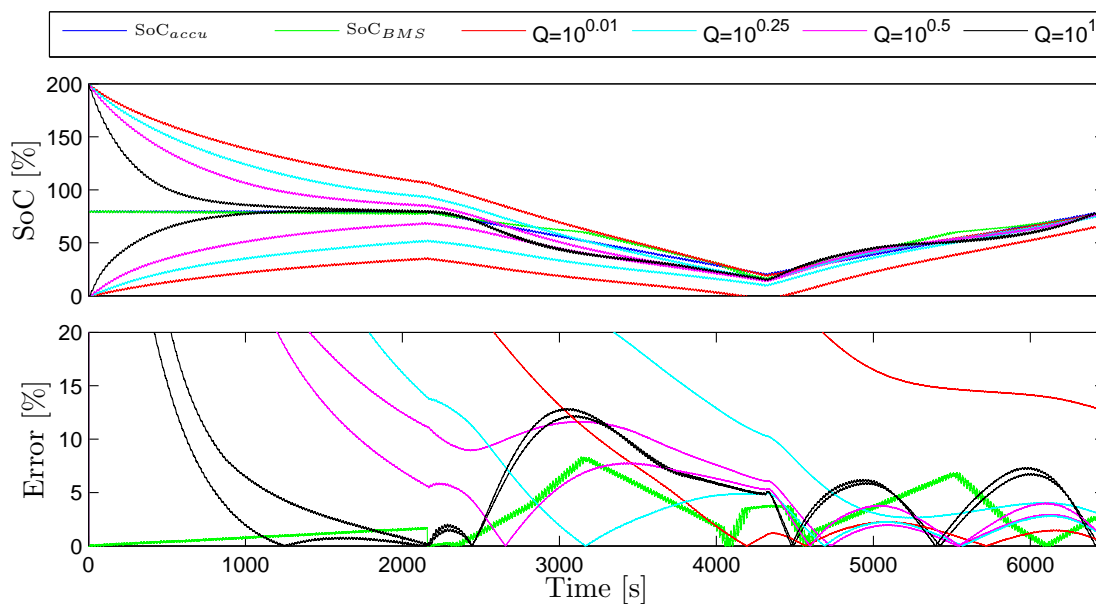

Figure 3.21: Convergence of LMN based SoC estimation on real battery module.

and conditions, which provides the possibility to estimate the cell SoC beside of the module SoC simultaneously. Note that the estimation of the cell SoC is more difficult than the module SoC, since an already very small voltage difference indicate a large SoC difference. This is caused by the flat discharge voltage behavior as discussed in Section 2.2.3 and Figure 2.5. Nevertheless, similarly to the battery module, the filter parameters can be chosen correspondingly to the desired filter properties.

Based on the merged SoC validation signals measured at different temperatures, the SoC estimation of battery cells should be presented. In Figure 3.22, the validation data is depicted. The merging of the individual data sets can be observed clearly in the temperature and SoC
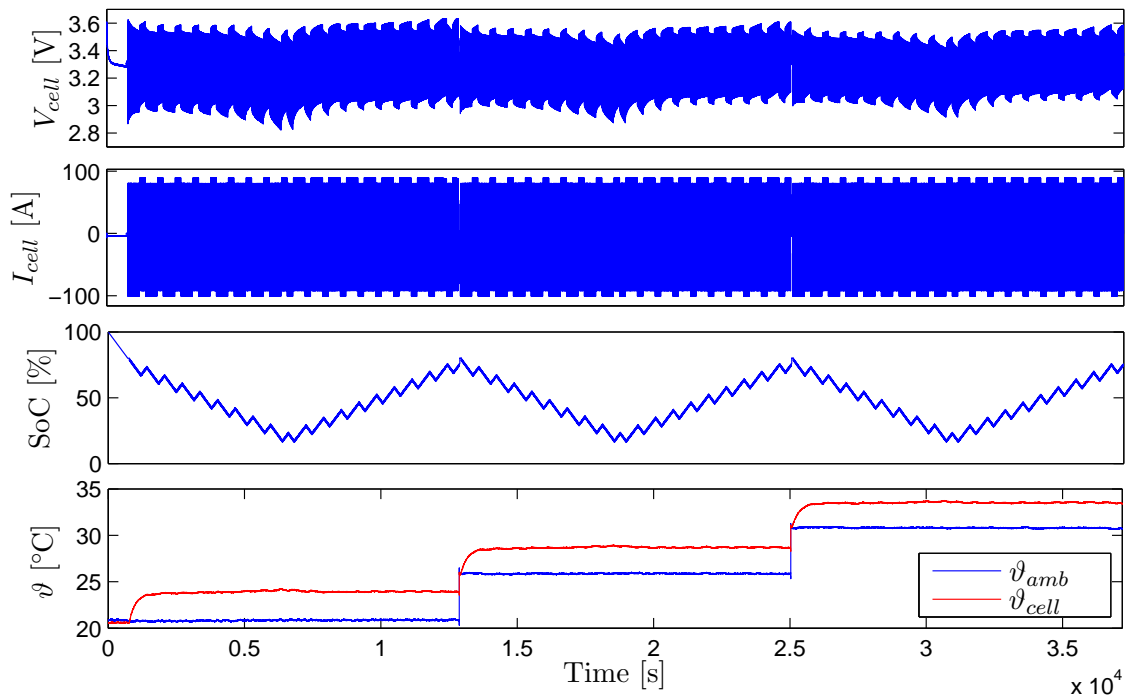

Figure 3.22: SoC estimation accuracy shown on the SoC validation signal at different temperatures measured on battery Cell **B**.

signal, respectively, where steps in the ambient temperature and SoC due to a SoC reset occur. In Figure 3.23, the battery cell SoC estimation results for the initial SoC values $SoC_{init} = 0\,\%$, $SoC_{init} = SoC$ and $SoC_{init} = 200\,\%$ are depicted, which are obtained for a chosen measurement noise variance of $R = 1 \cdot 25000$ and a set process noise variance of $Q = 1 \cdot 10^{0.01}$.

The convergence of the filter is observable clearly in Figure 3.23, where at the end of the signal, all SoC signals are almost identical. Although the initial condition of $SoC_{init} = 200\,\%$ is physically impossible, the filter is able to converge to the correct SoC. As can be seen in Subplot two of Figure 3.23, the accuracy for the first SoC validation signal is better in comparison to the others, although a SoC estimation error for the discharge part of the signal is observable. This is caused by the model mismatch, although the accuracy of the LMN battery cell model is high. For the higher temperature validation signals, the error is significantly higher, because the SoC is reset in the reference SoC integration. In combination with the model mismatch, this leads to an estimation error of up to $10\,\%$. Nevertheless, the voltage behavior is very similar around a wide range of approximately $50\,\%$ SoC, which makes an accurate estimation significantly below $10\,\%$ very difficult. In comparison with the battery module SoC estimation, this influence is reduced due to the higher voltage deviations.
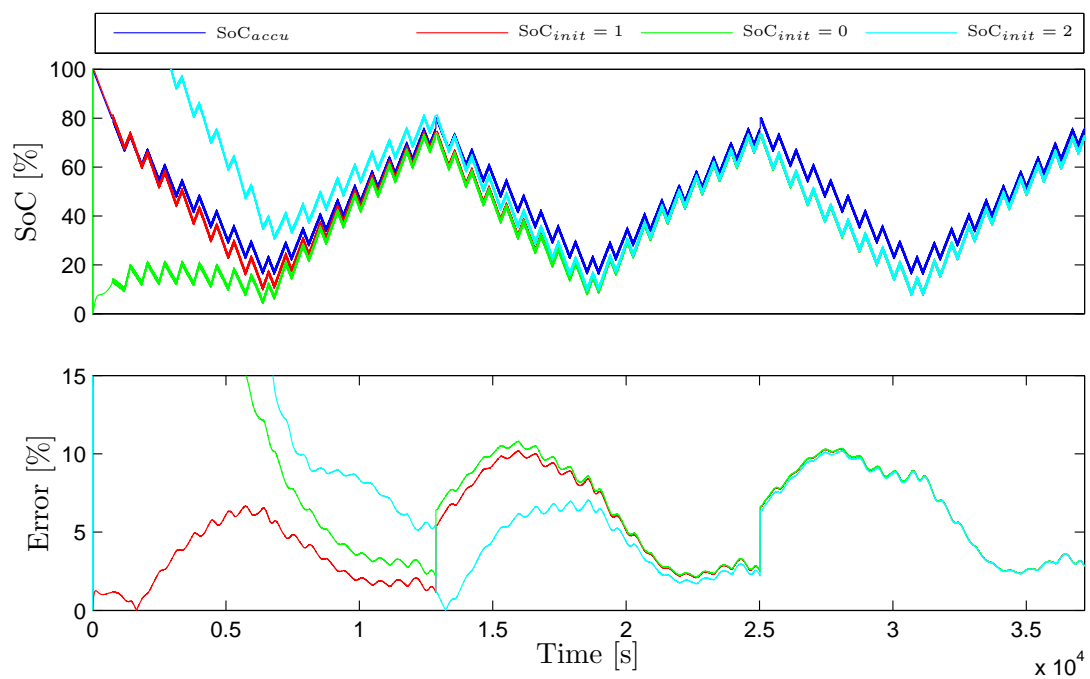
Figure 3.23: SoC estimation of battery cells with different initial SoC values.

Chapter 4

Energy Management

4.1 Introduction

The energy management in hybrid electric vehicles in non-road application is the superordinated control of the overall energy flows and influences the system behavior of the powertrain significantly. Minimization of the overall energy flows, exhaust emissions as well as fuel consumption are the primary objectives of the EMS, while all physical constraints of the system need to be taken into account [130]. Due to the multiple energy conversions from and into the battery, the minimization of the losses is essential and can only be achieved by an optimization of the overall system. However, in general the overall system is strongly nonlinear and differs significantly between different applications. A generic EMS in terms of applicability and cost reductions is therefore favorable. In this chapter, the energy management system is described in detail and methodologies to improve the EMS performance are introduced.

4.1.1 Challenges for energy management systems

Characteristic for non-road vehicles is the unknown high dynamic load acting on the powertrain. Compared to on-road vehicles, the driving directions and conditions as well as working tasks change very often in non-road vehicles and depend directly on the driver. In this context, the control of the powertrain has to cope with these circumstances to fulfill the requirement of a robust operation and the obviation of engine stalling. Additional to the external circumstances, different strategies such as a limited ICE torque gradient to reduce exhaust emissions (phlegmatisation) [93], [110] and a lowered average rotational speed to reduce fuel consumption (downspeeding), influence the degrees of freedom to control the powertrain.

Vehicle misuse or driver errors often lead to unexpected load peaks, while noise corrupted (measured) variables pretend the wrong actual state of the vehicle. Especially the actual load value, which is obtained by the calculation from different signals, and the torque values, which are obtained by the control units instead of being measured, are relevant for the controller. In terms of minimization of the losses, cyclical operated vehicles are often especially challenging, because higher SoC variations increase the usage of the electrical system. Nevertheless, the potential for fuel and emission reduction of cyclical operated vehicles is higher if the load cycle can be considered in the EMS. The required predictions of the future load trajectories are difficult to achieve though and can only be based on statistical evidence, which is subject to inaccuracies. Driver information, which is mostly not available in advance, can be considered for prediction of the future load requirements, but however, the difficulty is to predict the future load cycle sufficiently accurate and in particular at often changing load cycles. In the end, a multidimensional nonlinear optimization problem results that needs to be solved in real time in each time step to obtain the optimal control values, which is additionally tightened by the

nonlinear behavior of the electrical system [97].

4.1.2 State-of-the-Art

The field of EMS in HEV is strongly investigated, while only some of the authors consider load predictions to improve their proposed energy management systems. In the following, the state-of-the-art in EMS and load prediction is reviewed.

Desai et al. [29] classified and compared various control strategies to provide novel development directions in HEV. In [115], three different energy management approaches are compared, but a priori knowledge of the future load demand is not considered. A model based strategy to control the load of an on-road parallel HEV is proposed in [129], which also does not include the future driving conditions in the concept. In [92], dynamic programming is applied to simulation data in order to extract a rule-based controller as power management for a parallel hybrid truck. By accepting a small increase in fuel consumption, real time capability and a significant emission reduction could be achieved by the extracted controller. Poursamad et al. [120] tuned a genetic-fuzzy control strategy with a genetic algorithm based on three driving cycles including NEDC[1], FTP[2] and TEH-CAR[3]. Stochastic dynamic programming is used by [105] to optimize a power management for plug-in HEV over a distribution of drive cycles, rather than a single cycle. Furthermore, fuel and electricity usage are explicitly traded off and the impact of variations in relative fuel-to-electricity pricing is considered. In general, off-line optimization may lead to suboptimal control of non-road vehicles, since the load demand is unknown in advance.

For on-road vehicles several approaches are known that predict the future load demand in order to be considered in the energy management. An approach with exponentially decreasing torque demand across the prediction horizon is used by [167] and [15]. Lin et al. [91] proposed a driving pattern recognition to classify the current state into one of six representative driving patterns for which implementable sub-optimal controllers are extracted. Analytical approaches for future load demands are very difficult or impossible to find, since load trajectories of non-road vehicles are normally unknown in advance. A genetic-fuzzy HEV control is used by [104], which classifies driving patterns by Hidden Markov models. Hulnhagen et al. [67] used a probabilistic finite-state machine to merge basic maneuver elements to a driving pattern of on-road vehicles. The classification into driving patterns or basic maneuver elements are not suitable for non-road HEV, because in most non-road applications the elements are not clearly assignable. Since map information is not available for non-road vehicles, GPS data based path-forecasting for trajectory planning (c.f. [77, 39]), as mentioned for on-road vehicles by [130] and [5], is not feasible. Payri et al. [114] extracts an estimate for the future driving conditions by analyzing the power demands in a given receding horizon and uses the information in a stochastic controller. The prediction of recurrent load cycles used by [101] is based on the cross correlation function algorithm proposed by [95] that originally detected cycle boundaries automatically for a statistic evaluation. The disadvantage of the autocorrelation function is the slow detection of a changing load cycle at significantly different cycle times [152].

In summary, no on-line implemented MPC for non-road application is known, that features real time prediction of the future load demand in the MPC.

4.1.3 Solution approach

In the following, a cascaded control concept is proposed for the parallel hybrid powertrain schematically depicted in Figure 1.4. Additionally, two methodologies are presented to predict the future short term load and to detect recurrent load cycles in the past load signal. The

---

[1]New European Driving Cycle
[2]EPA Federal Test Procedure
[3]Car driving cycle for the capital city of Tehran.

proposed cascaded control concept consists of two separate controllers, which are both designed as model predictive controllers. In this context, MPCs provide the required possibilities to achieve an optimization of the overall system with consideration of the load predictions [100]. Note that an advanced solving algorithm as presented for the optimization problem and sufficient computational capabilities in the HCU are required to achieve real time capability.

The operation of the powertrain on the optimal load cycle trajectory can increase the overall efficiency and fully exploit the battery capacity. To this end, the cross correlation function (CCF) is used by a cycle detection algorithm to identify a recurrent load cycle within the past load signal that is further used to built the future load trajectory for the master MPC. Based on the detected recurrent load cycle, the master MPC is designed to provide the optimal operation point of the ICE as demand value for the slave controller, while the SoC of the battery is kept at the demand SoC and constraints as well as the nonlinearities of the electrical system are considered. In this context, the electrical system of the hybrid powertrain provides to boost at high load demands and to recuperate regenerative loads, but the battery capacity and physical constraints restrict it's usage, which furthermore reduces the degrees of freedoms to a certain operation range of the ICE. Within the master controller, a nonlinear optimization problem results, which is iteratively solved by a real-time capable relaxation approach.

Purpose of the slave MPC is to apply the demands of the master MPC to the powertrain, while constraints are considered. The ICE dynamics is significantly limited by the phlegmatisation and downspeeding strategies, which is disadvantageous for the high dynamic requirements of non-road vehicles. However, in order to prevent engine stalling and being able to lower the average rotational speed of the powertrain, Bayesian inference is applied to statistically predict the future short term load by means of available vehicle information such as accelerator position or driving speed (load prediction algorithm). This approach provides insight into the intentions of the driver and allows an increase of the rotational speed in case of sudden load peaks, which compensates the disadvantage of the restricted ICE dynamics. Nevertheless, the short term load prediction is based on probabilities and misprediction is considered. Furthermore, the convergence of the master MPC and the essential stability of the slave MPC are discussed, since the controller directly acts on the vehicle.

4.2 Basic concept of model predictive control

Model predictive control is an advanced method in control theory, which is suited to solve constrained control problems in the time domain. Different types such as Dynamic Matrix Control (DMC), Model Algorithmic Control (MAC), Generalized Predictive Control (GPC), etc. are known, but the main principle is similar for all approaches. The idea of the concept is to obtain the control moves for a process based on an on-line optimization of an objective (cost) function. A dynamic process model is used to predict the system output over a so called *prediction horizon*. In order to minimize the control error, the sequence of control moves over a so called *control horizon*, is optimized until the cost function reaches a minimum. Only the first control move in the obtained sequence is applied to the plant, the horizons are moved for one sample (*receding horizon principle*) and the optimization is done anew.

Process Model The process model has a substantial influence on the MPC. It is therefore important that the process model fully captures the process dynamics and allows accurate predictions of the output. In general two main methodologies can be used to obtain a process model: Modeling by physical principles to obtain a *white box* model or data-based system identification to obtain a *black box* model. Independent to the method of parameter determination, different types of process model representations can be used in the MPC. Commonly a state

space representation

$$\boldsymbol{x}(k + 1) = \boldsymbol{A}\boldsymbol{x}(k) + \boldsymbol{B}\boldsymbol{u}(k) + \boldsymbol{E}\boldsymbol{z}(k), \tag{4.1}$$

$$y(k) = \boldsymbol{C}\boldsymbol{x}(k), \tag{4.2}$$

is implemented though, where $\boldsymbol{A}, \boldsymbol{B}, \boldsymbol{C}, \boldsymbol{D}, \boldsymbol{E}$ are the system matrices including the system dynamics, $\boldsymbol{x}$ is the state vector, $\boldsymbol{u}$ is the input vector, y is the output, $\boldsymbol{z}$ is the disturbance vector and the time instant is denoted by k.

Real processes are in many cases nonlinear, which means that system parameters depend on system states or/and time. Linearization is one possibility to map the system behavior into one invariant SS-system with the disadvantage of reduced model accuracy. Nonlinear system behavior can be represented by e.g. local model networks (see Section 2.2), which use in principle local linearizations to calculate the nonlinear system behavior. A fuzzy MPC [4] can handle the LMN model to consider the nonlinearities. Another nonlinear MPC approach is presented in the following sections and more information can be found in e.g. [2].

In Figure 4.1, the principle of MPC is depicted for a single-input-single-output (SISO) system. The blue trajectory indicates the system output, if the red control moves and the grey disturbance acting on the plant, while the green trajectory shows the system states. As can be seen in the figure, the input and state trajectory keep the applied constraints of the plant.
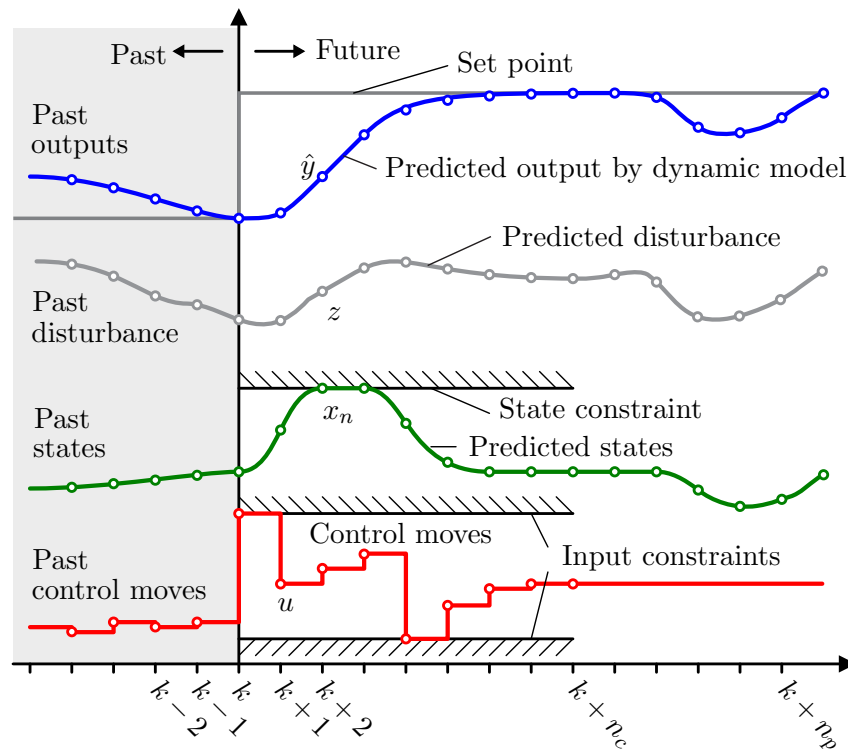

Figure 4.1: Principle of model predictive control trajectories

Prediction and Control Horizon   As can further be seen in Figure 4.1, the control moves are kept constant on the last calculated value $u(k+i) = u(k+n_c)$ for $i = n_c, \ldots, n_p - 1$ until the end of the prediction horizon n_p [4], [159]. In order to predict further into the future, the prediction horizon n_p is chosen larger than the control horizon n_c, since n_c determines the number of manipulated variables and thus affects the computation time. Due to the process model, the predicted output values $\hat{y}(k + i|k)$, $i = 1, \ldots, n_p$ are influenced by the current state of the process at time instant k and the future control moves $u(k + i)$, $i = 0, \ldots, n_c - 1$. However, the

prediction and control horizons are tuning parameters and no general rule for optimal horizons exists.

Objective Function   In order to optimize the control moves, an objective function needs to be formulated. A common cost function J is

$$J = \sum_{i=1}^{n_p} Q_i [r(k+i) - \hat{y}(k+i|k)]^2 + \sum_{i=1}^{n_c} \Delta u^T(k+i-1) R_i \Delta u(k+i-1), \qquad (4.3)$$

where n_p and n_c denote the prediction and control horizon, respectively, the prediction of the output is indicated by $\hat{y}(k+i|k), i = 1, 2, \ldots$ for time instant k at prediction instant i and Q_i, R_i weight output error and control effort, respectively. Note that in absence of constraints, an explicit analytical solution can be found, due to the quadratic nature of the cost function.

4.3   Cascaded model predictive controller design

In this section, the cascaded model predictive controller design for parallel hybrid electric vehicles is discussed. The architecture and system models are developed first, before constraints and both MPCs are discussed in detail. Methodologies to predict the future load trajectory are discussed in the next section (see Section 4.4).

4.3.1   Architecture of the control concept

In the following the controller architecture is briefly discussed to give a better overview of the concept. The powertrain consists of significantly different dynamics. Rotational speed and the torques represent fast dynamics within the ms time range. On the other hand, the battery's state of charge is only slowly changing within the seconds time range. This difference is addressed by the cascaded control concept, which include a slow master controller and a fast slave controller both established as MPC. However note that the interaction between inverter and battery also has a fast electrical impedance time constant, which is not relevant to the in this work referred change in SoC [52].
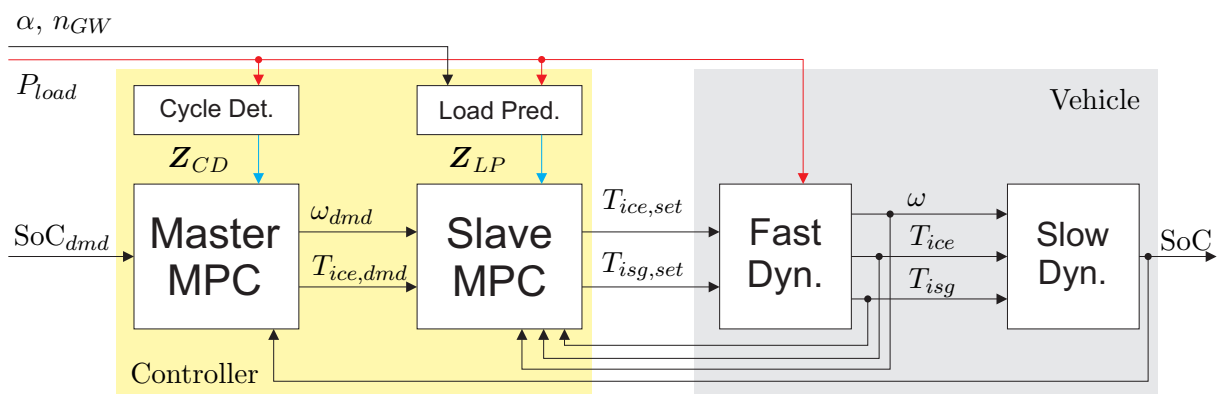

Figure 4.2: Overview of the cascaded controller scheme.

In Figure 4.2, the concept is depicted schematically, where the yellow area represents the EMS and the gray area the vehicle. The load P_{load} (red) acts as the unknown disturbance of the powertrain, n_{GW} is the driving speed and α is the accelerator angle that is directly influenced by the driver. Note that the actual SoC can be obtained by the SoC estimator presented in Section 2.6 and is therefore assumed to be known. The aim of the master MPC is to hold the

control variable SoC at the demand value SoC_{dmd}, while a full recurrent load cycle as well as all constraints are considered. In the concept, the cycle detection (Cycle Det.) provides the predicted future load trajectory $\boldsymbol{Z}_{CD}$ for the master MPC, while due to an optimization, the optimal values for the demand rotational speed ω_{dmd} and ICE torque $T_{ice,dmd}$ are obtained. Note that the prediction of the SoC trajectory within the master MPC depends on the battery conditions and is thus strongly nonlinear. In principle, the output of the master MPC defines the operation point of the ICE. The aim of the slave MPC is then to compensate unpredicted short term load peaks by considering the load prediction (Load Pred.) methodology that provides the short term load trajectory $\boldsymbol{Z}_{LP}$ for the slave MPC. Constraints are especially important to be kept by the slave MPC, since the manipulated variables ICE torque $T_{ice,set}$ and ISG torque $T_{isg,set}$ directly act on the vehicle. In this context, it is worth mentioning that the rotational speed ω is only controlled by ICE torque T_{ice} and ISG torque T_{isg}, respectively. Note that sufficient powertrain dynamics in case of strong load gradients must be guaranteed, which due to the slow sampling time $t_{s,m} = 0.25\,\text{s}$ of the master MPC must be compensated by the slave MPC. To this end, also not or wrong detected load cycles must be compensated. The CD and LP methodologies aim to find the a-priori unknown future load trajectories only based on the actual during operation available system states P_{load}, α and n_{GW}, which is discussed in more detail in the next subsection (cf. Subsection 4.4).

4.3.2 System models for controller design

The models for the slow as well as fast system dynamics of the plant are required by the design of the MPCs and are developed in the following.

First order lag elements and the principle of angular momentum, respectively, can be used to model the fast dynamics of the rotational speed and the torques in the continuous time domain (c.f. [121, 34]), which follow to

$$T_{ice}(t) + T_{isg}(t) - T_{load}(t) = \Theta\,\dot{\omega}(t), \tag{4.4}$$

$$\tau_{ice}\,\dot{T}_{ice}(t) + T_{ice}(t) = T_{ice,set}(t), \tag{4.5}$$

$$\tau_{isg}\,\dot{T}_{isg}(t) + T_{isg}(t) = T_{isg,set}(t). \tag{4.6}$$

In equations (4.4)-(4.6), the powertrain's total moment of inertia is denoted by Θ, the time constants of the torques are denoted by τ_{ice}, τ_{isg} and $T_{load}(t) = P_{load}(t)/\omega(t)$. The ICE is in general a nonlinear system, but the dependence of T_{ice} on ω is neglected. In order to consider the variant time constant of the ICE, τ_{ice} can be updated in each time instant to improve the control quality of the slave controller. Nevertheless, for the main focus of this work, the simplified model of the ICE dynamic is satisfactory because important is that time delays from the components are addressed in the process model of the controller and feasibility of the concept can be shown.

For the SS-representation of the slave MPC process model, the input vector $\boldsymbol{u}_s$, state vector $\boldsymbol{x}_{d,s}$, output $y_{d,s}$ and disturbance z_s can be chosen to

$$\boldsymbol{x}_{d,s} = \begin{bmatrix} \omega \\ T_{ice} \\ T_{isg} \end{bmatrix}, \ \ y_{d,s} = \omega, \ \ \boldsymbol{u}_s = \begin{bmatrix} T_{ice,set} \\ T_{isg,set} \end{bmatrix}, \ \ z_s = T_{load}, \tag{4.7}$$

while the fast sampling time of the slave controller is defined by $t_{s,s} = 10\,\text{ms}$. The discrete linear state space slave controller model is obtained by

$$\boldsymbol{x}_{d,s}(k+1) = \boldsymbol{A}_{d,s}\boldsymbol{x}_{d,s}(k) + \boldsymbol{B}_{d,s}\boldsymbol{u}_s(k) + \boldsymbol{E}_{d,s}T_{load}(k), \tag{4.8}$$

$$\omega(k) = \boldsymbol{C}_{d,s}\boldsymbol{x}_{d,s}(k), \tag{4.9}$$

where

$$
\boldsymbol{A}_{d,s} = \begin{bmatrix} 1 & \frac{t_{s,s}}{\Theta} & \frac{t_{s,s}}{\Theta} \\ 0 & \frac{\tau_{ice}}{\tau_{ice}+t_{s,s}} & 0 \\ 0 & 0 & \frac{\tau_{isg}}{\tau_{isg}+t_{s,s}} \end{bmatrix}, \boldsymbol{C}_{d,s} = \begin{bmatrix} 1 & 0 & 0 \end{bmatrix},
$$

$$
\boldsymbol{B}_{d,s} = \begin{bmatrix} 0 & 0 \\ \frac{t_{s,s}}{\tau_{ice}+t_{s,s}} & 0 \\ 0 & \frac{t_{s,s}}{\tau_{isg}+t_{s,s}} \end{bmatrix}, \qquad \boldsymbol{E}_{d,s} = \begin{bmatrix} \frac{t_{s,s}}{\Theta} \\ 0 \\ 0 \end{bmatrix}.
$$
(4.10)

The process model for the master MPC needs to constitute the relation between ISG torque and the resulting battery SoC. Based on the fact that integral of the battery current $I(t)$ and SoC are proportional [51], a corresponding model is obtained by

$$
\text{SoC}(t) = \text{SoC}_{init} + \frac{1}{Q_{c,batt}} \int_0^t \eta_{batt,Cou}(I(\nu)) \, I(\nu) d\nu, \tag{4.11}
$$

$$
I(t) = k_I \left(T_{isg,dmd}, \omega_{dmd}, V \right) T_{isg,dmd}(t), \tag{4.12}
$$

where SoC_{init} is the initial SoC of the battery. The relation between current and SoC is defined by battery capacity $Q_{c,batt}$ and coulombic efficiency $\eta_{batt,Cou}$, while the proportionality between ISG torque and current is denoted by k_I. Note that the battery current $I(t)$ is a nonlinear function of ISG torque, speed and battery voltage. Since the voltage depends on the current itself, the equations lead to an implicit form [101].

The difference between load and ICE torque define the ISG torque, which follows to

$$
T_{isg,dmd}(t) = \frac{P_{load}(t)}{\omega_{dmd}(t)} - T_{ice,dmd}(t). \tag{4.13}
$$

The nonlinear proportionality k_I is invariant during transient operation and can therefore statically determined by testbed measurements. A characteristic map of k_I can be extracted, which includes the motor and drive efficiencies at different voltage levels. By means of analytical polynomial surface approximation of each voltage level of the identified characteristic map, the current can be expressed by

$$
I(\omega_{dmd}, T_{isg})_v = p_{00,v} + p_{10,v} \, \omega_{dmd} + p_{01,v} \, T_{isg} + p_{20,v} \, \omega_{dmd}^2 + p_{02,v} \, T_{isg}^2 + p_{11,v} \, \omega_{dmd} T_{isg}, \tag{4.14}
$$

where p_{ij} are least squares identified parameters and v corresponds to the voltage level. Note that the analytical approximation has sufficient accuracy and simplifies the further process significantly. Differentiation of $I(\omega_{dmd}, T_{isg})_v$ with respect to the ISG torque follows to

$$
k_{I,v} = \frac{dI(\omega_{dmd}, T_{ISG})_v}{dT_{isg}} = p_{01,v} + 2 \, p_{02,v} \, T_{isg} + p_{11,v} \, \omega_{dmd}. \tag{4.15}
$$

In order to obtain the value of k_I, the obtained analytic equation for $k_{I,v}$ can be linearly interpolated between the different voltage levels

$$
k_I = k_{I,v_i} + \frac{k_{I,v_j} - k_{I,v_i}}{v_j - v_i} \left(V - v_i \right), \tag{4.16}
$$

where V is the terminal voltage of the battery. Note that for the purpose of the state prediction, a battery model is required to provide a value for V in the prediction.

The system behavior of electrochemical batteries is nonlinearly dependent on SoC, temperature ϑ_{batt} and current I [150]. Nonlinear effects such as relaxation and hysteresis are observable as well [117]. A powerful approach is a local model network, though several approaches are known for battery modeling (see Section 2). LMN comprise of local linear dynamic models,

each of which is valid in a certain operating region of a partition space [50]. The mentioned effects are considered by corresponding inputs, while the global nonlinear model output is obtained by weighted aggregation of the LLM outputs. Automatic iterative algorithms (e.g. [108], [70]) are used to built the LMN structure. A complete discussion about battery modeling with LMN is given in Section 2.

Since dynamic models require past system inputs and outputs, the output trajectory for a given input trajectory requires a simulation. The computational demand of dynamic models is therefore significantly higher than for parameter varying static models. Due to this reason, in the EMS, a simplified equivalent circuit battery model is used, which is depicted schematically in Figure 4.3 (see e.g. [65]).
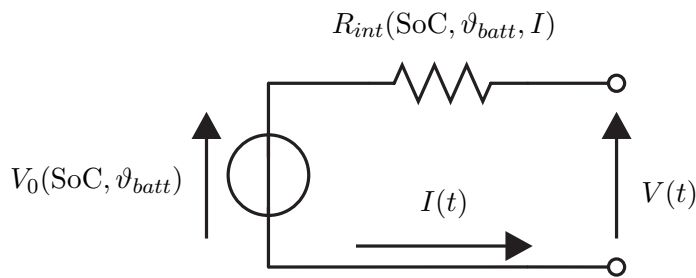
Figure 4.3: Simplified equivalent circuit model of a battery.

In order to consider the nonlinear parameter varying nature of batteries, look-up tables of the values of inner resistance $R_{int}(\text{SoC}, \vartheta_{batt}, I)$ and open circuit voltage $V_0(\text{SoC}, \vartheta_{batt})$ are extracted from an identified LMN. Applying Kirchhoff's second law, the battery voltage follows by

$$V(t) = V_0(\text{SoC}, \vartheta_{batt}) - R_{int}(\text{SoC}, \vartheta_{batt}, I)\, I(t). \tag{4.17}$$

Note that other modeling and prediction inaccuracies have large influences due to which the effect of the decreased battery model accuracy is of no consequence. Discretizing equation (4.11) using the master sampling time $t_{s,m}$ leads to a discrete time state space representation of the SoC model. Accumulation of the discrete current $I(k)$ multiplied with

$$k_{batt}(k) = \frac{\eta_{batt,Cou}(k)\, t_{s,m}}{Q_{c,batt}}, \tag{4.18}$$

where the coulombic efficiency $\eta_{batt,Cou}(k)$ of the battery

$$\eta_{batt,Cou}(k) = \begin{cases} \eta_{cha} = 0.99 & \text{for } I(k) > 0, \\ \eta_{dis} = 1 & \text{for } I(k) < 0, \end{cases} \tag{4.19}$$

is obtained by [155], approximates the integral in equation (4.11). Choosing the input u_m, state $x_{d,m}$, output $y_{d,m}$ and disturbance z_m of the system by

$$x_{d,m} = y_{d,m} = \text{SoC}, \quad u_m = T_{ice,dmd}, \quad z_m = T_{load}, \tag{4.20}$$

the discrete SS representation of equations (4.11)-(4.19) follows to

$$x_{d,m}(k+1) = A_{d,m}x_{d,m}(k) + B_{d,m}(k)u_m(k) + E_{d,m}(k)z_m(k), \tag{4.21}$$
$$y_{d,m}(k) = C_{d,m}x_{d,m}(k), \tag{4.22}$$

with

$$\begin{aligned} A_{d,m} &= 1, \quad B_{d,m}(k) = -k_I(x_{d,m}, u_m, z_m, k)\, k_{batt}(u_m, z_m, k), \\ C_{d,m} &= 1, \quad E_{d,m}(k) = k_I(x_{d,m}, u_m, z_m, k)\, k_{batt}(u_m, z_m, k), \end{aligned} \tag{4.23}$$

where the parameter varying structure of the ECM is directly integrated in k_I.

4.3.3 Structured constraints for controllers

The system states of both controllers do not directly include the battery current and voltage as well as the temperature of the ISG and the battery. Thus these constraints need to be considered indirectly by structured constraints. In this context, structured constraints means to apply only the most constraining value, while current, voltage and temperatures can be limited by increasing/decreasing the ISG torque. Equations (4.24)-(4.32) summarize all relevant structured constraints:

$$\hat{\omega}_{min} = \max \begin{cases} \omega_{min} \\ \omega_{min,driver} \end{cases} , \tag{4.24}$$

$$\hat{T}_{ice,min} = \max \begin{cases} T_{ice,min}(\omega) \\ \frac{P_{load}}{\omega_{dmd}} - \hat{T}_{isg,min} \end{cases} , \tag{4.25}$$

$$\hat{T}_{ice,max} = \min \begin{cases} T_{ice,max}(\omega) \\ \frac{P_{load}}{\omega_{dmd}} - \hat{T}_{isg,max} \end{cases} , \tag{4.26}$$

$$\hat{T}_{isg,min} = \max \begin{cases} T_{isg,min}(\omega, V) \\ T_{isg,min}(\vartheta_{isg}, \vartheta_{batt}) \\ T_{isg,min}(\text{SoC}) \\ T_{isg,min}(V, I) \end{cases} , \tag{4.27}$$

$$\hat{T}_{isg,max} = \min \begin{cases} T_{isg,max}(\omega, V) \\ T_{isg,max}(\vartheta_{isg}, \vartheta_{batt}) \\ T_{isg,max}(\text{SoC}) \\ T_{isg,max}(V, I) \end{cases} , \tag{4.28}$$

$$I_{min} \leq I \leq I_{max}, \tag{4.29}$$
$$V_{min} \leq V \leq V_{max}, \tag{4.30}$$
$$\vartheta_{batt,min} \leq \vartheta_{batt} \leq \vartheta_{batt,max}, \tag{4.31}$$
$$\vartheta_{isg,min} \leq \vartheta_{isg} \leq \vartheta_{isg,max}, \tag{4.32}$$

where $\omega_{min,driver}$ is the minimal rotational speed required by the driver and ϑ denotes the temperatures. Based on the characteristic maps providing the values based on the actual states of the system (see corresponding function arguments), min/max correspond to the minimal and maximal constraints obtained. Note that $f(V, I)$ additionally constrains the maximal/minimal battery power.

The finally applied set of constraints for the slave controller can be summarized by

$$\mathcal{C}_s = \begin{cases} \hat{\omega}_{min} \leq \omega \leq \omega_{max} \\ \Delta T_{ice,min} \leq \Delta T_{ice,set} \leq \Delta T_{ice,max} \\ \Delta T_{isg,min} \leq \Delta T_{isg,set} \leq \Delta T_{isg,max} \\ \hat{T}_{ice,min} \leq T_{ice,set} \leq \hat{T}_{ice,max} \\ \hat{T}_{isg,min} \leq T_{isg,set} \leq \hat{T}_{isg,max} \end{cases} , \tag{4.33}$$

where the backwards difference operator Δ indicates rate constraints. The set of constraints for

the master controller follows to

$$\mathcal{C}_m = \begin{cases} \Delta T_{ice,min} \leq \Delta T_{ice,dmd} \leq \Delta T_{ice,max} \\ \hat{\omega}_{min} \leq \omega_{dmd} \leq \omega_{max} \\ \hat{T}_{ice,min} \leq T_{ice,dmd} \leq \hat{T}_{ice,max} \\ \mathrm{SoC}_{min} \leq \mathrm{SoC} \leq \mathrm{SoC}_{max} \end{cases} . \tag{4.34}$$

All given constraints are considered in the control system.

4.3.4 Slave controller

In the following, the slave MPC is discussed in detail. The demand values rotational speed ω_{dmd} and ICE torque $T_{ice,dmd}$ are applied to the plant, while the used manipulated variables $T_{ice,set}$, $T_{isg,set}$ need to keep the constraints.

Slave MPC formulation

An augmentation of the process model (4.8),(4.9) provides the possibility to directly constrain the gradient of the manipulated variables as well as allows an offset free control by avoiding a steady state bias [17]. The augmentation is done by embedding an integrator which leads to an incremental plant description [111]

$$\underbrace{\begin{bmatrix} \Delta \boldsymbol{x}_{d,s}(k+1) \\ y_{d,s}(k+1) \end{bmatrix}}_{\boldsymbol{x}_s(k+1)} = \underbrace{\begin{bmatrix} \boldsymbol{A}_{d,s} & \boldsymbol{0} \\ \boldsymbol{C}_{d,s}\boldsymbol{A}_{d,s} & 1 \end{bmatrix}}_{\boldsymbol{A}_s} \underbrace{\begin{bmatrix} \Delta \boldsymbol{x}_{d,s}(k) \\ y_{d,s}(k) \end{bmatrix}}_{\boldsymbol{x}_s(k)}$$

$$+ \underbrace{\begin{bmatrix} \boldsymbol{B}_{d,s} \\ \boldsymbol{C}_{d,s}\boldsymbol{B}_{d,s} \end{bmatrix}}_{\boldsymbol{B}_s} \Delta \boldsymbol{u}_s(k) + \underbrace{\begin{bmatrix} \boldsymbol{E}_{d,s} \\ \boldsymbol{C}_{d,s}\boldsymbol{E}_{d,s} \end{bmatrix}}_{\boldsymbol{E}_s} \Delta z_s(k), \tag{4.35}$$

$$\omega(k) = \underbrace{\begin{bmatrix} \boldsymbol{0} & 1 \end{bmatrix}}_{\boldsymbol{C}_s} \boldsymbol{x}_s(k), \tag{4.36}$$

where $\boldsymbol{x}_s$ is the augmented state vector, $\Delta \boldsymbol{u}_s$ is the incremental input, Δz_s is the incremental disturbance and $\boldsymbol{0}$ represents a zero matrix with corresponding dimension. A sequence of $n_c = 25$ incremental control moves

$$\Delta \boldsymbol{U}_s(k) = \begin{bmatrix} \Delta \boldsymbol{u}_s(k+1)^T & \dots & \Delta \boldsymbol{u}_s(k+n_c)^T \end{bmatrix}^T, \tag{4.37}$$

can be found that minimizes a cost function

$$J_s = Q_s \sum_{i=1}^{n_p-1} (\omega_{dmd}(k+i) - \omega(k+i))^2 + \sum_{i=0}^{n_c-1} (\Delta \boldsymbol{u}_s^T(k+i)\boldsymbol{R}_s\Delta \boldsymbol{u}_s(k+i))$$

$$+ \sum_{i=0}^{n_c-1} (\Delta \tilde{\boldsymbol{u}}_s^T(k+i)\tilde{\boldsymbol{R}}_s\Delta \tilde{\boldsymbol{u}}_s(k+i)) + V_{f,s}(\boldsymbol{x}_s(k+n_p)), \tag{4.38}$$

with $V_{f,s}(\boldsymbol{x}_s(k+n_p)) = \boldsymbol{x}_s(k+n_p)^T \boldsymbol{P}_s \boldsymbol{x}_s(k+n_p)$, where the term $V_{f,s}$ is a terminal weight. In principle, the cost function J_s has no unique minimum, since the torque split between ICE and ISG is not uniquely defined. For this reason, the term $\Delta \tilde{\boldsymbol{u}}_s = \begin{bmatrix} T_{ice,dmd} & T_{isg,dmd} \end{bmatrix}^T - \boldsymbol{u}_s$ penalizes the deviations of the manipulated variables from the demand values provided by the master MPC and forces $\boldsymbol{u}_s$ to reach the demand values at steady state if no constraints are violated (c.f. [45]).

Output, input rate and input respectively are penalized by user-defined, symmetric and positive definite weighting matrices Q_s, R_s and $\tilde{R}_s$. The solution of the discrete algebraic Riccati equation (DARE) is used as terminal weight matrix P_s, which follows to

$$P_s = A_s^T P_s A_s - K_s^T \left(R_s + B_s^T P_s B_s \right) K_s + C_s^T Q_s C_s \tag{4.39}$$

with $K_s = \left(R_s + B_s^T P_s B_s \right)^{-1} B_s^T P_s A_s$. Note that, $V_{f,s}$ is used to obtain the stabilizing properties of the linear-quadratic regulator (LQR) [84].

As mentioned in Section 4.2, there exists no general rule for the selection of the prediction as well as control horizon. However, a guideline for a minimum prediction horizon is to choose it at least large enough to cover the smallest time constant of the system, while a maximum for n_p is given by the maximal system runtime [17].

For the example of the wheel loader, usual short term load peaks occur within $250\,\text{ms}$ ahead, which leads to a prediction horizon of $n_p = 25$ chosen in this work. The matrix notation of the output prediction $\hat{Y}_s$ is obtained by

$$\hat{Y}_s = \left[\omega(k+1) \quad \cdots \quad \omega(k+n_p) \quad x_s(k+n_p)^T \right]^T$$
$$= F_s x_s(k) + \Phi_{s,u} \Delta U_s(k) + \Phi_{s,z} \Delta Z_{LP}(k), \tag{4.40}$$

where ΔZ_{LP} is the incremental disturbance trajectory predicted by the short term load prediction and the matrices F_s, $\Phi_{s,u}$ and $\Phi_{s,z}$ predict the system states based on $x_s(k)$ and $\Delta U_s(k)$:

$$F_s = \left[(C_s A_s)^T \quad (C_s A_s^2)^T \quad \cdots \quad \left(C_s A_s^{n_p-1} \right)^T \quad (A_s^{n_p})^T \right]^T, \tag{4.41}$$

$$\Phi_{s,u} = \begin{bmatrix} C_s B_s & 0 & \dots & 0 \\ C_s A_s B_s & C_s B_s & \dots & 0 \\ \vdots & \vdots & \ddots & \vdots \\ C_s A_s^{n_p-2} B_s & C_s A_s^{n_p-3} B_s & \dots & 0 \\ A_s^{n_p-1} B_s & A_s^{n_p-2} B_s & \dots & A_s^{n_p-n_c} B_s \end{bmatrix}, \tag{4.42}$$

$$\Phi_{s,z} = \begin{bmatrix} C_s E_s & 0 & \dots & 0 \\ C_s A_s E_s & C_s E_s & \dots & 0 \\ \vdots & \vdots & \ddots & \vdots \\ C_s A_s^{n_p-2} E_s & C_s A_s^{n_p-3} E_s & \dots & 0 \\ A_s^{n_p-1} E_s & A_s^{n_p-2} E_s & \dots & E_s \end{bmatrix}. \tag{4.43}$$

Following Wang et al. [159], the slave controller constraints (4.33) can be formulated by corresponding linear inequalities and directly implemented in the the optimization problem. The compact notation follows to

$$\mathcal{C}_s: \quad M_s \Delta U_s \leq \gamma_s, \tag{4.44}$$

$$\text{with} \quad M_s = \begin{bmatrix} M_{s,\Delta u} \\ M_{s,u} \\ M_{s,y} \end{bmatrix}, \quad \gamma_s = \begin{bmatrix} \gamma_{s,\Delta u} \\ \gamma_{s,u} \\ \gamma_{s,y} \end{bmatrix},$$

where the indices refer to the rate, input and output constraints, respectively. A formal formulation of the final constrained optimal control problem can be denoted by

$$\mathscr{P}_s(x_s(k)): \quad \Delta U_s^*(x_s(k)) = \arg\min J_s(x_s(k), \Delta U_s) \tag{4.45}$$
$$\text{s.t.} \quad M_s \Delta U_s \leq \gamma_s.$$

Real-time implementation

The given optimization problem (4.45) needs to be solved in each time instant, which gives a time frame of $t_{s,s} = 10\,\text{ms}$ to solve the full optimization problem. In order to reduce computational loads, in the work of Unger et al. [151], an approach to reduce the order of the formulated MPC problem by using principal control moves is presented. Following e.g. [148], [127], the idea is to parametrize $\Delta\boldsymbol{U}_s$ in equation (4.37) according to

$$\Delta\boldsymbol{U}_s = \boldsymbol{\Omega}_s\boldsymbol{p}_s, \tag{4.46}$$

where $\boldsymbol{\Omega} \in I\!\!R^{n_c \cdot n_u \times \nu_p}$ is a matrix whose columns form a basis for $\Delta\boldsymbol{U}_s$, n_u is the number of input variables and $\boldsymbol{p}_s \in I\!\!R^{\nu_p \times 1}$ is the new decision variable with reduced dimension ($\nu_p \leq n_c \cdot n_u$). The columns of $\boldsymbol{\Omega}$ describe the shape of the control increments of every manipulated variable up to the control horizon and are called *principal control moves*, while the integer variable ν_p indicates the number of columns in $\boldsymbol{\Omega}$ and is called the *order of principal control moves* (PCM-order). Replacing $\Delta\boldsymbol{U}_s$ in the constrained optimization problem (4.45) by (4.46), the optimization problem (4.45) with $\boldsymbol{p}_s$ as the new decision variable follows to

$$\mathscr{P}_p(\boldsymbol{x}_s(k)): \quad \boldsymbol{p}_s^*(\boldsymbol{x}_s(k)) = \arg\min J_{s,p}(\boldsymbol{x}_s(k), \boldsymbol{p}_s) \ \text{ s.t. } \ \boldsymbol{M}_s\boldsymbol{\Omega}_s\boldsymbol{p}_s \leq \boldsymbol{\gamma}_s. \tag{4.47}$$

Another approach for real time implementation of the MPC is the fast model predictive control (FMPC) algorithm proposed by [161]. The particular structure of the MPC problem is exploited to decrease computation times. Since the algorithm is provided for implementation, this method is used, though, the algorithm is appropriately extended to include the disturbance costs in the optimization.

Further approaches are presented in e.g. [125], [169] and [123].

Stability analysis slave controller

The stability of the slave controller is essential, since it directly acts on the plant. In order to show stability for the constrained controller, distinction is usually made between stability inside a terminal set $\mathbb{X}_f$, where no constraints are active and a region of attraction $\bar{\mathcal{X}}_N$, where constraints are active [83, 135].

Assuming that $\boldsymbol{x}_s \in \mathbb{X}_f$ and $\tilde{\boldsymbol{x}}_s(k+1) = (\boldsymbol{A}_s - \boldsymbol{B}_s\boldsymbol{K}_s)\tilde{\boldsymbol{x}}_s(k) \in \mathbb{X}_f$, a stabilizing control law $\Delta\boldsymbol{U}_s = -\boldsymbol{K}_s(\boldsymbol{x}_s - \boldsymbol{x}_s^*) = -\boldsymbol{K}_s\tilde{\boldsymbol{x}}_s$ inside the positive invariant terminal set $\mathbb{X}_f$ is obtained so that all constraints $\mathcal{C}_s$ are satisfied, when a terminal weight $V_{f,s}$ is applied to the MPC [124]. Outside the terminal set, an N-step admissible set $\mathcal{X}_N$ can be found, for which the MPC is enforced to reach $\mathbb{X}_f$ in N steps if a terminal set constraint $\boldsymbol{x}_s(k+N) \in \mathbb{X}_f$ is added to $\mathscr{P}_s(\boldsymbol{x}_s(k))$. Following [124], the terminal set constraint is usually too complex for real time implementations and can be omitted if the initial state lies inside a region of attraction $\bar{\mathcal{X}}_N$. Depending on the choice of the controller parameters, the region of attraction is defined as a sufficiently small subset of the admissible set $\bar{\mathcal{X}}_N \subseteq \mathcal{X}_N$.

A terminal set $\mathbb{X}_f$ for the given controller can be calculated following the algorithm proposed by [43], while Keerthi et al. [78] proposed an algrithm to calculate $\mathcal{X}_N$. Since the state vector only consists of three variables, $\mathbb{X}_f$ and $\mathcal{X}_N$ can be determined straightforward and depicted in a 3-D figure. Figure 4.4 depicts the terminal set $\mathbb{X}_f$ and the 25-step admissible set $\mathcal{X}_{25}$. Additionally the state trajectories with initial states inside (black) and outside (red) $\mathcal{X}_{25}$ are depicted as well.

As can be seen in the figure, both trajectories converge to the origin, while the black trajectory reaches $\mathbb{X}_f$ in less than 25 samples. Since the initial state of the red trajectory is outside the admissible set, the controller needs almost 23 samples (corresponds to $230\,\text{ms}$) to reach $\mathcal{X}_{25}$.
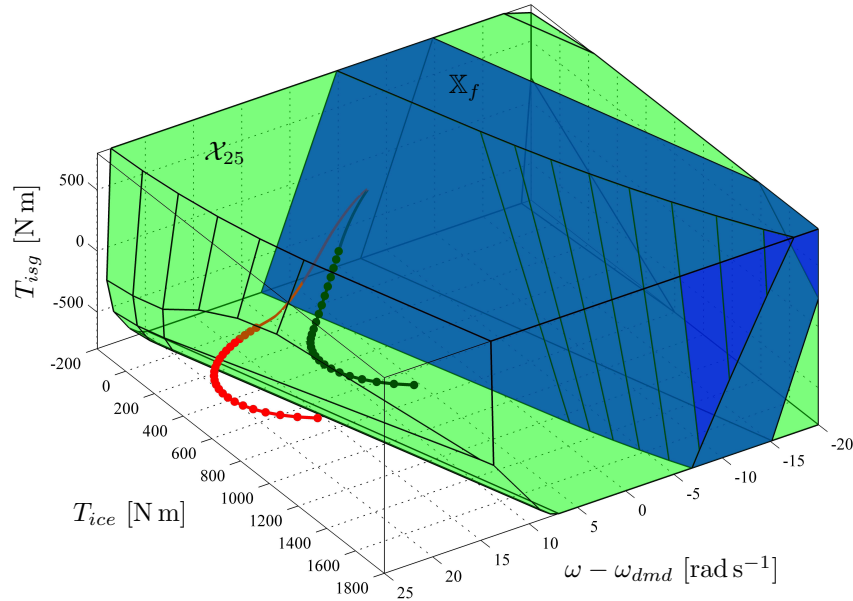
Figure 4.4: Terminal set $\mathbb{X}_f$ and 25-step admissible set $\mathcal{X}_{25}$ of slave MPC with $\omega_{dmd} = 100\,\text{rad/s}$. Black: State trajectory with initial state inside $\mathcal{X}_{25}$. Red: State trajectory with initial state outside $\mathcal{X}_{25}$.

The slightly increase of the rotational speed in both cases results from the input constraints which implies due to the compensation of the excessive torque.

Note that the prove of stability does not guarantee that engine stalling is avoided and that due to this reason, the load must lie within the feasible range of the powertrain. The stability of the control loop is also not effected by unpredicted disturbances, though the performance of the control loop is mainly depending on the controller tuning which may cause poor performance in case of prediction errors.

4.3.5 Master controller

The goal of the master controller is to take SoC_{dmd} as a reference value and provide the demand set point values speed ω_{dmd} and ICE torque $T_{ice,dmd}$ for the slave controller. Due to the nonlinear behavior of the plant, optimal demand values are only obtained if the nonlinearities are considered [97]. In the following, the concept and design of the master controller are developed in detail and the convergence of the iterative approach is discussed.

Concept of master controller

A link between the applied load of the powertrain and the battery SoC must be established in the controller. Due to this reason, following the SoC model in Section 4.3.2, the nonlinear function k_I in (4.12) links the SoC to the ISG torque, which is proportional to the current of the battery. In each time as well as prediction step the model changes, which results in a nonlinear optimization problem to be solved in real time. A solution of the optimization problem can only be achieved by an iterative approach. The master controller is designed to consider a full load cycle duration in the optimization. In this work, a solution approach is proposed that consists of an inner iteration loop, a linear optimization $\mathscr{P}(\boldsymbol{x}_m)$ as well as an outer iteration loop. The flowchart in Figure 4.5 depicts the concept schematically, where the variables refer to the trajectories across the prediction horizon N_p. Note that the minimum prediction horizon

is defined in such a way that the full cycle duration can be considered, while the real time capability gives an upper limit for N_p. Due to consideration of the entire load cycle within the optimization, the energy storage can be fully exploited. In the following, the concept is discussed in more detail.
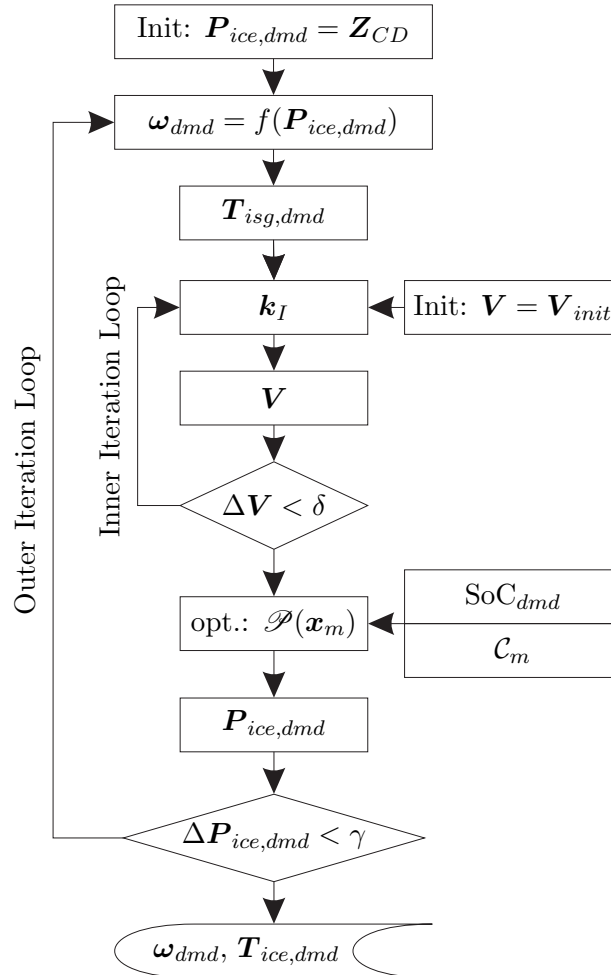

Figure 4.5: Flowchart of the master controller concept.

Inner iteration loop

In the inner iteration loop, a relaxation approach is used to consider the influence of the battery behavior. The implicit equations for the SoC model are evolved for optimization by using the predicted load trajectory $\boldsymbol{Z}_{CD} \in \mathbb{R}^{N_p}$ to initialize the ICE load trajectory $\boldsymbol{P}_{ice,dmd} \in \mathbb{R}^{N_p}$ and to obtain the optimal demand speed trajectory $\boldsymbol{\omega}_{dmd} \in \mathbb{R}^{N_p}$ from a characteristic map of the ICE. From (4.13) follows the ISG demand torque trajectory $\boldsymbol{T}_{isg,dmd} \in \mathbb{R}^{N_p}$ from which the initial $\boldsymbol{k}_I \in \mathbb{R}^{N_p}$ can be obtained using an initial voltage trajectory $\boldsymbol{V}_{init} \in \mathbb{R}^{N_p}$ as the actual voltage. Due to the ISG torque trajectory $\boldsymbol{T}_{isg,dmd} \in \mathbb{R}^{N_p}$, the current trajectory $\boldsymbol{I} \in \mathbb{R}^{N_p}$ by (4.12) affects the battery voltage $\boldsymbol{V}$ which behavior is updated with the implemented battery model (4.17). Based on the determined $\boldsymbol{V}$, a more accurate voltage trajectory $\boldsymbol{V}$ is obtained by updating $\boldsymbol{k}_I$. This iteration is done until the voltage change $\Delta \boldsymbol{V}$ has converged to a small threshold value δ. A small threshold implies that the nonlinear plant behavior is considered in the SoC model.

MPC formulation

The master controller, similar to the slave controller, is based on the augmentation of the obtained SoC model (4.21), (4.22) which follows to the incremental formulation [159]

$$\boldsymbol{x}_m(k+1) = \boldsymbol{A}_m\boldsymbol{x}_m(k) + \boldsymbol{B}_m(k)\Delta u_m(k) + \boldsymbol{E}_m(k)\Delta z_m(k), \tag{4.48}$$

$$\mathrm{SoC}(k) = \boldsymbol{C}_m\boldsymbol{x}_m(k), \tag{4.49}$$

where $\boldsymbol{x}_m(k) = \begin{bmatrix} \Delta\mathrm{SoC}(k) & \mathrm{SoC}(k) \end{bmatrix}^T$ is the augmented state vector, Δu_m is the incremental input and Δz_m is the incremental disturbance. For the optimization, the objective function J_m to be optimized can be formulated by

$$J_m = Q_m \sum_{i=1}^{N_p-1} \left(\mathrm{SoC}_{dmd} - \mathrm{SoC}(k+i)\right)^2 + R_m \sum_{i=0}^{N_c-1} \left(\Delta u_m(k+i)\right)^2$$
$$+ \boldsymbol{x}_m(k+N_p)^T \boldsymbol{P}_m \boldsymbol{x}_m(k+N_p) \quad (4.50)$$

where Q_m, R_m are weights. The weight $\boldsymbol{P}_m$ is calculated by the discrete algebraic Riccati equation

$$\boldsymbol{P}_m = \boldsymbol{A}_m^T \boldsymbol{P}_m \boldsymbol{A}_m - \boldsymbol{K}_m^T \left(\boldsymbol{R}_m + \boldsymbol{B}_m^T \boldsymbol{P}_m \boldsymbol{B}_m\right) \boldsymbol{K}_m + \boldsymbol{C}_m^T Q_m \boldsymbol{C}_m, \tag{4.51}$$

where $\boldsymbol{K}_m = \left(\boldsymbol{R}_m + \boldsymbol{B}_m^T \boldsymbol{P}_m \boldsymbol{B}_m\right)^{-1} \boldsymbol{B}_m^T \boldsymbol{P}_m \boldsymbol{A}_m$. The stacked output prediction $\hat{\boldsymbol{Y}}_m$ follows then to

$$\hat{\boldsymbol{Y}}_m = \begin{bmatrix} \mathrm{SoC}(k+1) & \cdots & \mathrm{SoC}(k+N_p) & \boldsymbol{x}_m(k+N_p)^T \end{bmatrix}^T$$
$$= \boldsymbol{F}_m\boldsymbol{x}_m(k) + \boldsymbol{\Phi}_{m,u}\Delta\boldsymbol{U}_m(k) + \boldsymbol{\Phi}_{m,z}\Delta\boldsymbol{Z}_{CD}(k), \quad (4.52)$$

with

$$\Delta\boldsymbol{U}_m(k) = \begin{bmatrix} \Delta u_m(k+1) & \ldots & \Delta u_m(k+N_c) \end{bmatrix}^T, \tag{4.53}$$

$$\boldsymbol{F}_m = \begin{bmatrix} (\boldsymbol{C}_m\boldsymbol{A}_m)^T & (\boldsymbol{C}_m\boldsymbol{A}_m^2)^T & \cdots & \left(\boldsymbol{C}_m\boldsymbol{A}_m^{N_p-1}\right)^T & \left(\boldsymbol{A}_m^{N_p}\right)^T \end{bmatrix}^T, \tag{4.54}$$

$$\boldsymbol{\Phi}_{m,u} = \begin{bmatrix} \boldsymbol{C}_m\boldsymbol{B}_m(k|1) & \boldsymbol{0} & \ldots & \boldsymbol{0} \\ \boldsymbol{C}_m\sum_{i=1}^{2}\boldsymbol{B}_m(k|i) & \boldsymbol{C}_m\boldsymbol{B}_m(k|1) & \ldots & \boldsymbol{0} \\ \vdots & \vdots & \ddots & \vdots \\ \boldsymbol{C}_m\sum_{i=1}^{N_p-1}\boldsymbol{B}_m(k|i) & \boldsymbol{C}_m\sum_{i=1}^{N_p-2}\boldsymbol{B}_m(k|i) & \ldots & \boldsymbol{0} \\ \sum_{i=1}^{N_p}\boldsymbol{B}_m(k|i) & \sum_{i=1}^{N_p-1}\boldsymbol{B}_m(k|i) & \ldots & \sum_{i=1}^{N_p-N_c}\boldsymbol{B}_m(k|i) \end{bmatrix}, \tag{4.55}$$

$$\boldsymbol{\Phi}_{m,z} = \begin{bmatrix} \boldsymbol{C}_m\boldsymbol{E}_m(k|1) & \boldsymbol{0} & \ldots & \boldsymbol{0} \\ \boldsymbol{C}_m\sum_{i=1}^{2}\boldsymbol{E}_m(k|i) & \boldsymbol{C}_m\boldsymbol{E}_m(k|1) & \ldots & \boldsymbol{0} \\ \vdots & \vdots & \ddots & \vdots \\ \boldsymbol{C}_m\sum_{i=1}^{N_p-1}\boldsymbol{E}_m(k|i) & \boldsymbol{C}_m\sum_{i=1}^{N_p-2}\boldsymbol{E}_m(k|i) & \ldots & \boldsymbol{0} \\ \sum_{i=1}^{N_p}\boldsymbol{E}_m(k|i) & \sum_{i=1}^{N_p-1}\boldsymbol{E}_m(k|i) & \ldots & \boldsymbol{E}_m(k|1) \end{bmatrix}, \tag{4.56}$$

where $(k|i)$ denotes the time step k at prediction step i, $\Delta\boldsymbol{Z}_{CD}$ is the incremental disturbance trajectory obtained by the cycle detection and $\boldsymbol{F}_m$, $\boldsymbol{\Phi}_{m,u}$ and $\boldsymbol{\Phi}_{m,z}$ predicting the states. Due

to the time varying process model (4.21), (4.22), the terms in $\boldsymbol{\Phi}_{m,u}$ and $\boldsymbol{\Phi}_{m,z}$ appear to be sums instead of a multiplication of $\boldsymbol{A}_m$.

In order to provide sufficient dynamics within the master controller, a sampling time of at least $t_{s,m} = 0.25\,\mathrm{s}$ is beneficial, while the used computational capability limits the prediction horizon to $N_p = 100$. Due to this reason, cycle durations up to $250\,\mathrm{s}$ can only be considered by implementing a not equidistant prediction model. Following equation (4.18), which contains the sampling time $t_{s,m} = 0.25\,\mathrm{s}$ of the master controller, $t_{s,m}$ is adapted for the prediction instants. Note that this provides the possibility to achieve dynamic control with a sampling time of $t_{s,m} = 0.25\,\mathrm{s}$, while a wide prediction horizon is covered. The inaccuracy due to the larger sampling intervals towards the end of the prediction horizon may have negligible influence, since the mean discharge – mainly important – is considered. A multiplication factor for each single SS-model can be used to implement the different sampling times of the prediction within the cost function J_m.

Under consideration of the set of constraints (4.34), the formal optimization problem can be denoted by

$$\mathscr{P}(\boldsymbol{x}_m(k)): \quad \Delta \boldsymbol{U}_m^*(\boldsymbol{x}_m(k)) = \arg\min J_m(\boldsymbol{x}_m(k), \Delta \boldsymbol{U}_m), \tag{4.57}$$
$$\text{s.t.} \;\; \mathcal{C}_m: \; \boldsymbol{M}_m \Delta \boldsymbol{U}_m \leq \boldsymbol{\gamma}_m$$
$$\text{with} \quad \boldsymbol{M}_m = \begin{bmatrix} \boldsymbol{M}_{m,\Delta u} \\ \boldsymbol{M}_{m,u} \\ \boldsymbol{M}_{m,y} \end{bmatrix}, \quad \boldsymbol{\gamma}_m = \begin{bmatrix} \boldsymbol{\gamma}_{m,\Delta u} \\ \boldsymbol{\gamma}_{m,u} \\ \boldsymbol{\gamma}_{m,y} \end{bmatrix}$$

referring to rate, input and output constraints, respectively. Similar to the slave controller, the real time optimization is realized using the FMPC algorithm proposed by [161].

Outer iteration loop

As a result, the optimization problem (4.57) provides the incremental trajectory of the ICE torque $\Delta \boldsymbol{U}_m^*$ that minimizes the SoC deviation from SoC_{dmd} at a defined $\boldsymbol{\omega}_{dmd}$. Calculating the demand ICE torque by

$$T_{ice,dmd}(k+i) = T_{ice}(k) + \sum_{l=1}^{i} \Delta u_m^*(l) \tag{4.58}$$

and taking ICE load constraints into consideration, the demand ICE load $\boldsymbol{P}_{ice,dmd}$ can be obtained by

$$P_{ice,dmd}(k) = \omega_{dmd}(k) T_{ice,dmd}(k), \tag{4.59}$$
$$\text{s.t.} \;\; P_{ice,min} \leq P_{ice,dmd}(k) \leq P_{ice,max}.$$

The outer iteration loop is obtained by solving the inner iteration loop as well as the optimization (4.57) anew with the obtained ICE load $\boldsymbol{P}_{ice,dmd}$ until $\Delta \boldsymbol{P}_{ice,dmd}$ is converged to a defined threshold γ or the maximal sampling time is reached. Note that the ICE load represents another nonlinearity of the master controller that is considered due to the iteration loop.

The master controller equals a power controller that is capable of controlling the SoC, speed as well as ICE and ISG torque, if no constraints are violated. Nevertheless, the optimal trajectories can only be achieved if the system is controllable, which is assumed for any load request.

Convergence of the concept

The Banach fixed-point theorem shows convergence for iteration loops, if the Lipschitz condition is fulfilled and the sequence is Cauchy. Using equations (4.12) and (4.17), the inner iteration loop

can be expressed by an implicit equation $\boldsymbol{V} = f_v(\boldsymbol{T}_{isg,dmd}, \boldsymbol{\omega}_{dmd}, \mathrm{SoC}, \vartheta_{batt}, \boldsymbol{V}) = f_v(\zeta, \boldsymbol{V})$. Similarly, with equations (4.11), (4.12), (4.13), (4.18) and (4.19) as well as the MPC, the outer iteration loop is expressed by a function $\boldsymbol{P}_{ice,dmd} = f_p(\boldsymbol{P}_{load}, \mathrm{SoC}, \vartheta_{batt}, \boldsymbol{P}_{ice,dmd}) = f_p(\xi, \boldsymbol{P}_{ice,dmd})$. Both equations are assumed to be feasible in the operation range, since the output voltage $\boldsymbol{V}$ as well as demand ICE load $\boldsymbol{P}_{ice,dmd}$ are bounded by constraints.

The prove for convergence can be done by standard linear MPC literature (c.f. e.g. [48], [68], [156]) and is similar for both iterations as given in the following.

Assumption 1. *Both functions f_v and f_p satisfy the Lipschitz condition such that*

$$|f_v(\zeta, \boldsymbol{V} + \Delta\boldsymbol{V}) - f_v(\zeta, \boldsymbol{V})| \leq L_v\,|\Delta\boldsymbol{V}|, \tag{4.60}$$

$$|f_p(\xi, \boldsymbol{P}_{ice,dmd} + \Delta\boldsymbol{P}_{ice,dmd}) - f_p(\xi, \boldsymbol{P}_{ice,dmd})| \leq L_p\,|\Delta\boldsymbol{P}_{ice,dmd}|, \tag{4.61}$$

with $L_v, L_p > 0$ hold. Therefore, if f_v and f_p are continuous and satisfy (4.60) and (4.61), respectively, it follows that each of f_v and f_p have unique solutions [42].

Denoting $\boldsymbol{X}$ instead of $\boldsymbol{V}$ and $\boldsymbol{P}_{ice,dmd}$, respectively, with Assumption 1 and mathematical induction, Lemma 1 follows:

Lemma 1. *For all $k \in \mathbb{N}_{>0}$, arbitrary $\boldsymbol{X}_0$ and Lipschitz constant $L \in [0, 1)$, $\|\boldsymbol{X}_{k+1} - \boldsymbol{X}_k\|_2 \leq L^k \|\boldsymbol{X}_1 - \boldsymbol{X}_0\|_2$ holds.*

Proof. Proceeding using mathematical induction, the base case holds:

$$\|\boldsymbol{X}_2 - \boldsymbol{X}_1\|_2 = \|f(\boldsymbol{X}_1) - f(\boldsymbol{X}_0)\|_2 \leq L\,\|\boldsymbol{X}_1 - \boldsymbol{X}_0\|_2 \tag{4.62}$$

Then, supposing the statement holds for some $k \in \mathbb{N}_{>0}$, the induction hypothesis follows to

$$\|f(\boldsymbol{X}_{k+1}) - f(\boldsymbol{X}_k)\|_2 \leq L\,\|\boldsymbol{X}_{k+1} - \boldsymbol{X}_k\|_2 \tag{4.63}$$

$$\leq L L^k \|\boldsymbol{X}_1 - \boldsymbol{X}_0\|_2 \tag{4.64}$$

$$= L^{k+1} \|\boldsymbol{X}_1 - \boldsymbol{X}_0\|_2, \tag{4.65}$$

which proves the Lemma by the principle of mathematical induction [48]. $\qquad\square$

Based on Lemma 1, the sequence can be shown to be Cauchy.

Lemma 2. *Let $M \in \mathbb{R}^{N_p}$ be a metric space. The sequence $\{\boldsymbol{X}_k\}$ in M is a Cauchy sequence and therefore converges with a Lipschitz constant $L \in [0, 1)$ to a limit $\boldsymbol{X}^*$ in M [68].*

Proof. Let $m, n \in \mathbb{N}_{>0}$ such that $m > n$. Using the Triangle Inequality, Lemma 1 and the Geometric Series, the following can be denoted:

$$\|\boldsymbol{X}_m - \boldsymbol{X}_n\|_2 \leq \|\boldsymbol{X}_m - \boldsymbol{X}_{m-1}\|_2 + \cdots + \|\boldsymbol{X}_{n+1} - \boldsymbol{X}_n\|_2 \tag{4.66}$$

$$\leq L^n \|\boldsymbol{X}_1 - \boldsymbol{X}_0\|_2 \sum_{k=0}^{m-n-1} L^k \tag{4.67}$$

$$\leq L^n \|\boldsymbol{X}_1 - \boldsymbol{X}_0\|_2 \sum_{k=0}^{\infty} L^k \tag{4.68}$$

$$= L^n \|\boldsymbol{X}_1 - \boldsymbol{X}_0\|_2 \left(\frac{1}{1-L}\right). \tag{4.69}$$

Let $\varepsilon > 0$ arbitrary, a large $N \in \mathbb{N}_{>0}$ can be found such that

$$L^N < \frac{\varepsilon\,(1-L)}{\|\boldsymbol{X}_1 - \boldsymbol{X}_0\|_2} \tag{4.70}$$

is satisfied, and

$$\|\boldsymbol{X}_m - \boldsymbol{X}_n\|_2 \leq L^n \|\boldsymbol{X}_1 - \boldsymbol{X}_0\|_2 \left(\frac{1}{1-L}\right) < \varepsilon \tag{4.71}$$

follows for m, n large enough. Since $\varepsilon > 0$ is arbitrary, the sequence is proven to be Cauchy. $\quad\square$

Using Assumption 1, Lemmas 1 and 2, Theorem 1 follows:

Theorem 1 (Banach Fixed-Point Theorem [6])**.** *A map* $f : M \to M$ *is called contraction mapping on* M *if there exists a Lipschitz constant* $L \in [0, 1)$ *such that*

$$\|f(\boldsymbol{X}_{k+1}) - f(\boldsymbol{X}_k)\|_2 \leq L \|\boldsymbol{X}_{k+1} - \boldsymbol{X}_k\|_2, \ \forall k \in \mathbb{N}_{>0} \tag{4.72}$$

with $\boldsymbol{X}_k = f(\boldsymbol{X}_{k-1})$. *If*

$$L^N < \frac{\varepsilon(1-L)}{\|\boldsymbol{X}_1 - \boldsymbol{X}_0\|_2}, \quad \varepsilon > 0, \tag{4.73}$$

is satisfied for a large $N \in \mathbb{N}_{>0}$, *the following inequalities hold:*

$$\frac{\|\boldsymbol{X}_{k+1} - \boldsymbol{X}_k\|_2}{\|\boldsymbol{X}_1 - \boldsymbol{X}_0\|_2} \leq L^k < \frac{\|\boldsymbol{X}_2 - \boldsymbol{X}_1\|_2}{\|\boldsymbol{X}_1 - \boldsymbol{X}_0\|_2} < 1. \tag{4.74}$$

Theorem 1 is fulfilled if $\exists L \in [0, 1)$, which is shown for both iteration loops in the following.

Convergence of iteration loops   Based on Theorem 1, $0 \leq L < 1$ can be shown for both iteration loops separately by evaluating the closed set of possible configurations. Both iterations converged to the true value $\boldsymbol{V}^*$ (see Figure 4.6) and $\boldsymbol{P}^*_{ice,dmd}$ (see Figure 4.7), respectively.
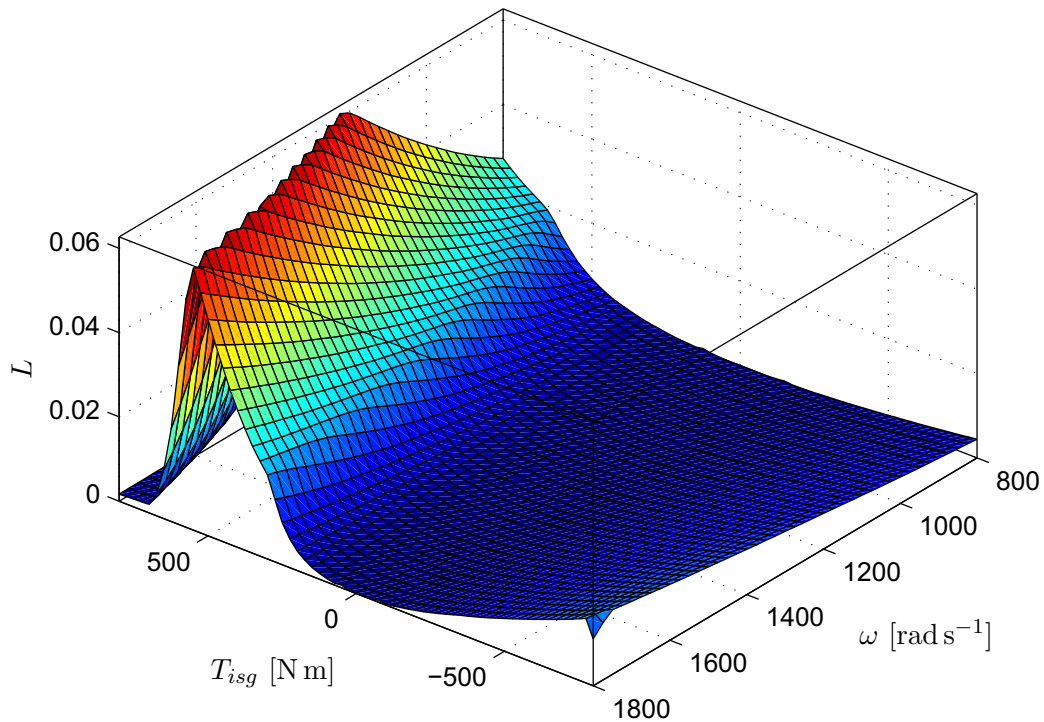
Figure 4.6: Contraction map of the inner iteration loop showing that L exists and $0 \leq L < 1$ for all possible configurations.

4.4   Load and cycle prediction for non-road machinery

The driver exclusively influences the load trajectory and driving patterns of non-road machinery [38]. Exact prediction of future load demands is in general very difficult or sometimes impossible. Nevertheless, in the following, two statistical approaches are introduced, which are able to predict
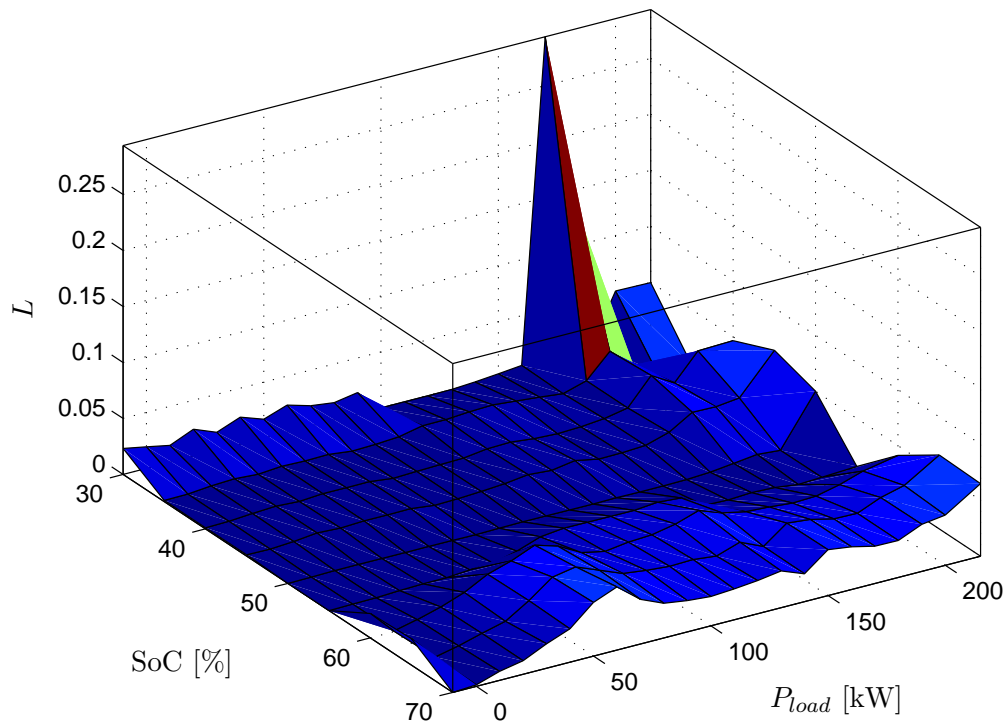
Figure 4.7: Contraction map of the outer iteration loop showing that L exists and $0 \leq L < 1$ for all possible configurations.

the future load trajectories with sufficient accuracy for the usage in non-road vehicles. A short term load trajectory $\boldsymbol{Z}_{LP}$ for use in the slave MPC and a long term cycle prediction $\boldsymbol{Z}_{CD}$ for use in the master MPC are proposed in detail. The cycle prediction is based on a cycle detection that is similar to the approach proposed by [101].

4.4.1 Short term load prediction

The idea of the short term load prediction is to detect critical load demands of e.g. wheel loaders at digging or at reversion, in order to permit a control action in advance (e.g. increasing the rotational speed in advance to a load peak acting on the powertrain). For example, at reversion of the vehicle, if the load requirement is especially high shortly after direction change and vehicle acceleration, the load prediction offers the possibility to avoid engine stalling or a speed undershoot. Driveability and handling capacity may be increased, which is especially of interest for the industry. In the following the theory of Bayesian inference is shortly reviewed before the methodology is discussed in detail. Based on the wheel loader the accuracy of the methodology is validated based on real data measured on a real wheel loader.

Bayesian inference

In the field of mathematical statistics, the Bayesian inference (BI) is an important technique to update a probability of a hypothesis (H) as new evidence (E) is available. Especially for dynamic data sequence analysis, the BI has a decisive role. Based on Bayes' rule, the posterior probability is calculated using the a prior probability and the likelihood function, respectively. The latter two can be obtained from a probability model describing the data to be observed.

The posterior probability is calculated using Bayes' theorem (4.75)

$$P(H \mid E) = \frac{P(E \mid H) \cdot P(H)}{P(E)}, \tag{4.75}$$

where | denotes a conditional probability, $P(H)$ and $P(H \mid E)$ are prior and posterior probability, respectively, $P(E)$ is the likelihood function and $P(E \mid H)$ is the conditional probability of observing evidence E if hypothesis H is given. Note here that the posterior probability is proportional to $P(H)$ and $P(E \mid H)$, since these values appear in the numerator of equation (4.75). Using the theory of Bayesian inference, the load prediction methodology can be developed.

Methodology of load prediction

The actual vehicle inputs u_i, such as accelerator angle α, driving speed n_{GW} and load P_{load} offer the only information about the vehicle state that can be used to predict the future load demand. In case of a specific input state configuration, a probability can be calculated that provide statistical evidence about the future load demand depending on the actual vehicle state. For that purpose, inputs and outputs are assigned to discrete classes ϕ_{ij} in the possible input/output range in order to be able to apply the theory of the discrete Bayesian inference. Based on Bayes' rule, the a posteriori probability for a certain load class ψ_{1j} given a certain input configuration $\underline{\Phi}(k)$ can be calculated. A priori probability and the likelihood function are required [99] and can be obtained from training data [16]. Note that the accuracy is directly dependent on the training data and therefore all relevant information needs to be included in the training data. Determining the a priori probability and the likelihood function based on training data shifted backwards in time, the basis to calculate the a posteriori probabilities $P(\psi_{hj}|\underline{\Phi})$ for further prediction steps h is given. Exemplarily, the methodology is depicted in Figure 4.8 and the rule of Bayes to calculate $P(\psi_{hj}|\underline{\Phi})$ is given.

Prediction of the future load demand

Since a load trajectory is required by the controllers, the probabilities $P(\psi_{hj}|\underline{\Phi})$ need to be converted into a load value. A simple approach to extract the load value is to choose the highest load class probability $\max(P(\psi_{hj}|\underline{\Phi}))$ and use the corresponding maximum load value associated by the class for each prediction step h. Note that in case of large load classes, the resolution is rough and the prediction may have insufficient accuracy. This can be avoided by choosing enough output classes or an average class load value. The short term load trajectory $\boldsymbol{Z}_{LP}$ (green stair function) follows therefore by storing the corresponding load value $z_{LP,h}$ of the class in a vector

$$\boldsymbol{Z}_{LP} = \begin{bmatrix} z_{LP,1} \cdots z_{LP,n_p} \end{bmatrix}^T. \tag{4.76}$$

The incremental notation required by the MPC follows by

$$\Delta \boldsymbol{Z}_{LP} = \begin{bmatrix} \Delta z_{LP}(1) \cdots \Delta z_{LP}(n_p) \end{bmatrix}^T, \tag{4.77}$$

$$\text{with} \quad \Delta z_{LP}(i) = \begin{cases} z_{LP,1} - P_{load}(k) & \text{if } i = 1 \\ z_{LP,i} - z_{LP,i-1} & \text{else} \end{cases}.$$

Validation of the load prediction

For validation of the load prediction, training data were recorded on a corresponding wheel loader at operation for an eight hour duration. An analysis showed the following input configuration $\underline{u}$ to be significant for the load prediction

$$\underline{u} = \begin{bmatrix} \alpha & |n_{GW}| & P_{load} & \Delta^2\left(\text{filt}\left(P_{load}\right)\right) \end{bmatrix}, \tag{4.78}$$
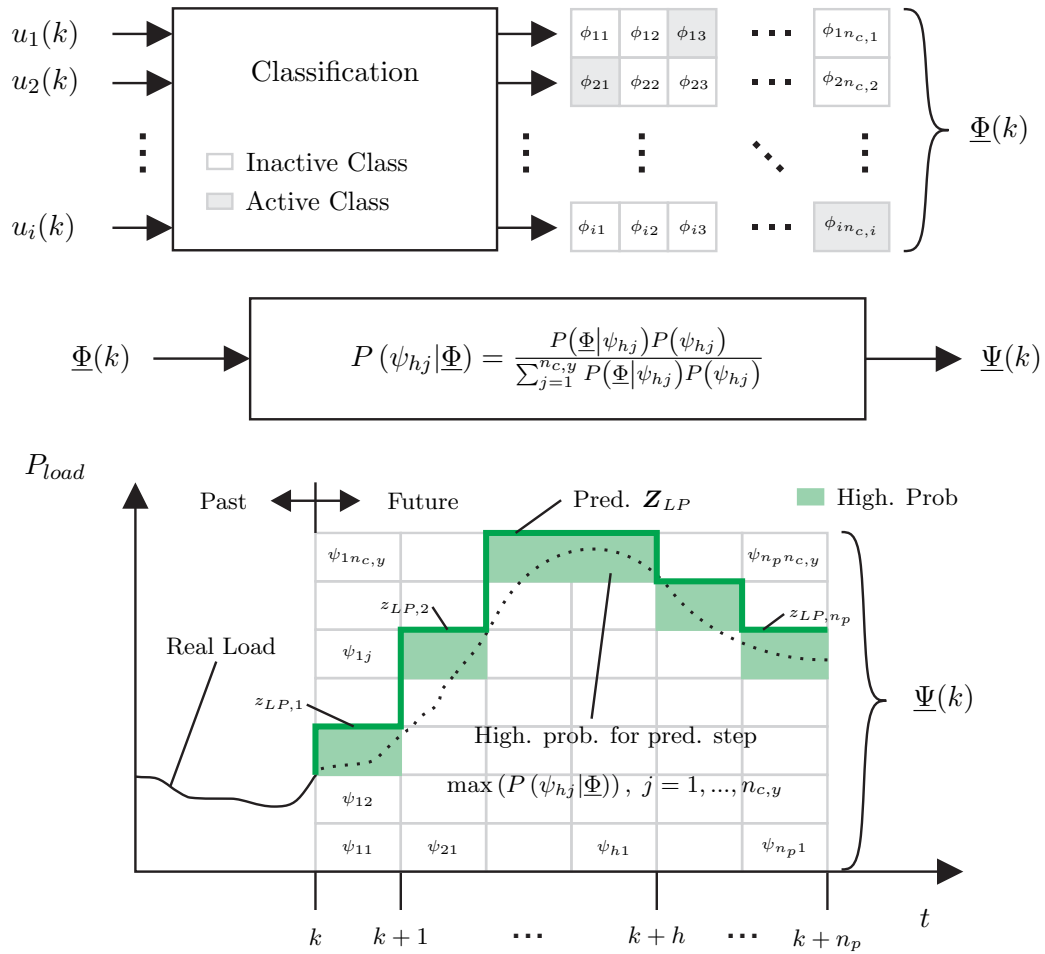
Figure 4.8: Load prediction methodology.

where Δ^2 denotes the dual backwards difference operator and filt() is a low pass filter. The selection includes the driver information (α), an indication for the overall power consumption ($|n_{GW}|$) and the actual state of the vehicle ($P_{load}, \Delta^2 \left(\text{filt}\left(P_{load}\right)\right)$). Note that the filter input corresponds to the mechanical inertia and needs to be tuned in such a way that strong gradients are not too much delayed, but that noise and small load peaks are avoided. A selection of 6 input classes $n_{c,i}$ for α, 4 for $|n_{GW}|$, 24 for P_{load} and 6 for the filter input showed to be adequate, while 24 output classes $n_{c,y}$ have been chosen to achieve sufficient resolution for the load prediction.

Figure 4.9 shows the input signals (blue) corresponding to the measured load signal (red) and the predicted short term load trajectories across a horizon of $n_p = 25$ samples (gray). The load sequence is previously unknown by the load prediction, but though, accurate predictions are achieved at increasing load gradients (c.f. around second 2 and 9). This is plausible since accelerator position, filter input and driving speed indicate a clear load demand. The largest part of the overall load is in general consumed by the drivetrain. Around second 6, the driving speed is increasing although the accelerator position is around 60% and decreases. At this point, a serious indication is impossible since not even the filter input can provide an additional indication and therefore the actual load is in principle predicted.

Between second 7 and 8 negative loads appear, which are not critical to engine stalling. A significant prediction mismatch results from a low resolution obtained by the simplification of assigning only one load class for the entire negative load range. Note that an increase in the number of output load classes would enhance the prediction accuracy in the negative load range.

4.4.2 Cycle detection

Dockside cranes or wheel loaders are mostly used in cyclical operations, which yield recurrent load demands that can be used to predict the future cycles. The goal is to predict the load trajectory by detecting a recurrent load cycle $\boldsymbol{z}_{cyc} \in \mathbb{R}^{s_{cyc}}$ within the past load signal and to provide a disturbance trajectory $\boldsymbol{Z}_{CD} = \left[\boldsymbol{z}_{cyc}^T \cdots \boldsymbol{z}_{cyc}^T\right]^T \in \mathbb{R}^{N_p}$ with sampling time $t_{s,m}$ for the master controller based on the obtained cycle information. Correlation analysis provides the necessary theory to find the recurrent cycles within the past load signal. In the following, the theory of correlation analysis is therefore reviewed before the methodology of the cycle detection is presented in detail. Based on a real load signal obtained from a wheel loader, the methodology is validated to show the possibilities.

Cross correlation function

Commonly in signal processing, tasks consist of finding short signals within a long signal. A measure for the similarity of two signals is given by the cross correlation, which has applications over all natural sciences. It is used in e.g. pattern recognition, single particle analysis, electron tomography, averaging, cryptanalysis, or neurophysiology. In terms of statistical analysis, the term cross correlation refers to the correlation between the values of two random vectors $\boldsymbol{x}$ and $\boldsymbol{y}$, while a special case is the correlation of the values of one vector $\boldsymbol{x}$ with itself, which is referred to as auto correlation (ACF). The cross correlation function is defined by

$$\hat{R}_{xy}(l) = \sigma \sum_{k=1}^{N} x(k)\, y(k-l), \tag{4.79}$$

where x, y are the entries of the vectors $\boldsymbol{x}$ and $\boldsymbol{y}$ respectively, N is the signal length and σ is a scaling factor. Note here that in the field of statistical analysis, the scaling factor σ is usually included in the definition in order to obtain correlations between -1 and $+1$. Based on the cross correlation function, the methodology of the cycle detection can be developed in the following.
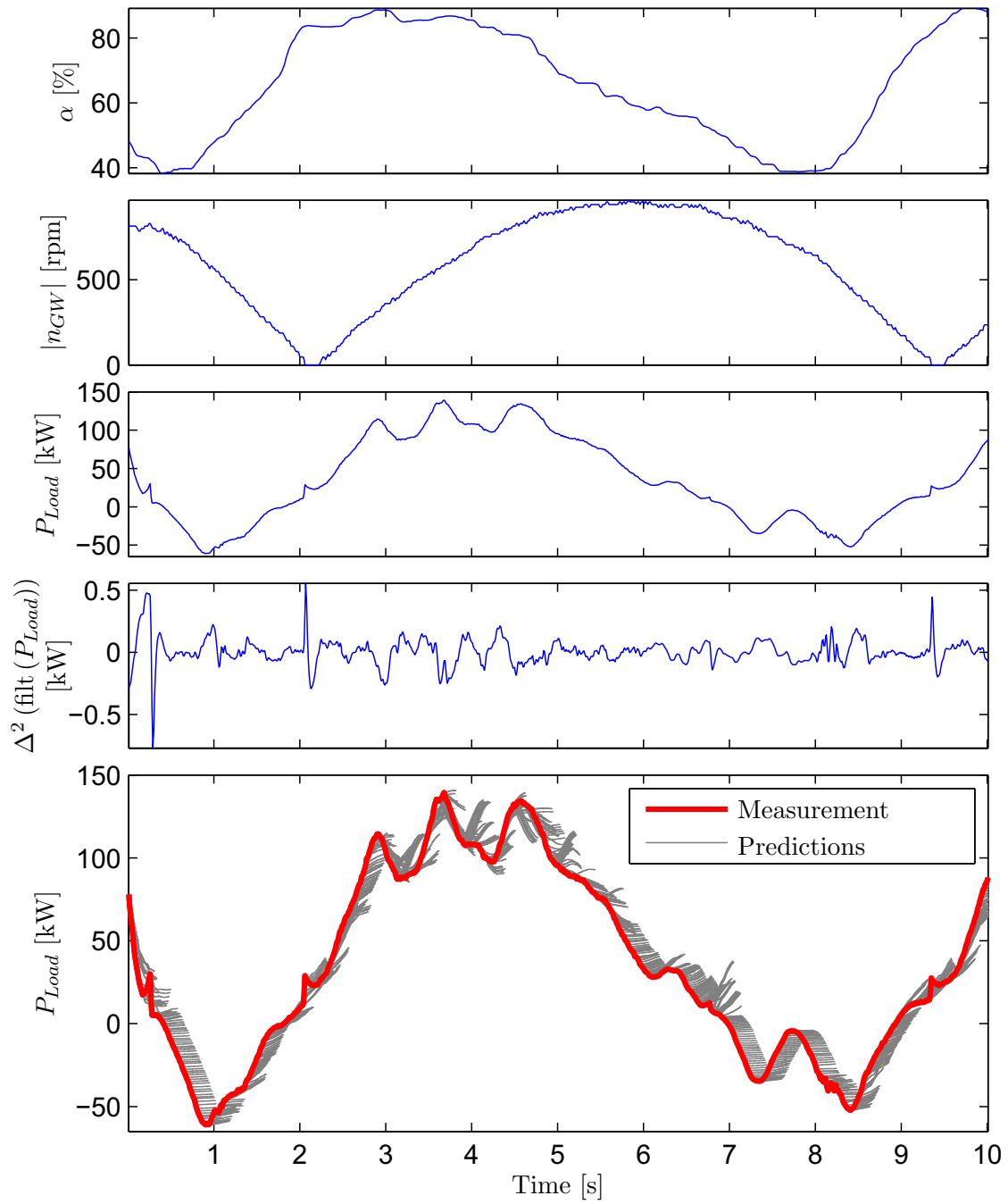
Figure 4.9: Predictions (gray lines) achieved for the measured load (red) at given actual inputs (blue).

Identification methodology for recurrent load cycles

Mayr et al. [101] proposed an algorithm to detect the cycle duration $t_{cyc} = s_{cyc}t_{s,m}$ of a recurrent load cycle within the past load signal $\boldsymbol{y}_{CD} \in \mathbb{R}^{\geq 2 \cdot s_{cyc}}$ based on the auto correlation function. The first local maximum in the ACF is used to identify the cycle. One disadvantage of the ACF is that in case of a changing load cycle, a detection of the cycle with an acceptable time delay is difficult. In case of cycles with significantly different cycle times, the shape of the first local maximum is not formed clearly, which makes a secure detection impossible.

In this work, the cross correlation function $\hat{R}_{xy,i}$ between $\boldsymbol{y}_{CD}$ and different parts $\boldsymbol{x}_{CD,i}$, $i = 1, 2, 3, \ldots$, which are systematically taken from $\boldsymbol{y}_{CD}$, is used to adapt the ACF approach in order to avoid this disadvantage. The size of the parts $\boldsymbol{x}_{CD,i}$ are within the scope of the possible cycle durations within $\boldsymbol{y}_{CD}$ due to which reason a cycle change can be detected sufficiently fast. A cycle is detected and included in $\boldsymbol{y}_{CD}$ if more than two local maxima of $\hat{R}_{xy,i}$ lie within a small range around $\hat{R}_{xy,i} = 1$ and the distance between the local maxima defines the corresponding cycle time.

Once a cycle is detected, the past s_{cyc} load values form the load cycle $\boldsymbol{z}_{cyc}$, which is used to built the incremental notation of the future load trajectory $\boldsymbol{Z}_{CD}$ used in the master controller by

$$\Delta \boldsymbol{Z}_{CD}(k) = \begin{bmatrix} \Delta z_{CD}(1) \cdots \Delta z_{CD}(N_p) \end{bmatrix}^T, \tag{4.80}$$

$$\text{with} \quad \Delta z_{CD}(i) = \begin{cases} Z_{CD}(i) - P_{load}(k) & \text{if } i = 1 \\ Z_{CD}(i) - Z_{CD}(i-1) & \text{else} \end{cases}.$$

Validation of the methodology

A more sophisticated representation of the methodology is depicted in Figure 4.10, where the cycle detection is demonstrated on real load measurement from a wheel loader. The measured signal (blue), the past load trajectory $\boldsymbol{y}_{CD}$ (red) and the predicted disturbance trajectory $\boldsymbol{Z}_{CD}$ (green) are drawn in the first subplot, while the true (blue) with the detected (red) cycle time t_{cyc} are given in the second subplot. It can be seen that almost 3 cycles are required to detect the cycle change, which is sufficiently fast since a confident prediction needs at least 3 occurred cycles. Note that, though, the new cycle is only a short part of $\boldsymbol{y}_{CD}$, the cycle time can be detected correctly.

Below the first two subplots, the past load signal $\boldsymbol{y}_{CD}$ (red) and the different parts $\boldsymbol{x}_{CD,i}$ (cyan) are depicted on the left side, while the corresponding CCF $\hat{R}_{xy,i}$ (blue) between $\boldsymbol{x}_{CD,i}$ and $\boldsymbol{y}_{CD}$ is shown on the right side. The blue points indicate that the local maxima lie inside the thresholds (green dashed lines) and match for the different $\hat{R}_{xy,i}$. Consequential, a cycle is detected.
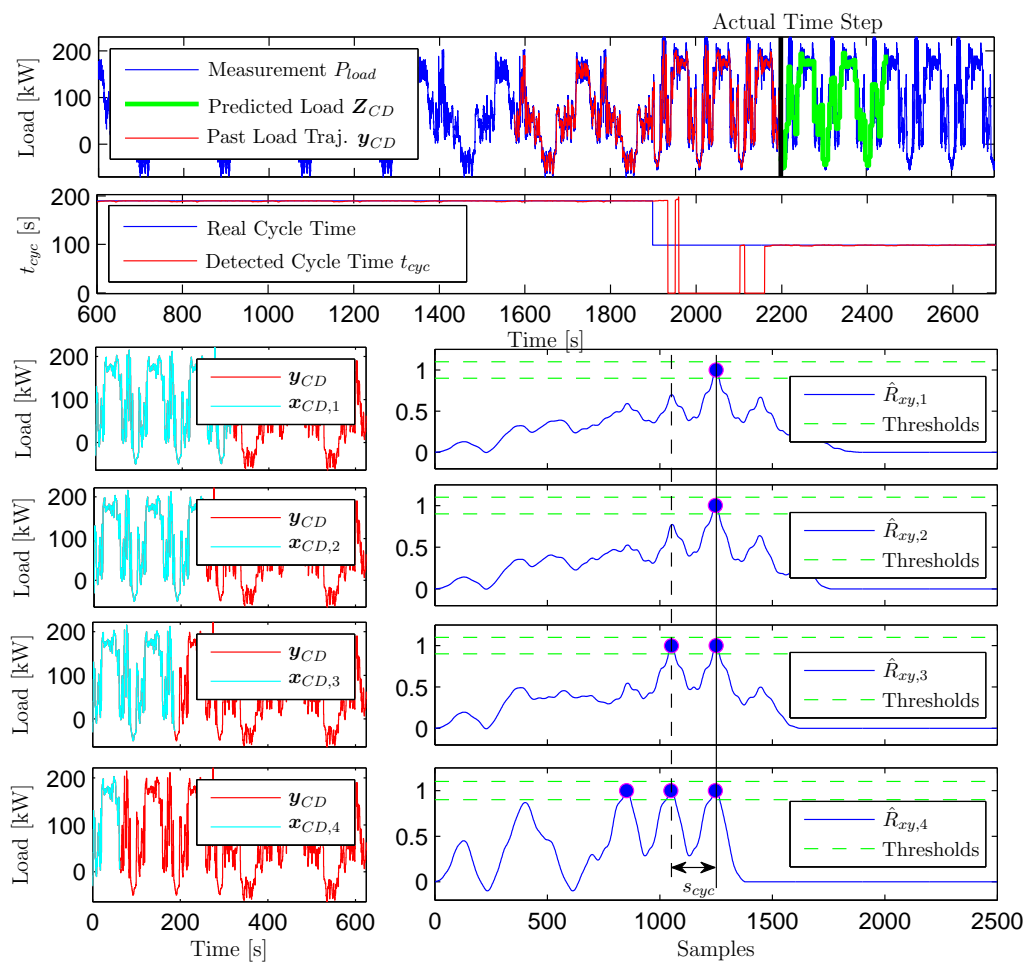
Figure 4.10: Cycle detection demonstrated on a real load cycle change.

Chapter 5

Application Example: Wheel Loader

The chapters 2, 3 and 4 discussed the methodologies to estimate the battery SoC with high accuracy as well as to control a parallel hybrid electric powertrain in non-road vehicles. In this chapter, the results obtained by these methodologies should be presented. First, the hardware of the used real powertrain and testbed including a battery simulator, respectively, are described. Second, simulation and real measurement results are presented in terms of dynamics, overall optimality and efficiency improvement due to the proposed EMS.

5.1 Hardware configuration of the hybrid powertrain testbed

Non-road vehicles are usually equipped with more powerful engines than they are registered with, which in this context means that they are restricted in power. At the testbed a real diesel electrical parallel hybrid powertrain comprising of a $290\,\mathrm{kW}$ ICE (limited at $P_{ice,max} = 215\,\mathrm{kW}$) and a $120\,\mathrm{kW}$ ISG, is set up. A torque sensing shaft connects the testbed dyno with the powertrain in order to apply the load. Instead of a real battery, a battery simulator supplies the required power for the ISG where an accurate LMN battery model of the lithium-iron-phosphate chemistry based battery module with $630\,\mathrm{V}$ nominal voltage and $\pm200\,\mathrm{A}$ maximal current (192 series and 2 parallel connected cells (192S2P) configuration) is implemented (see Section 3.6). Note that the powertrain is also modeled and used for real time simulation.

A dSpace DS1006 platform is used to control the testbed measurements as well as real time simulations. The platform runs the standard fixed step-size solver for which the controller is compiled, while the optimization problem is solved using the primal barrier interior-point method in the FMPC algorithm proposed by [161]. Further details on algorithm and computation times can be found in [161] and e.g. [126], [169]. The proposed controller can be parametrized by the number of iterations in the FMPC, which are properly chosen to $n_{iter,FMPC,slave} = 10$ and $n_{iter,FMPC,master} = 3$, respectively, the number of inner ($n_{iter,inner} = 10$) and outer ($n_{iter,outer} = 3$) iteration loops of the master controller and the prediction horizons for both MPCs in order to achieve lower computation times. Based on the given selections, the runtime limit of the platform is fully exploited, but is not exceeded. Relevant information between platform and supervisory testbed control system is exchanged with a CAN interface, while a sampling time of $t_{s,s} = 10\,\mathrm{ms}$ is used for the interface as well as for all measurements. Figure 5.1 shows a picture of the testbed application.

5.2 Energy management in wheel loaders

The feasibility of the control concept is validated by carrying out real testbed measurements using the real powertrain described previously. Important to show is that the controller is able to
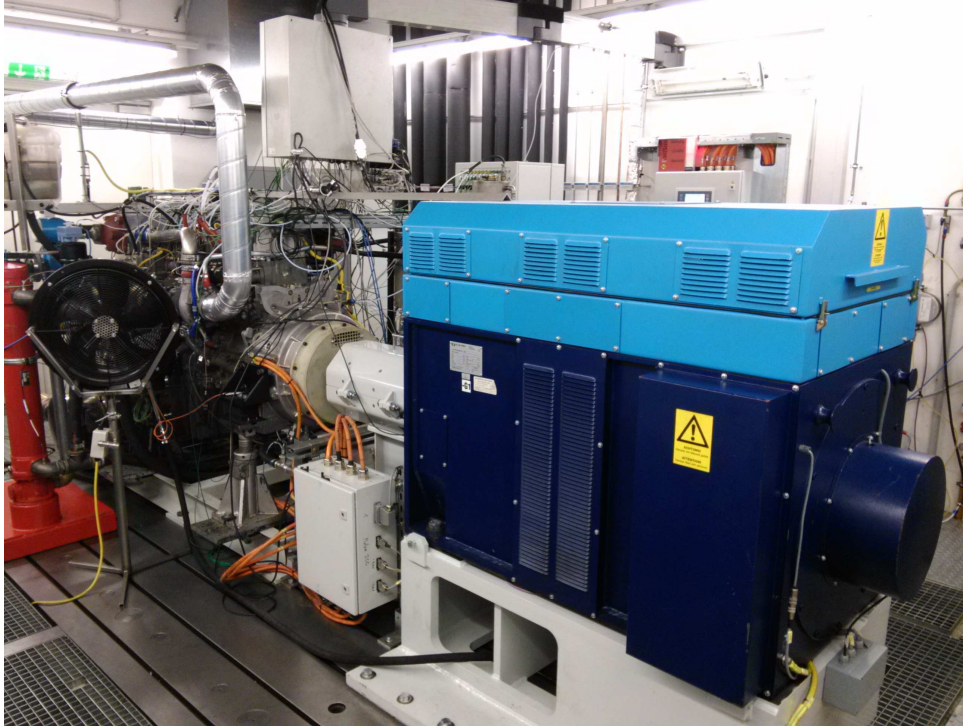
Figure 5.1: Parallel hybrid electric powertrain at the testbed.

cope with the high dynamic load transients appearing in non-road applications, while emissions and fuel consumption are reduced simultaneously. A critical point of the control is, if constraints are active. For the purpose of reasonable results, the controller is tuned based on simulations, before testbed measurements are carried out. In the following, the controller penalties are discussed before the simulations are presented and measurement results are discussed.

5.2.1   User-defined tuning of the controller penalties

The selection of the penalties used in the optimization problems $\mathscr{P}_s(\boldsymbol{x}_s(k))$ and $\mathscr{P}_m(\boldsymbol{x}_m(k))$, is referred to as tuning and influences the behavior of the controller. In order to achieve maximal efficiency of the powertrain, the electrical energy conversion (EEC) must be kept at a minimum, since efficiency and EEC are directly linked by the conservation of energy principle. To this end, the penalties need to be set in such a way that dynamic requirements of the powertrain are provided in any case and the EEC is minimized simultaneously.

The SoC deviation from the demand SoC has direct influence on the EEC and can be penalized with the state penalty Q_m. By choosing $Q_m = 0.1$ (*more EEC*) and $Q_m = 10$ (*less EEC*), the influence of the SoC deviation can be seen and compared. In terms of dynamic and a good speed controlling performance, the state penalty Q_s plays a major role and is therefore chosen significantly higher than the control $\boldsymbol{R}_s$ and input $\tilde{\boldsymbol{R}}_s$ penalties. Desirable is also a smooth dynamic behavior of the ICE, since strong torque gradients cause higher emissions. This is achieved by penalizing the ICE torque increments more than the ISG torque increments. Note that this is inconsistent with the required dynamics, but due to the optimization, solved in an optimal manner. In contrast to the slave dynamics, the master controller has inferior influence on the fast control dynamics, due to which the control penalty R_m is chosen appropriately small. The used parameters of the model and controller, respectively, are summarized in Table 5.1 to give a better overview.

Parameter	Nominal value	Description
$t_{s,s}$	$0.01\,\mathrm{s}$	sampling time slave
$t_{s,m}$	$0.25\,\mathrm{s}$	sampling time master
$N_p = N_c$	100	prediction horizon master
Q_m	0.1, 10	state penalties master
R_m	0.01	control penalty master
$n_p = n_c$	25	prediction horizon slave
Q_s	100	state penalty slave
$\boldsymbol{R}_s$	$\mathrm{diag}[10 \quad 2]$	control penalties slave
$\tilde{\boldsymbol{R}}_s$	$\mathrm{diag}[0.5 \quad 1]$	input penalties slave
$\omega_{min} \ldots \omega_{max}$	$1000 \ldots 2000\,\mathrm{rpm}$	speed range
$\mathrm{SoC}_{min} \ldots \mathrm{SoC}_{max}$	$20 \ldots 80\,\%$	state of charge range
$I_{min} \ldots I_{max}$	$-200 \ldots 200\,\mathrm{A}$	current range
$V_{min} \ldots V_{max}$	$550 \ldots 700\,\mathrm{V}$	voltage range
$P_{ice,max}$	$215\,\mathrm{kW}$	maximal ICE load limit
$Q_{c,batt}$	$8.8\,\mathrm{A\,h}$	battery capacity
Θ	$10\,\mathrm{kg\,m^2}$	total moment of inertia
τ_{ice}	$0.1\,\mathrm{s}$	ICE model time constant
τ_{isg}	$0.05\,\mathrm{s}$	ISG model time constant

Table 5.1: Used user-defined controller and simulation model parameters.

5.2.2 Simulation results

The simulations are executed on the real time platform, where a real time model of the powertrain is implemented. Main interest of the simulations is to validate the controller tuning in terms of the optimality of the controller set points, while a ICE torque gradient restriction of $\Delta T_{ice,max} = 1000\,\mathrm{Nm/s}$ is applied to limit the ICE dynamics.

Based on the dimensionless energetic efficiency map η_{ice}, in Figure 5.2, the simulation results are compared with a real load cycle of a conventional operated powertrain (black $\times$). The results of the hybrid powertrain are inserted for the hybrid strategies with small (red, $Q_m = 0.1$) and large (blue, $Q_m = 10$) state penalty in order to see the difference between the strategies. As can be seen, the distribution of the operation points is limited to the optimal characteristic line (green) with the lowest specific fuel consumption for $Q_m = 0.1$, while for $Q_m = 10$ an increased distribution is obtained due to the increased usage of the ICE to compensate the transient load.

Compared to the conventional powertrain, a significant decrease of the mean speed is observable due to the optimal operation set points, which proves that the downspeeding strategy is considered directly as proposed. The outliers at $\omega \approx 1250\,\mathrm{rpm}$ and $T_{ice} \approx 700\,\mathrm{N\,m}$ are caused by the driver request $\omega_{min,driver}$.

5.2.3 Experimental results

The experimental results focus mainly on the three following critical points and are presented in detail in the following:

1. Dynamic feasibility under consideration of all relevant constraints of the powertrain and hybrid strategies such as downspeeding and phlegmatisation.

2. Reduction of exhaust emissions and fuel consumption compared to the conventional powertrain due to optimal control.
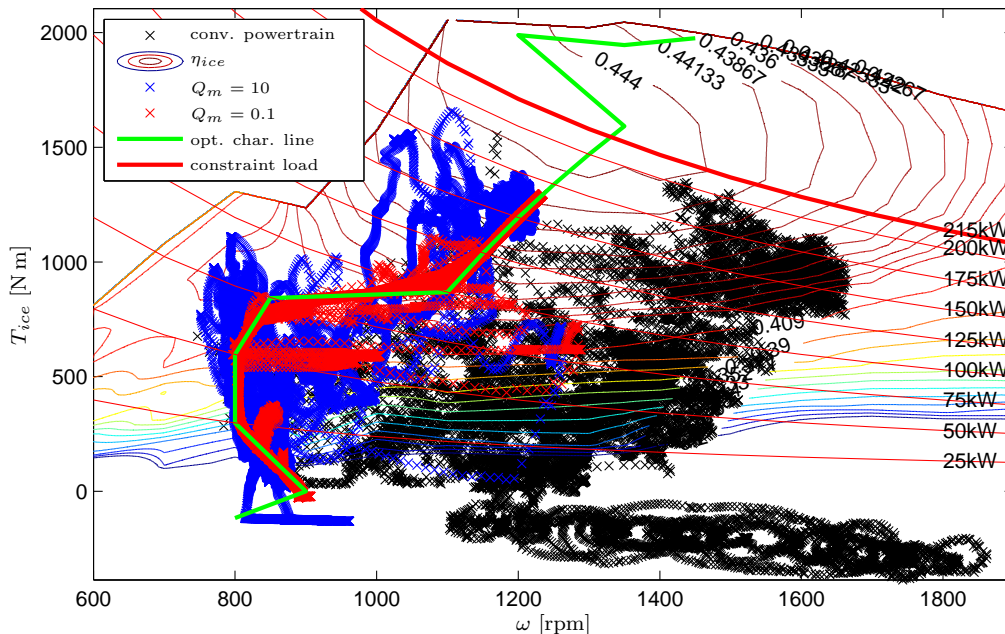
Figure 5.2: Simulated operating points depicted on the dimensionless energetic efficiency map η_{ice}.

3. The benefit of a full exploitation of the energy storage capabilities by use of the cycle detection.

Dynamic feasibility

Phlegmatisation incises the dynamics of the powertrain drastically, especially at an optimal (low) rotational speed, but provides a large potential to reduce exhaust emissions significantly [110]. The feasibility depends mainly to the phlegmatisation rate though. On the testbed, different phlegmatisation rates between $\Delta T_{ice,max}$ between $500\,\mathrm{Nm/s}$ and $5000\,\mathrm{Nm/s}$ are measured, while a rate of $500\,\mathrm{Nm/s}$ showed a significant emission reduction. Nevertheless, cycles with higher load gradients may not be feasible using $500\,\mathrm{Nm/s}$ and therefore a time variant phlegmatisation rate is applied to the powertrain: In general, the ICE torque is limited by $\Delta T_{ice,max} = 500\,\mathrm{Nm/s}$, but after an active constraint for the past 15 samples, it is relaxed to $\Delta T_{ice,max} = 1500\,\mathrm{Nm/s}$. Note that an effective maximum of $1350\,\mathrm{Nm/s}$ is reachable, which is an appreciable limitation. Furthermore, the load prediction is used to avoid engine stalling on high load peaks and to provide sufficient engine dynamics. The influence of the load prediction on the reduced dynamics of the ICE is presented in Figure 5.3.

The first subplot of Figure 5.3 shows the rotational speed trajectories of the actual speed ω and the speed set point ω_{set} for enabled (subscript LP) and disabled load prediction. Enlargement (c) shows that in case of an enabled LP, ω_{set} is raised prior to the load peak and engine stalling occurs for disabled LP due to insufficient ICE dynamics, which can be observed in marked region (a).

The time variant phlegmatisation rate is observable in the second subplot (see marked region (b)), where the trajectories of the ICE torques are depicted. Region (b) shows furthermore that $T_{ice,LP}$ is increased prior to a load peak, due to which engine stalling is avoided. The missing constraints for the driveability limit of the ICE are observable at higher torque levels, where a large mismatch occurs. Prior to the testruns, driveability limit information was not available and could not be considered. Nevertheless, the structured constraints as introduced in Section
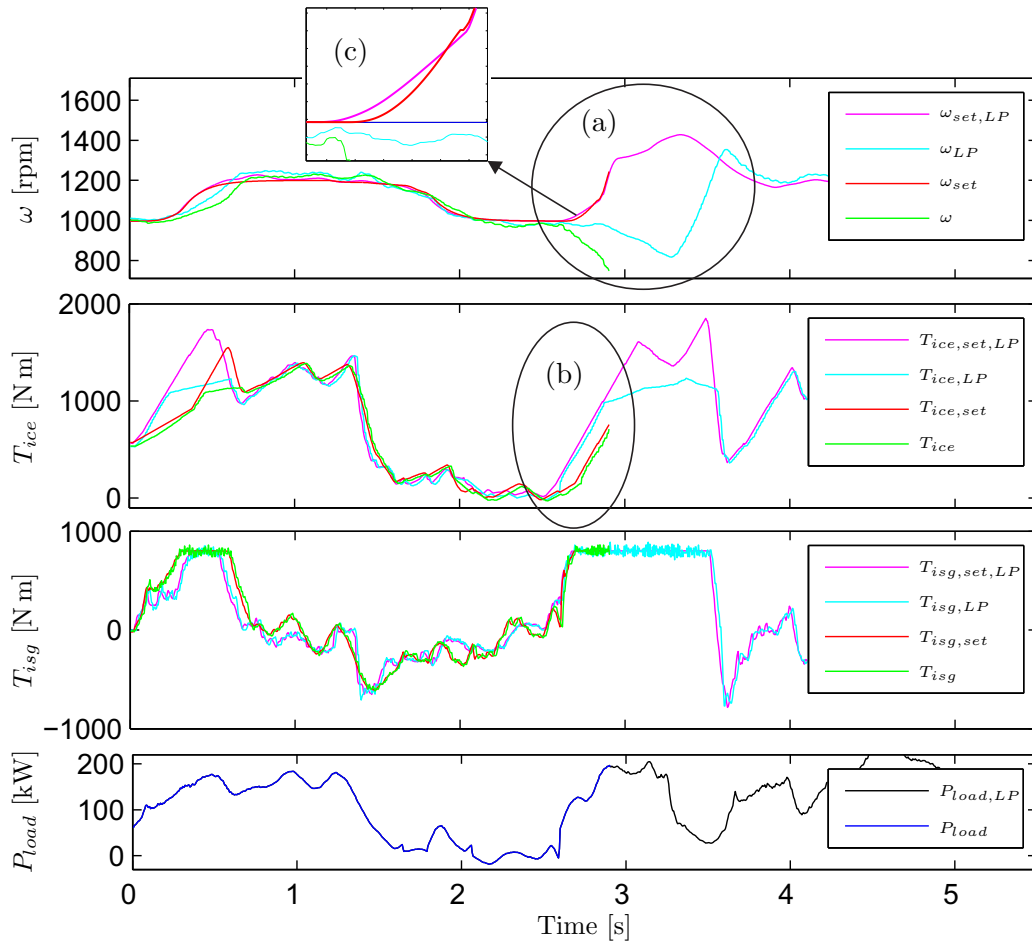
Figure 5.3: Difference between enabled (subscript LP) and disabled load prediction. Engine stalling in case of disabled load prediction.

4.3.3 provide to integrate any additional limits easily.

The ISG torque signals are shown in the third subplot, where can be observed that in terms of dynamics, the load prediction smooths T_{isg} as well as reduces the dynamics of the signal in general. In the last subplot, the load P_{load} is depicted, which matches for enabled as well as disabled LP. Note that in order to avoid engine stalling with disabled LP, the speed must be increased, which also increases the fuel consumption due to friction losses. Hence, the load prediction enables to further reduce fuel consumption although the load demand is unknown and ICE dynamics are restricted.

Fuel consumption and exhaust emissions

In order to achieve a suitable comparison between the hybrid and conventional powertrain, real load cycles are measured at the testbed with the same experimental setup. For that purpose, four representative real load cycles are extracted from a large data set of field measurements obtained from common wheel loaders representing common applications. In Table 5.2, more details about the cycles are summarized, which testbed measurements are used for comparison of fuel consumption and raw exhaust emissions.

Cycle	Duration	Mean Load	Mean Speed
	s	kW	rpm
1	38.48	70.1	1236
2	54.15	61.3	1215
3	189.84	58.4	1360
4	90.44	66.5	1277

Table 5.2: Specifications of the four representative load cycles.

The ECU of the used ICE provides two series controller that take the speed or ICE torque demand as reference value. For the reference measurements on the conventional ICE, the speed controller is used to control the speed demand, which is proportional to the accelerator position. In contrast, the series torque controller is used for the hybrid measurements to execute the set point torque of the hybrid controller on the shaft. Since the proposed control concept is supervisory in terms of the components, the parametrization of both series controller is not changed in any way.

The compensation of any SoC change in the battery is an important topic, which plays an significant role, especially at short load cycles. Many works address the issue to compensate the deviations correctly, e.g. [129], [74]. In this work, in order to avoid the problem, the values for fuel consumption and raw exhaust emissions are obtained by repeating any load cycle for 10 times and determining the average value. Almost all cycles reached the initial SoC after the 10-th cycle, due to what the SoC deviation can be neglected. Nevertheless, any significant deviations are marked in Table 5.3, where the results for the measured values of fuel consumption and raw exhaust emissions of the four representative cycles are summarized.

As can be seen in Table 5.3, fuel consumption, carbon monoxide (CO), hydrocarbons (HC) and soot emissions are significantly reduced, while nitrogen oxide (NOx) emissions are slightly increased. Note that the optimal rotational speed of the ICE is in the lower speed range, which has higher specific NOx emissions and increase therefore the NOx emissions. Nevertheless, the vehicle's after treatment system is capable to compensate the slightly increased raw NOx emissions.

It can be observed that significant SoC deviations mainly occur for $Q_m = 0.1$, which is caused by the small state penalty that focuses more on maximizing the powertrain efficiency than minimizing the SoC deviations. Nevertheless, the capacity limits of the battery are not

Cycle	Strategy	Fuel %	CO %	HC %	NOx %	Soot %
1	$Q_m = 10$	-2.04	-50.16	-9.64	8.12	-21.00
1	$Q_m = 0.1$	-2.98^*	-54.98^*	-13.46^*	8.44^*	-31.01^*
2	$Q_m = 10$	-2.00	-55.09	-14.99	7.45	-27.25
2	$Q_m = 0.1$	$-1.39^\bullet$	$-56.37^\bullet$	$-13.52^\bullet$	$8.99^\bullet$	$-29.81^\bullet$
3	$Q_m = 10$	-8.54	-71.76	-11.23	7.10	-17.74
3	$Q_m = 0.1$	$-9.14^\bullet$	$-70.70^\bullet$	$-3.65^\bullet$	$7.64^\bullet$	$-7.47^\bullet$
4	$Q_m = 10$	-3.79	-51.26	-11.59	9.27	-19.02
4	$Q_m = 0.1$	-4.26^*	-53.76^*	-11.76^*	9.52^*	-22.35^*

$*\dots$ Mean discharge ($\Delta \mathrm{SoC} < -0.05\,\%$, $\Delta \mathrm{SoC_{min}} = -0.33\,\%$)

$\bullet \dots$ Mean charge ($\Delta \mathrm{SoC} > 0.05\,\%$, $\Delta \mathrm{SoC_{max}} = 0.19\,\%$)

Table 5.3: Measured fuel and emission reductions of 4 representative cycles with enabled load and cycle prediction compared to conventional ICE operation.

even closely reached since the overall energy conversion is large compared to the deviations and two of the four test runs even increased the SoC in average.

Benefit for a cyclically working wheel loader using CD

Filla [35] analyzed different work cycles of wheel loaders in order to optimize the path trajectories to decrease fuel consumption and to increase productivity, respectively. The cycle detection targets for the same aims, but only based on the past load trajectory since the applied cycles are unknown in advance. In Figure 5.4, the influence on the system behavior due to enabled (subscript extension CD) and disabled cycle detection is depicted in more detail for the measurements of cycle number 3.

Subplot one in Figure 5.4 shows the rotational speed, while enlargement (a) emphasizes that due to the CD, the speed is increased prior to the load peak. This reduces the need of the electrical system to support any speed changes, which can be seen in marked region (b) in Subplot four, where the ISG torques are depicted. The SoC trajectories are shown in the last subplot, where in marked region (c), the difference is clearly observable. After the second recurrence, the cycle is detected and the master MPC optimizes across the predicted load trajectory, which enforces to optimally use the energy storage capabilities, minimizes the fuel consumption as well as exhaust emissions and fully considers the phlegmatisation. Any slightly larger deviation from the demand SoC has therefore less influence on the cost function than the efficiency improvement. It is important to mention that the cycle detection in principle needs at least two or more cycles to detect a cycle and reduces noise emissions due to the smoothed operation of the powertrain.

Another way to express the benefit is to calculate the rate of electrical and overall energy conversion, which follows for cycle number 3 to 28.14% with disabled CD and 25.21% with enabled CD. In other words, almost 3% less electrical system usage can be achieved if the information available from the past load trajectory is used accordingly in the control concept. Nevertheless, the reduction in fuel consumption and exhaust emissions are the main aims of the control concept and keeping the SoC at the demand SoC value is only of secondary importance. On this account, there is a great importance on the accuracy of the SoC value though.
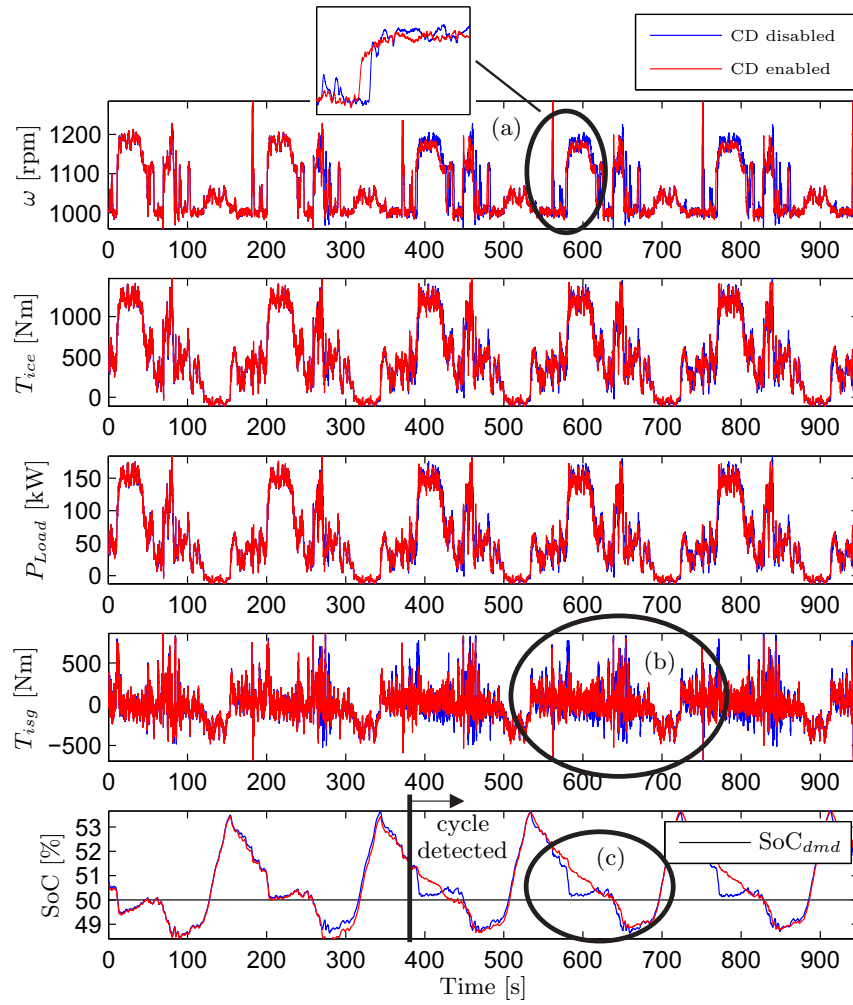
Figure 5.4: Comparison of controller behavior due to cycle detection with state penalty $Q_m = 0.1$.

Chapter 6

Conclusion and Outlook

In this work, the hybridization of non-road vehicles is discussed in terms of the control aspect. The work is motivated by the continuously increasing legislative regulations of non-road mobile machinery to decrease exhaust emissions and fuel consumption. Two topics are mainly relevant to be discussed in this context: The energy management system of the hybrid electric powertrain and the mandatory accurate estimation of the battery state of charge during operation.

First, the generic methodology for nonlinear system identification of battery models in the context of accurate real time SoC estimation is discussed. The SoC is not measurable on-line and needs to be estimated during operation, which in case of non-road vehicles is difficult due to the high dynamic usage of the electrical system. In order to obtain a precise battery model for different battery cell chemistries and different temperatures, the data based local model network approach is used to model the battery cell terminal voltage. The LMN consists of local linear models, which are interpolated to obtain the global nonlinear model output, while the LMN structure is iteratively built by the automatic LOLIMOT algorithm. Battery cells have strong nonlinear effects acting on the voltage, which need to be considered in the model structure. To this end, relaxation and hysteresis effects as well as the SoC, current and temperature are integrated by corresponding inputs in the LMN structure, which is enhanced by a prepartitioned network to achieve a physically appropriate network. A significant increase in model accuracy results from optimal model based design of experiments, where a model of the battery is used to optimize the excitation signal of battery cell tests. The high dynamic excitation signal consists of sufficient high currents, which are necessarily required for non-road applications. Furthermore, a real load cycle analysis is made to especially consider frequently used load ranges in operation. The results showed that a battery cell model accuracy with less than 3% NRMSE could be achieved, while currents above $20C$ were applied to the cell. A proposed measurement procedure guaranteed the reproducibility as well as comparability of the results.

Based on the battery cell model, different battery module models are built, while the results showed that the consideration of the additional internal resistance due to the cell connections can obviously increase the model quality significantly. Nevertheless, the results also showed that the disregard of the battery module internal resistance also achieves reasonable accuracy, which leads to the fact that if no battery module is available for measurements, the battery module model can nevertheless be built and used for principle analyses. A NRMSE of significantly less than 1.4% for the battery module models could be achieved. The obtained battery models could further be used in a SoC estimator based on the theory of Kalman filter. Due to the LMN models, a fuzzy observer is used to dynamically estimate the SoC during operation, which could achieve an accuracy below 5% depending on the used filter tuning. The results obtained with the fuzzy observer were compared to the SoC estimation provided by the battery management system of the battery module, which showed that the assumption of an inaccurate SoC estimation of the BMS after some time is justified.

Second, an energy management system is presented for a non-road parallel hybrid electric powertrain that considers physical constraints and the future load demand to achieve an optimal control. A cascaded model predictive control concept provides the possibilities to implement the mentioned requirements. The future load demand is in advance unknown, due to which two data based methodologies are introduced, which predict the disturbance trajectories of the vehicle with sufficient accuracy to be used in the control concept. To this end, a short term load trajectory prediction based on the Bayesian inference provides a load trajectory for the fast inner control loop, while a cycle detection based on correlation analysis is used to detect recurrent cycles in the past load signal. The strong nonlinear behavior of the electrical system is fully integrated by an iterative optimization of the master control loop.

Simulations and real time testbed measurements verify the feasibility of the concept on the application example of a wheel loader, while also a theoretic prove of stability is given. The special strategies downspeeding and phlegmatisation have a significant influence on the powertrain dynamics, which could be compensated by the proposed controller. At the expense of slightly increased NOx exhaust emissions, CO, HC and soot emissions as well as the fuel consumption are significantly reduced. The results showed furthermore that a change in the MPC penalties can easily implement different hybrid strategies on the powertrain due to which an easy portability to other vehicles is given.

Future work needs to be focused on an experimental vehicle, which must prove the overall methodology of energy and battery management system. Furthermore, the controller can be improved by integrating material behavior and penetration force of the wheels in the process model (see e.g. [109], [14]) .

List of Figures

List of Tables

Bibliography

[1] S. Abu-Sharkh and D. Doerffel. Rapid test and non-linear model characterisation of solid-state lithium-ion batteries. *Journal of Power Sources*, 130(1-2):266–274, 2004.

[2] Frank Allgöwer and Alex Zheng. *Nonlinear model predictive control*, volume 26. Birkhäuser Basel, 2000.

[3] Davide Andrea. *Battery management systems for large lithium ion battery packs*. Artech House, 2010.

[4] Robert Babuska. *Fuzzy modeling for control*. Kluwer Academic Publishers, 1998.

[5] Michael Back. *Prädiktive Antriebsregelung zum energieoptimalen Betrieb von Hybridfahrzeugen*. Univ.-Verlag Karlsruhe, [Online], 2005. Available: http://www.ksp.kit.edu/.

[6] Stefan Banach. Sur les opérations dans les ensembles abstraits et leur application aux équations intégrales. *Fund. Math*, 3(1):133–181, 1922.

[7] Kamil Cagatay Bayindir, Mehmet Ali Gözükücük, and Ahmet Teke. A comprehensive overview of hybrid electric vehicle: Powertrain configurations, powertrain control techniques and electronic control units. *Energy Conversion and Management*, 52(2):1305–1313, 2011.

[8] WF Bentley. Cell balancing considerations for lithium-ion battery systems. In *Twelfth Annual Battery Conference on Applications and Advances*, pages 223–226. IEEE, 1997.

[9] Pontus Bergsten, Rainer Palm, and Dimiter Driankov. Observers for takagi-sugeno fuzzy systems. *IEEE Transactions on Systems, Man, and Cybernetics, Part B: Cybernetics*, 32(1):114–121, 2002.

[10] D.M. Bernardi and J.Y. Go. Analysis of pulse and relaxation behavior in lithium-ion batteries. *Journal of Power Sources*, 196(1):412–427, 2011.

[11] Bikramjit S Bhangu, Paul Bentley, David A Stone, and Christopher M Bingham. Nonlinear observers for predicting state-of-charge and state-of-health of lead-acid batteries for hybrid-electric vehicles. *IEEE Transactions on Vehicular Technology*, 54(3):783–794, 2005.

[12] SA Billings and Luis Antonio Aguirre. Effects of the sampling time on the dynamics and identification of nonlinear models. *International Journal of Bifurcation and Chaos*, 5(06):1541–1556, 1995.

[13] Henk AP Blom and Yaakov Bar-Shalom. The interacting multiple model algorithm for systems with Markovian switching coefficients. *IEEE Transactions on Automatic Control*, 33(8):780–783, 1988.

[14] Stéphane Blouin, Ahmad Hemami, and Mike Lipsett. Review of resistive force models for earthmoving processes. *Journal of Aerospace Engineering*, 14(3):102–111, 2001.

[15] Hosein Ali Borhan, Chen Zhang, Ardalan Vahidi, Anthony M Phillips, Ming L Kuang, and Stefano Di Cairano. Nonlinear model predictive control for power-split hybrid electric vehicles. In *49th IEEE Conference on Decision and Control (CDC)*, pages 4890–4895. IEEE, 2010.

[16] George EP Box and George C Tiao. *Bayesian inference in statistical analysis*, volume 40. John Wiley & Sons, 2011.

[17] E.F. Camacho and C. Bordons. *Model predictive control*. Springer, 1999.

[18] Jian Cao, Nigel Schofield, and Ali Emadi. Battery balancing methods: A comprehensive review. In *Vehicle Power and Propulsion Conference (VPPC'08)*, pages 1–6. IEEE, 2008.

[19] M. Charkhgard and M. Farrokhi. State-of-charge estimation for lithium-ion batteries using neural networks and EKF. *IEEE Transactions on Industrial Electronics*, 57(12):4178–4187, 2010.

[20] N.A. Chaturvedi, R. Klein, J. Christensen, J. Ahmed, and A. Kojic. Algorithms for advanced battery management systems: Modeling, estimation, and control challenges for lithium-ion batteries. *Control Systems Magazine, IEEE*, 30(3):49–68, 2010.

[21] Guanrong Chen, Qingxian Xie, and Leang S. Shieh. Fuzzy kalman filtering. *Information Sciences*, 109(1-4):197–209, 1998.

[22] M. Chen and G.A. Rincon-Mora. Accurate electrical battery model capable of predicting runtime and IV performance. *IEEE Transactions on Energy conversion*, 21(2):504–511, 2006.

[23] Zhihang Chen, Shiqi Qiu, M Abul Masrur, and Yi Lu Murphey. Battery state of charge estimation based on a combined model of extended kalman filter and neural networks. In *The 2011 International Joint Conference on Neural Networks (IJCNN)*, pages 2156–2163. IEEE, 2011.

[24] D.A. Cohn. Neural network exploration using optimal experiment design. *Neural Networks*, 9(6):1071–1083, 1996.

[25] Ralph B D'Agostino. *Goodness-of-fit-techniques*, volume 68. CRC press, 1986.

[26] Mohamed Daowd, Noshin Omar, Peter Van Den Bossche, and Joeri Van Mierlo. Passive and active battery balancing comparison based on matlab simulation. In *Vehicle Power and Propulsion Conference (VPPC'11)*, pages 1–7. IEEE, 2011.

[27] JP Marques De Sá. *Applied Statistics: Using SPSS, Statistica, MATLAB, and R*. Springer, 2nd edition, 2007.

[28] M Deflorian and F Klöpper. Design of dynamic experiments. *Design of Experiments (DoE) in Engine Development*, 4:31–40, 2009.

[29] Chirag Desai and Sheldon S Williamson. Comparative study of hybrid electric vehicle control strategies for improved drivetrain efficiency analysis. In *Electrical Power & Energy Conference (EPEC)*, pages 1–6. IEEE, 2009.

[30] Dinh Vinh Do, Christophe Forgez, Khadija El Kadri Benkara, and Guy Friedrich. Impedance observer for a li-ion battery using kalman filter. *IEEE Transactions on Vehicular Technology*, 58(8):3930–3937, 2009.

[31] M. Doyle, T.F. Fuller, and J. Newman. Modeling of galvanostatic charge and discharge of the lithium/polymer/insertion cell. *Journal of the Electrochemical Society*, 140(6):1526–1533, 1993.

[32] Matthieu Dubarry, Nicolas Vuillaume, and Bor Yann Liaw. From li-ion single cell model to battery pack simulation. In *IEEE International Conference on Control Applications (CCA)*, pages 708–713. IEEE, 2008.

[33] Matthieu Dubarry, Nicolas Vuillaume, and Bor Yann Liaw. From single cell model to battery pack simulation for li-ion batteries. *Journal of Power Sources*, 186(2):500–507, 2009.

[34] Sajjad Fekri and Francis Assadian. The role and use of robust multivariable control in hybrid electric vehicle energy management-part i: An overview. In *IEEE International Conference on Control Applications (CCA)*, pages 303–309. IEEE, 2012.

[35] R. Filla. Optimizing the trajectory of a wheel loader working in short loading cycles. In *The 13th Scandinavian International Conference on Fluid Power (SICFP2013)*, pages 307–317, 2013.

[36] Reno Filla. Hybrid power systems for construction machinery: Aspects of system design and operability of wheel loaders. In *International Mechanical Engineering Congress and Exposition*, pages 611–620. ASME, 2009.

[37] Christophe Forgez, Dinh Vinh Do, Guy Friedrich, Mathieu Morcrette, and Charles Delacourt. Thermal modeling of a cylindrical $LiFePO_4$/graphite lithium-ion battery. *Journal of Power Sources*, 195(9):2961–2968, 2010.

[38] Bobbie Frank, Lennart Skogh, and Mats Alaküla. On wheel loader fuel efficiency difference due to operator behaviour distribution. In *2nd International Commercial Vehicle Technology Symposium (CVT)*, 2012.

[39] Behnam Ganji and Abbas Z Kouzani. A look-ahead road grade determination method for hevs. In *Electrical engineering and control*, pages 703–711. Springer, 2011.

[40] L. Gao, S. Liu, and R.A. Dougal. Dynamic lithium-ion battery model for system simulation. *IEEE Transactions on Components and Packaging Technologies*, 25(3):495–505, 2002.

[41] Wenzhong Gao and Sachin Kumar Porandla. Design optimization of a parallel hybrid electric powertrain. In *Vehicle Power and Propulsion Conference (VPPC'05)*, pages 6–pp. IEEE, 2005.

[42] Yuan Gao. Existence and uniqueness theorem on uncertain differential equations with local Lipschitz condition. *Journal of Uncertain Systems*, 6(3):223–232, 2012.

[43] Elmer G Gilbert and Kok Tin Tan. Linear systems with state and control constraints: The theory and application of maximal output admissible sets. *IEEE Transactions on Automatic Control*, 36(9):1008–1020, 1991.

[44] Jamie Gomez, Ruben Nelson, Egwu E Kalu, Mark H Weatherspoon, and Jim P Zheng. Equivalent circuit model parameters of a high-power li-ion battery: Thermal and state of charge effects. *Journal of Power Sources*, 196(10):4826–4831, 2011.

[45] AH González, EJ Adam, and JL Marchetti. Conditions for offset elimination in state space receding horizon controllers: A tutorial analysis. *Chemical Engineering and Processing: Process Intensification*, 47(12):2184–2194, 2008.

[46] G.C. Goodwin and R.L. Payne. *Dynamic system identification: Experiment design and data analysis.* Academic Press Inc., New York, 1977.

[47] G. Gregorcic and G. Lightbody. Local model network identification with gaussian processes. *IEEE Transactions on Neural Networks*, 18(5):1404–1423, 2007.

[48] David S Gunderson. Handbook of mathematical induction: Theory and applications. *AMC*, 10:12, 2010.

[49] C. Hametner and S. Jakubek. Neuro-fuzzy modelling using a logistic discriminant tree. In *American Control Conference*, pages 864–869. IEEE, 2007.

[50] C. Hametner, J. Unger, and S. Jakubek. Local model network based dynamic battery cell model identification. In *12th WSEAS International Conference on Robotics, Control and Manufacturing Technology*, pages 116–123. WSEAS, 2012.

[51] Christoph Hametner and Stefan Jakubek. State of charge estimation for lithium ion cells: Design of experiments, nonlinear identification and fuzzy observer design. *Journal of Power Sources*, 238(0):413 – 421, 2013.

[52] Christoph Hametner, Wenzel Prochazka, Amra Suljanovic, and Stefan Jakubek. Model based lithium ion cell ageing data analysis. In *IEEE International Conference on Fuzzy Systems (FUZZ-IEEE)*, pages 962–967. IEEE, 2014.

[53] Christoph Hametner, Markus Stadlbauer, Maxime Deregnaucourt, and Stefan Jakubek. Incremental optimal process excitation for online system identification based on evolving local model networks. *Mathematical and Computer Modelling of Dynamical Systems*, 19(6):505–525, 2013.

[54] Christoph Hametner, Markus Stadlbauer, Maxime Deregnaucourt, Stefan Jakubek, and Thomas Winsel. Optimal experiment design based on local model networks and multilayer perceptron networks. *Engineering Applications of Artificial Intelligence*, 26(1):251–261, 2013.

[55] Jaehyun Han, Dongchul Kim, and Myoungho Sunwoo. State-of-charge estimation of lead-acid batteries using an adaptive extended kalman filter. *Journal of Power Sources*, 188(2):606–612, 2009.

[56] B. Hartmann, J. Moll, O. Nelles, and C.P. Fritzen. Hierarchical local model trees for design of experiments in the framework of ultrasonic structural health monitoring. In *IEEE International Conference on Control Applications*, pages 1163–1170. IEEE, 2011.

[57] Hongwen He, Rui Xiong, Xiaowei Zhang, Fengchun Sun, and JinXin Fan. State-of-charge estimation of the lithium-ion battery using an adaptive extended kalman filter based on an improved thevenin model. *IEEE Transactions on Vehicular Technology*, 60(4):1461–1469, 2011.

[58] Siegfried Helm, Martin Kozek, and Stefan Jakubek. Combustion torque estimation and misfire detection for calibration of combustion engines by parametric Kalman filtering. *IEEE Transactions on Industrial Electronics*, 59(11):4326–4337, 2012.

[59] A. Hentunen, Lehmuspelto T., and Suomela J. Electrical battery model for dynamic simulations of hybrid electric vehicles. In *Vehicle Power and Propulsion Conference (VPPC'11)*, pages 1–6. IEEE, 2011.

[60] F. Hoffmann and O. Nelles. Genetic programming for model selection of tsk-fuzzy systems. *Information Sciences*, 136(1):7–28, 2001.

[61] Xiao Hu, Shaohua Lin, and Scott Stanton. A novel thermal model for HEV/EV battery modeling based on CFD calculation. In *Energy Conversion Congress and Exposition (ECCE)*, pages 893–900. IEEE, 2010.

[62] Xiaosong Hu, Fengchun Sun, and Yuan Zou. Estimation of state of charge of a lithium-ion battery pack for electric vehicles using an adaptive Luenberger observer. *Energies*, 3(9):1586–1603, 2010.

[63] Y. Hu, B.J. Yurkovich, S. Yurkovich, and Y. Guezennec. Electro-thermal battery modeling and identification for automotive applications. In *Dynamic Systems and Control Conference*, pages 233–240. ASME, 2009.

[64] Y Hu and S Yurkovich. Battery cell state-of-charge estimation using linear parameter varying system techniques. *Journal of Power Sources*, 198:338–350, 2012.

[65] Y. Hu, S. Yurkovich, Y. Guezennec, and BJ Yurkovich. A technique for dynamic battery model identification in automotive applications using linear parameter varying structures. *Control Engineering Practice*, 17(10):1190–1201, 2009.

[66] Y. Hu, S. Yurkovich, Y. Guezennec, and BJ Yurkovich. Electro-thermal battery model identification for automotive applications. *Journal of Power Sources*, 196(1):449–457, 2011.

[67] T Hulnhagen, Ingo Dengler, Andreas Tamke, Thao Dang, and Gabi Breuel. Maneuver recognition using probabilistic finite-state machines and fuzzy logic. In *Intelligent Vehicles Symposium (IV)*, pages 65–70. IEEE, 2010.

[68] Vasile I Istratescu. *Fixed point theory: an introduction*, volume 7. Springer, 2001.

[69] Robyn Jackey, Michael Saginaw, Pravesh Sanghvi, Javier Gazzarri, Tarun Huria, and Massimo Ceraolo. Battery model parameter estimation using a layered technique: An example using a lithium iron phosphate cell. *SAE Technical Paper 2013-01-1547*, 2013.

[70] S. Jakubek and C. Hametner. Identification of neurofuzzy models using GTLS parameter estimation. *IEEE Transactions on Systems, Man, and Cybernetics, Part B: Cybernetics*, 39(5):1121–1133, 2009.

[71] Stefan Jakubek and Nikolaus Keuth. A local neuro-fuzzy network for high-dimensional models and optimization. *Engineering Applications of Artificial Intelligence*, 19(6):705–717, 2006.

[72] Dong Hyup Jeon and Seung Man Baek. Thermal modeling of cylindrical lithium ion battery during discharge cycle. *Energy Conversion and Management*, 52(8):2973–2981, 2011.

[73] ZL Jing, ACJ Luo, and M. Tomizuka. A stochastic fuzzy neural network for nonlinear dynamic systems. *International Journal of Intelligent Control and Systems*, 3(2):193–203, 1998.

[74] Valerie H Johnson, Keith B Wipke, and David J Rausen. Hev control strategy for real-time optimization of fuel economy and emissions. *SAE Technical Paper 2000-01-1543*, 2000.

[75] Dah-Jing Jwo and Chien-Hao Tseng. Fuzzy adaptive interacting multiple model unscented kalman filter for integrated navigation. In *Control Applications (CCA) & Intelligent Control (ISIC)*, pages 1684–1689. IEEE, 2009.

[76] Tomaz Katrasnik. Analytical framework for analyzing the energy conversion efficiency of different hybrid electric vehicle topologies. *Energy Conversion and Management*, 50(8):1924–1938, 2009.

[77] Georgia-Evangelia Katsargyri, Ilya V Kolmanovsky, John Michelini, Ming L Kuang, Anthony M Phillips, Michael Rinehart, and Munther A Dahleh. Optimally controlling hybrid electric vehicles using path forecasting. In *American Control Conference*, pages 4613–4617. Institute of Electrical and Electronics Engineers, 2009.

[78] SS Keerthi and EG Gilbert. Computation of minimum-time feedback control laws for discrete-time systems with state-control constraints. *IEEE Transactions on Automatic Control*, 32(5):432–435, 1987.

[79] Il-Song Kim. The novel state of charge estimation method for lithium battery using sliding mode observer. *Journal of Power Sources*, 163(1):584–590, 2006.

[80] Jonghoon Kim, Jongwon Shin, Changyoon Chun, and BH Cho. Stable configuration of a Li-ion series battery pack based on a screening process for improved voltage/SOC balancing. *IEEE Transactions on Power Electronics*, 27(1):411–424, 2012.

[81] Jonghoon Kim, Jongwon Shin, Changyoon Jeon, and Bohyung Cho. High accuracy state-of-charge estimation of li-ion battery pack based on screening process. In *26th Annual IEEE Applied Power Electronics Conference and Exposition (APEC)*, pages 1984–1991. IEEE, 2011.

[82] R. Klein, N.A. Chaturvedi, J. Christensen, J. Ahmed, R. Findeisen, and A. Kojic. State estimation of a reduced electrochemical model of a lithium-ion battery. In *American Control Conference*, pages 6618–6623. IEEE, 2010.

[83] O Konig, G Prochart, C Hametner, and Stefan Jakubek. Battery emulation for power-hil using local model networks and robust impedance control. *IEEE Transactions on Industrial Electronics*, 61(2):943–955, 2014.

[84] Oliver König, Gregor Gregorčič, and Stefan Jakubek. Model predictive control of a DC–DC converter for battery emulation. *Control Engineering Practice*, 21(4):428–440, 2013.

[85] R.C. Kroeze and P.T. Krein. Electrical battery model for use in dynamic electric vehicle simulations. In *Power Electronics Specialists Conference*, pages 1336–1342. IEEE, 2008.

[86] Tae-Suk Kwon, Seon-Woo Lee, Seung-Ki Sul, Cheol-Gyu Park, Nag-In Kim, Byung-il Kang, and Min-seok Hong. Power control algorithm for hybrid excavator with supercapacitor. *IEEE Transactions on Industry Applications*, 46(4):1447–1455, 2010.

[87] S Shawn Lee, Tae H Kim, S Jack Hu, Wayne W Cai, and Jeffrey A Abell. Joining technologies for automotive lithium-ion battery manufacturing: A review. In *International Manufacturing Science and Engineering Conference*, pages 541–549. ASME, 2010.

[88] Seongjun Lee, Jonghoon Kim, Jaemoon Lee, and BH Cho. State-of-charge and capacity estimation of lithium-ion battery using a new open-circuit voltage versus state-of-charge. *Journal of Power Sources*, 185(2):1367–1373, 2008.

[89] Yuang-Shung Lee and Ming-Wang Cheng. Intelligent control battery equalization for series connected lithium-ion battery strings. *IEEE Transactions on Industrial Electronics*, 52(5):1297–1307, 2005.

[90] Zsófia Lendek, Robert Babuska, and Bart De Schutter. Stability of cascaded fuzzy systems and observers. *IEEE Transactions on Fuzzy Systems*, 17(3):641–653, 2009.

[91] Chan-Chiao Lin, Soonil Jeon, Huei Peng, and Jang Moo Lee. Driving pattern recognition for control of hybrid electric trucks. *Vehicle System Dynamics*, 42(1-2):41–58, 2004.

[92] Chan-Chiao Lin, Huei Peng, Jessy W Grizzle, and Jun-Mo Kang. Power management strategy for a parallel hybrid electric truck. *IEEE Transactions on Control Systems Technology*, 11(6):839–849, 2003.

[93] Ing Nils Lindenkamp and Dipl-Ing Benjamin Tilch. Reducing of exhaust emissions from diesel hybrid vehicles. *MTZ worldwide*, 73(7-8):64–69, 2012.

[94] Lennart Ljung. *System identification*. Springer, 1998.

[95] Andrea Lorenz and Martin Kozek. Automatic cycle border detection for a statistic evaluation of the loading process of earth-moving vehicles. *Commercial Vehicle Engineering Congress and Exhibition*, pages 08–12, 2007.

[96] D.G. Luenberger and Y. Ye. *Linear and nonlinear programming*. Springer, 3rd edition, 2008.

[97] Sergey Edward Lyshevski. Energy conversion and optimal energy management in diesel–electric drivetrains of hybrid-electric vehicles. *Energy conversion and management*, 41(1):13–24, 2000.

[98] J.R. Magnus and H. Neudecker. *Matrix differential calculus with applications in statistics and econometrics*. Wiley, 2nd edition, 1988.

[99] Joaquim P Marques De Sá. *Applied statistics using SPSS, STATISTICA and MATLAB*. Springer, 2003.

[100] David Q Mayne, James B Rawlings, Christopher V Rao, and Pierre OM Scokaert. Constrained model predictive control: Stability and optimality. *Automatica*, 36(6):789–814, 2000.

[101] Christian H Mayr, Andreas Fleck, and Stefan Jakubek. Hybrid powertrain control using optimization and cycle based predictive control algorithms. In *9th IEEE International Conference on Control and Automation (ICCA)*, pages 937–944. IEEE, 2011.

[102] Christian H Mayr, Christoph Hametner, Martin Kozek, and Stefan Jakubek. Piecewise quadratic stability analysis for local model networks. In *IEEE International Conference on Control Applications (CCA)*, pages 1418–1424. IEEE, 2011.

[103] Efim Mazor, Amir Averbuch, Yakov Bar-Shalom, and Joshua Dayan. Interacting multiple model methods in target tracking: a survey. *IEEE Transactions on Aerospace and Electronic Systems*, 34(1):103–123, 1998.

[104] M Montazeri-Gh, A Ahmadi, and M Asadi. Driving condition recognition for genetic-fuzzy hev control. In *3rd International Workshop on Genetic and Evolving Systems (GEFS)*, pages 65–70. IEEE, 2008.

[105] Scott Jason Moura, Hosam K Fathy, Duncan S Callaway, and Jeffrey L Stein. A stochastic optimal control approach for power management in plug-in hybrid electric vehicles. *IEEE Transactions on Control Systems Technology*, 19(3):545–555, 2011.

[106] R. Murray-Smith and T. Johansen. *Multiple model approaches to nonlinear modelling and control*. CRC Press, 1997.

[107] O. Nelles. *Nonlinear system identification: from classical approaches to neural networks and fuzzy models*. Springer, Berlin, 2001.

[108] O. Nelles and R. Isermann. Basis function networks for interpolation of local linear models. In *Proceedings of the 35th IEEE Decision and Control*, volume 1, pages 470–475. IEEE, 1996.

[109] Yue Ning and Xin Hui Liu. Research on the resistance acting on the bucket during shovelling. *Advanced Materials Research*, 787:778–781, 2013.

[110] Tobias Nüesch, Mu Wang, Pascal Isenegger, Christopher H Onder, Rüdiger Steiner, Pedro Macri-Lassus, and Lino Guzzella. Optimal energy management for a diesel hybrid electric vehicle considering transient PM and quasi-static NOx emissions. *Control Engineering Practice*, 29(August 2014):266–276, 2014.

[111] Katsuhiko Ogata. *Discrete-Time Control Systems*, volume 8. Prentice-Hall Englewood Cliffs, NJ, 2nd edition, 1995.

[112] Kazuo Onda, Takamasa Ohshima, Masato Nakayama, Kenichi Fukuda, and Takuto Araki. Thermal behavior of small lithium-ion battery during rapid charge and discharge cycles. *Journal of Power sources*, 158(1):535–542, 2006.

[113] Bharath Pattipati, Chaitanya Sankavaram, and Krishna R. Pattipati. System identification and estimation framework for pivotal automotive battery management system characteristics. *IEEE Transactions on Systems, Man, and Cybernetics, Part C: Applications and Reviews*, pages 1–16, 2010.

[114] F Payri, C Guardiola, B Pla, and D Blanco-Rodriguez. A stochastic method for the energy management in hybrid electric vehicles. *Control Engineering Practice*, 29(August 2014):257–265, 2014.

[115] Pierluigi Pisu and Giorgio Rizzoni. A comparative study of supervisory control strategies for hybrid electric vehicles. *IEEE Transactions on Control Systems Technology*, 15(3):506–518, 2007.

[116] G.L. Plett. Extended Kalman filtering for battery management systems of LiPB-based HEV battery packs: Part 1. Background. *Journal of Power Sources*, 134(2):252–261, 2004.

[117] G.L. Plett. Extended Kalman filtering for battery management systems of LiPB-based HEV battery packs: Part 2. Modeling and identification. *Journal of Power Sources*, 134(2):262–276, 2004.

[118] G.L. Plett. Extended Kalman filtering for battery management systems of LiPB-based HEV battery packs: Part 3. State and parameter estimation. *Journal of Power Sources*, 134(2):277–292, 2004.

[119] Gregory L Plett. High-performance battery-pack power estimation using a dynamic cell model. *IEEE Transactions on Vehicular Technology*, 53(5):1586–1593, 2004.

[120] Amir Poursamad and Morteza Montazeri. Design of genetic-fuzzy control strategy for parallel hybrid electric vehicles. *Control Engineering Practice*, 16(7):861–873, 2008.

[121] BK Powell. A dynamic model for automotive engine control analysis. In *18th IEEE Conference on Decision and Control including the Symposium on Adaptive Processes*, volume 18, pages 120–126. IEEE, 1979.

[122] L. Pronzato. Optimal experimental design and some related control problems. *Automatica*, 44(2):303–325, 2008.

[123] Tran Dinh Quoc, Carlo Savorgnan, and Moritz Diehl. Real-time sequential convex programming for optimal control applications. In *Modeling, Simulation and Optimization of Complex Processes*, pages 91–102. Springer, 2012.

[124] James Blake Rawlings and David Q Mayne. *Model predictive control: Theory and design.* Nob Hill Pub., 2009.

[125] Stefan Richter, Colin Neil Jones, and Manfred Morari. Real-time input-constrained MPC using fast gradient methods. In *48th IEEE Conference on Decision and Control held jointly with the 28th Chinese Control Conference (CDC/CCC)*, pages 7387–7393. IEEE, 2009.

[126] Stefan Richter, Sébastien Mariéthoz, and Manfred Morari. High-speed online MPC based on a fast gradient method applied to power converter control. In *American Control Conference (ACC)*, pages 4737–4743. IEEE, 2010.

[127] Osvaldo J. Rojas, Graham C. Goodwin, Maria M. Seron, and Arie Feuer. An SVD based strategy for receding horizon control of input constrained linear systems. *Int. J. Robust Nonlinear Control*, 14:1207–1226, 2004.

[128] S. Santhanagopalan and R.E. White. Online estimation of the state of charge of a lithium ion cell. *Journal of Power Sources*, 161(2):1346–1355, 2006.

[129] Antonio Sciarretta, Michael Back, and Lino Guzzella. Optimal control of parallel hybrid electric vehicles. *IEEE Transactions on Control Systems Technology*, 12(3):352–363, 2004.

[130] Antonio Sciarretta and Lino Guzzella. Control of hybrid electric vehicles. *Control systems, IEEE*, 27(2):60–70, 2007.

[131] Chitradeep Sen and Narayan C Kar. Battery pack modeling for the analysis of battery management system of a hybrid electric vehicle. In *Vehicle Power and Propulsion Conference (VPPC'09)*, pages 207–212. IEEE, 2009.

[132] R Senthil, K Janarthanan, and J Prakash. Nonlinear state estimation using fuzzy kalman filter. *Industrial & engineering chemistry research*, 45(25):8678–8688, 2006.

[133] M. Seyr and S. Jakubek. Dynamic trajectory generation via numerical multi-objective optimisation. In *American Control Conference*, pages 3336–3341. IEEE, 2007.

[134] Dan Simon. Kalman filtering for fuzzy discrete time dynamic systems. *Applied Soft Computing*, 3(3):191–207, 2003.

[135] Daniel Simon, Johan Lofberg, and Torkel Glad. Reference tracking MPC using terminal set scaling. In *IEEE 51st Annual Conference on Decision and Control (CDC)*, pages 4543–4548. IEEE, 2012.

[136] K. Smith and C.Y. Wang. Power and thermal characterization of a lithium-ion battery pack for hybrid-electric vehicles. *Journal of Power Sources*, 160(1):662–673, 2006.

[137] K.A. Smith, C.D. Rahn, and C.Y. Wang. Model-based electrochemical estimation and constraint management for pulse operation of lithium ion batteries. *IEEE Transactions on Control Systems Technology*, 18(3):654–663, 2010.

[138] Haryong Song, Vladimir Shin, and Moongu Jeon. Mobile node localization using fusion prediction-based interacting multiple model in cricket sensor network. *IEEE Transactions on Industrial Electronics*, 59(11):4349–4359, 2012.

[139] M. Stadlbauer, C. Hametner, S. Jakubek, and T. Winsel. Analytic multilayer perceptron based experiment design for nonlinear systems. In *Proceedings of the Eighth IFAC World Congress*, pages 4332–4337, 2011.

[140] Markus Stadlbauer, Christoph Hametner, and Stefan Jakubek. Analytic model based design of experiments for nonlinear dynamic systems with constraints. In *Proceedings of the IASTED International Conference in Control and Applications*, volume 20, 2011.

[141] F. Sun, R. Xiong, H. He, W. Li, and J.E.E. Aussems. Model-based dynamic multi-parameter method for peak power estimation of lithium-ion batteries. *Applied Energy*, 96:378–386, 2012.

[142] Fengchun Sun, Xiaosong Hu, Yuan Zou, and Siguang Li. Adaptive unscented Kalman filtering for state of charge estimation of a lithium-ion battery for electric vehicles. *Energy*, 36(5):3531–3540, 2011.

[143] Hongguang Sun, Xiaohui Wang, Brian Tossan, and Regan Dixon. Three-dimensional thermal modeling of a lithium-ion battery pack. *Journal of power Sources*, 206:349–356, 2012.

[144] Kazuo Tanaka, Takayuki Ikeda, and Hua O Wang. Fuzzy regulators and fuzzy observers: relaxed stability conditions and LMI-based designs. *IEEE Transactions on Fuzzy Systems*, 6(2):250–265, 1998.

[145] X. Tang, X. Zhang, B. Koch, and D. Frisch. Modeling and estimation of Nickel Metal Hydride battery hysteresis for SOC estimation. In *IEEE International Conference on Prognostics and Health Management*, pages 1–12. IEEE, 2008.

[146] The European Parliament and Council of the European Union. Directive 97/68/EC of the European Parliament and of the Council of 16 December 1997 on the approximation of the laws of the Member States relating to measures against the emission of gaseous and particulate pollutants from internal combustion engines to be installed in non-road mobile machinery, 1997.

[147] The European Parliament and Council of the European Union. Proposal for a regulation of the European Parliament and of the Council on requirements relating to emission limits and type-approval for internal combustion engines for non-road mobile machinery, 2014/0268/COD, 2014.

[148] Petter Tondel and Tor A. Johansen. Complexity reduction in explicit linear model predictive control. In *15th Triennial World Congress of the International Federation of Automatic Control*, 2002.

[149] J. Unger, C. Hametner, and S. Jakubek. Optimal model based design of experiments applied to high current rate battery cells. In *Conference on Electrical Systems for Aircraft, Railway and Ship Propulsion*, pages 1–6, 2012.

[150] Johannes Unger, Christoph Hametner, Stefan Jakubek, and Marcus Quasthoff. A novel methodology for non-linear system identification of battery cells used in non-road hybrid electric vehicles. *Journal of Power Sources*, 269:883–897, 2014.

[151] Johannes Unger, Martin Kozek, and Stefan Jakubek. Reduced order optimization for model predictive control using principal control moves. *Journal of Process Control*, 22(1):272–279, 2012.

[152] Johannes Unger, Martin Kozek, and Stefan Jakubek. Nonlinear model predictive energy management controller with load and cycle prediction for non-road HEV. *Control Engineering Practice*, 36:120–132, 2015.

[153] A Vasebi, SMT Bathaee, and M Partovibakhsh. Predicting state of charge of lead-acid batteries for hybrid electric vehicles by extended Kalman filter. *Energy Conversion and Management*, 49(1):75–82, 2008.

[154] Amir Vasebi, Maral Partovibakhsh, and S Mohammad Taghi Bathaee. A novel combined battery model for state-of-charge estimation in lead-acid batteries based on extended kalman filter for hybrid electric vehicle applications. *Journal of Power Sources*, 174(1):30–40, 2007.

[155] M. Verbrugge and E. Tate. Adaptive state of charge algorithm for nickel metal hydride batteries including hysteresis phenomena. *Journal of Power Sources*, 126(1-2):236–249, 2004.

[156] Mathukumalli Vidyasagar. *Nonlinear systems analysis*, volume 42. Siam, 2002.

[157] J. Wang and Q. Chen. Stochastic fuzzy neural network and its robust parameter learning algorithm. *Advances in Neural Networks*, pages 199–221, 2005.

[158] JP Wang, L Xu, JG Guo, and L Ding. Modelling of a battery pack for electric vehicles using a stochastic fuzzy neural network. *Proceedings of the Institution of Mechanical Engineers, Part D: Journal of Automobile Engineering*, 223(1):27–35, 2009.

[159] Liuping Wang. *Model Predictive Control System Design and Implementation Using* Matlab. Springer, 1st edition, 2009.

[160] L.X. Wang. *Adaptive fuzzy systems and control: Design and stability analysis*. Prentice Hall, 1994.

[161] Yang Wang and Stephen Boyd. Fast model predictive control using online optimization. *IEEE Transactions on Control Systems Technology*, 18(2):267–278, 2010.

[162] Nicolas Watrin, David Bouquain, Benjamin Blunier, and Abdellatif Miraoui. Multiphysical lithium-based battery pack modeling for simulation purposes. In *Vehicle Power and Propulsion Conference (VPPC'11)*, pages 1–5. IEEE, 2011.

[163] Michel Weibel, Volker Schmeißer, and Frank Hofmann. Model-based approaches to exhaust aftertreatment system development. In *Urea-SCR Technology for deNOx After Treatment of Diesel Exhausts*, pages 691–707. Springer, 2014.

[164] Phil Weicker. *A systems approach to Lithium-Ion battery management*. Artech house, 2013.

[165] Qing Xiao, Qingfeng Wang, and Yanting Zhang. Control strategies of power system in hybrid hydraulic excavator. *Automation in Construction*, 17(4):361–367, 2008.

[166] Long Xu, Junping Wang, and Quanshi Chen. Kalman filtering state of charge estimation for battery management system based on a stochastic fuzzy neural network battery model. *Energy Conversion and Management*, 53(1):33–39, 2012.

[167] Fengjun Yan, Junmin Wang, and Kaisheng Huang. Hybrid electric vehicle model predictive control torque-split strategy incorporating engine transient characteristics. *IEEE Transactions on Vehicular Technology*, 61(6):2458–2467, 2012.

[168] Shifei Yuan, Hongjie Wu, and Chengliang Yin. State of Charge Estimation Using the Extended Kalman Filter for Battery Management Systems Based on the ARX Battery Model. *Energies*, 6(1):444–470, 2013.

[169] Melanie Nicole Zeilinger, Colin Neil Jones, and Manfred Morari. Real-time suboptimal model predictive control using a combination of explicit MPC and online optimization. *IEEE Transactions on Automatic Control*, 56(7):1524–1534, 2011.

CURRICULUM VITAE

Personal Information

Name	Dipl.-Ing. Johannes Unger
Date of birth	13th of May 1987
Birthplace	Vienna
Gender	Male
Nationality	Austria
Address	Sonnwendgasse 34/32, 1100 Vienna, Austria

Education

03/2011 - 05/2015	Vienna University of Technology, Vienna Doctoral studies in Mechanical Engineering
08/2009 - 01/2010	The City College of New York Semester abroad New York City, United States of America
10/2005 - 01/2011	Vienna University of Technology, Vienna Diploma studies in Mechanical Engineering Specialization in Mechatronics Passed with distinction (January 26, 2011)
09/1997 - 06/2005	BRG IV Waltergasse, Vienna (secondary school) Final examination passed with distinction (June 7, 2005)
09/1993 - 06/1997	PVS Waldkloster, Vienna (elementary school)

Doctoral Thesis

Title	Energy and battery management for non-road hybrid electric vehicles
Supervisor	Univ.Prof. Dipl.-Ing. Dr. techn. Stefan Jakubek
Industrial Partners	LIEBHERR Machines Bulle S.A. LIEBHERR Werk Bischofshofen GmbH LIEBHERR-Werk Nenzing GmbH Kristl, Seibt & Co GmbH Graz University of Technology Forschungsgesellschaft für Verbrennungskraftmaschinen und Thermodynamik GmbH
Description	The work provides a control concept for parallel hybrid electric powertrains in non-road vehicles and presents methodologies for nonlinear system identification of battery models in order to achieve a high accurate state of charge estimation during operation of non-road vehicles.

Diploma Thesis

Title	Control based analysis of a gas dosing system for stationary gas engines
Supervisor	Univ.Prof. Dipl.-Ing. Dr. techn. Stefan Jakubek
Industrial Partner	HOERBIGER Ventilwerke GmbH & Co KG
Description	In the work, an active gas dosing system for a stationary gas engine is developed and different control strategies are analyzed, in order to show the different control possibilities of such systems.

Honors and Awards

November 19th, 2012	NRW Young Scientist Award 2012 from the International Graduate School of Dynamic Intelligent Systems for the Publication "Reduced Order Optimization For Model Predictive Control Using Principal Control Moves" in the *Journal of Process Control*.

Mandatory National Service

11/2014 - 07/2015	Austrian Service Abroad Austrian Holocaust Memorial Ambassador at American Jewish Committee New York, United States of America
08/2014 - 10/2014	Austrian Service Abroad Austrian Holocaust Memorial Ambassador at Sydney Jewish Museum Sydney, Australia

Professional Work Experience

04/2014 - 07/2014	Vienna University of Technology Educational Leave
03/2011 - 02/2014	Project Assistant at Vienna University of Technology Institute of Mechanics and Mechatronics Division of Control and Process Automation
07/2009	Internship at Test-Fuchs GMBH, Austria Engineering Department
07/2008 - 09/2008	Internship at Walter Unger GMBH, Austria Department for Security Matters and IT
08/2007	Internship at Altromin GMBH, Germany Technical Department
07/2006 - 08/2006	Internship at Walter Unger KFT, Hungary Technical Department
07/2005 - 08/2005	Internship at Walter Unger KFT, Hungary Technical Department
07/2004 - 08/2004	Internship at Csardahof GMBH, Austria Department for agricultural machines and equipment

IT Skills

Operation systems	Windows, Windows Server Systems, Linux
Office	Microsoft Office, Open Office, LATEX
Programming	C/C++, Matlab, LabView
Mathematics	Matlab, Maple, MathCAD
Simulation	Simulink
CAD	Catia, AutoCAD, Microstation (with certification)

Further Skills and Certifications

Microstation Certification (Certification of successful completion of the Descriptive Geometry Course using Microstation)

Welder's performance qualification in gas-shielded welding

Driver licenses for classes B and F

Languages

German	Native language
English	Fluent in written and spoken

Leisure Interests

Traveling, running, cooking, enjoying nature, Raspberry PI

Publications

1. J. UNGER, M. KOZEK, AND S. JAKUBEK
   Reduced Order Optimization For Model Predictive Control Using Principal Control Moves
   Journal of Process Control, Volume 22(1), pages 272–279, Elsevier, 2012.

2. J. UNGER, M. KOZEK, AND S. JAKUBEK
   Verfahren zur Ordnungsreduktion für Modellprädiktive Regelung
   17. Steirisches Seminar über Regelungstechnik und Prozessautomatisierung (SSRP 2011),
   Schloss Retzhof, Leibnitz, Austria, pages 17–31, ISBN: 978-3-901439-08-7, 2011.

3. C. HAMETNER, J. UNGER, M. QUASTHOFF
   DoE und Identifikation von Lithium-Ionen Zellen
   2. Workshop für Modellbasierte Kalibriermethoden, TU-Wien, 2011.

4. J. UNGER, M. KOZEK, AND S. JAKUBEK
   Reduced Order Optimization For Model Predictive Control Using Principal Control Moves
   Poster: NRW Young Scientist Award 2012, Düsseldorf, 2011.

5. C. HAMETNER, J. UNGER, S. JAKUBEK
   Local Model Network based Dynamic Battery Cell Model Identification
   12th WSEAS International Conference on Robotics, Control and Manufacturing Technology (ROCOM'12), pages 116–123, ISBN: 978-1-61804-085-5, WSEAS, 2012.

6. M. QUASTHOFF, J. UNGER, S. JAKUBEK
   Entwicklungsmethodik eines generischen Batterie-Simulationsmodells und dessen Einsatzmöglichkeiten
   5. Fachtagung Baumaschinentechnik 2012 in Dresden, Baumaschinentechnik 2012 - Energie, Mechatronik, Simulation, Dresden, Schriftreihe der Forschungsvereinigung Bau- und Baustoffmaschinen e.V. (FVB), Heft Nr. 44, pages 263–284, 2012.

7. J. UNGER, C. HAMETNER, S. JAKUBEK, M. QUASTHOFF
   Optimal Model Based Design of Experiments Applied to High Current Rate Battery Cells
   IEEE International Conference on Electrical Systems for Aircraft, Railways, Ship Propulsion and Road Vehicles (ESARS 2012 Edition), Bologna, ISBN: 978-1-4673-1371-1, pages 1–6, 2012.

8. J. UNGER, C. HAMETNER, S. JAKUBEK, M. QUASTHOFF
   A novel methodology for non-linear system identification of battery cells used in non-road hybrid electric vehicles
   Journal of Power Sources, Volume 269, pages 883–897, Elsevier 2014.

9. J. UNGER, M. QUASTHOFF, S. JAKUBEK
   Innovative Energy Management System Using a Model Predictive Controller with Disturbance Prediction for Off-Road Applications
   16. Antriebstechnisches Kolloquium (ATK 2015), 1. Auflage 2015, pages 427–443, 2015.

10. J. UNGER, M. KOZEK, S. JAKUBEK
    Nonlinear model predictive energy management controller with load and cycle prediction for non-road HEV
    Control Engineering Practice, Volume 36, pages 120–132, Elsevier, March 2015.